Spring 5-19-2018

A Comparative Analysis of Integrated Optical Waveguide Isolators with Magneto-Optic Layers

Reyhane Oztekin
Southern Methodist University, rkilci@smu.edu

A COMPARATIVE ANALYSIS OF

INTEGRATED OPTICAL WAVEGUIDE ISOLATORS

WITH MAGNETO-OPTIC LAYERS

Approved by:

_____

Jerome K. Butler, Professor

_____

Gary A. Evans, Professor

_____

Maria A. Martinez, Associate Professor

_____

Choon Lee, Associate Professor

_____

Johannes Tausch, Professor

A COMPARATIVE ANALYSIS OF INTEGRATED OPTICAL WAVEGUIDE ISOLATORS WITH MAGNETO-OPTIC LAYERS

A Dissertation Presented to the Graduate Faculty of

Bobby B. Lyle School of Engineering

Southern Methodist University

in

Partial Fulfillment of the Requirements

for the degree of

Doctor of Philosophy

with a

Major in Applied Science

by

Reyhane Kilci Oztekin

B.S. Bilkent University, Ankara, Turkey
M.S. Koc University, Istanbul, Turkey

May 19, 2018

ACKNOWLEDGEMENTS

I would like to express my sincere appreciation to my academic advisor, Dr. Jerome K. Butler, for his enthusiasm in academic guidance for me, inspirations, continuous motivation, and friendliness. We had countless days of discussions about my dissertation work and Dr. Butler never hesitated to patiently explain all details pertaining to my questions. I also would like to extend my gratitude to my co-advisor, Dr. Gary A. Evans, for his creative ideas to support my research, invaluable guidance, and assistance. This dissertation would not be complete without their aspirations. They trusted in me from the day they sent the admission letter for my doctoral study in our department and supported me at all stages of my stay at SMU. I present my sincere thanks to my dissertation committee member, Dr. Maria A. Martinez, for the immense support that she provided me with from the first day that I met her. I am also grateful to Dr. C. S. Yeh for the technical discussions and insights in new areas of optical isolator studies. Additionally, I am thankful to Dr. Chong Lee for his patience, friendliness, and kindness, which made me feel comfortable at SMU. The last but not the least, I want to emphasize the contribution that Dr. Johannes Tausch provided for this research. He helped me and our research team with his great ideas in mathematical modeling of our work.

I also want to express my gratitude to all my friends in the department and in Dallas, TX. Without their friendship and encouragement at the time of difficulties, this study would not have been completed. Also, I'd like to emphasize and acknowledge the strong support and guidance I got from my dear friends Susan Mitchell and Dr. James H. Waldo. I will always remember their warm friendship and support.

Finally, special thanks go to my husband Dr. Asil Oztekin for his patience with me during this journey as well as giving me a hand, his love and understanding, patience and sacrifice whenever I had hard times. And of course, I am so grateful to my parents, Sukran and Eyyup, for their strong encouragement towards completing my Ph.D. degree. Despite the distance, I always felt them overcoming the difficulties together with me. Therefore, I dedicate this dissertation to my family: Asil, Eyyup, and Sukran.

Oztekin, Reyhane Kilci B.S., Bilkent University, Ankara, Turkey
M.S., Koc University, Istanbul, Turkey

A Comparative Analysis of
Integrated Optical Waveguide Isolators
with Magneto-optic Layers

Advisor: Professor Jerome K. Butler

Doctor of Philosophy conferred May 19, 2018

Dissertation completed April 20, 2018

The objective of this study is to theoretically devise an on-chip optical isolator which is monolithically integrated with a semiconductor active waveguide layer yielding low loss. Use of magneto-optic materials for semiconductor waveguide isolators are indispensable to have nonreciprocal transmission of light. In this research, we first use ferromagnetic metals i.e. iron, cobalt, and nickel as magneto-optic materials in the development of optical isolators. From all these, iron is the one which shows a larger magneto-optic effect. Since there is a gap in literature about the optical characterization of iron to higher energies, we model the optical properties of iron by improving the Brendel-Bormann model. Our model for iron shows an excellent fit with the optical data up to 30 electronvolts (eV).

The theory of the proposed optical waveguide isolator with the solutions of Maxwell Equations for the TE and TM modes is analyzed in detail. In contrast to the TE mode, TM mode has an anisotropic behavior which is required to observe nonreciprocity;

therefore, it is selected as an operating mode for our devices. As performance metrics for the isolators, the conventional isolation ratio and the insertion loss parameters are considered. The isolation ratios of the devices with these three metals yield promising results. However, the insertion loss values are in very high ranges due to their large optical absorptions that prevents these metals from being the best candidates for the use of optical isolators.

In contrast to the ferromagnetic elemental metals in this work, magnetic garnets are better candidates for optical waveguide isolators thanks to their low loss and large Faraday rotation properties. Therefore, we utilize cerium-substituted yttrium iron garnet (Ce:YIG) as a magneto-optic material for the proposed isolator design. The study is unique in using magnetic garnets as a magneto-optic material for semiconductor waveguide optical isolators. A high amount of isolation ratio of 55 dB is attained while the insertion loss is fairly low at the level of 0.47 dB/mm. The limitation of the study with Ce:YIG is mainly attributed to its large footprint. Apart from that, Ce:YIG material is demonstrated to be a favorable candidate for on-chip isolator applications. This theoretically devised design yields satisfactory results. However, further experimental research needs to be conducted to validate the proposed methodology in practice.

TABLE OF CONTENTS

TABLE OF CONTENTS VIII

1 INTRODUCTION 1

1.1 Motivation and Literature Review 1

1.2 Research Goal and Objectives 4

2 OPTICAL PROPERTIES OF METALS 6

2.1 Introduction and Literature Review 6

2.2 Drude Free Electron Model 8

2.3 Lorentz Oscillator Model 13

2.4 Electric Susceptibility for Anisotropic Materials 17

2.5 Brendel-Bormann (BB) Model 27

2.5.1 The superiority of BB model over LD model 28

2.5.2 Electric Susceptibility from the BB Model 30

2.6 Methodology and Discussion 32

2.6.1 Dielectric Constant of Gold 33

2.6.2 Susceptibility of Iron 37

2.7 Conclusion 41

3 MAGNETO-OPTIC EFFECTS 43

3.1 Introduction to Magneto-optic Effects 43

3.2 The Solutions of the Refractive Index for the Faraday and Voigt Effects 47

3.3 Magneto-optic Kerr Effect (MOKE) 51

3.4 Parameters for The Types of MOKE 54

4 THEORY OF MAGNETO-OPTIC LAYER EMBEDDED OPTICAL WAVEGUIDE ISOLATORS 59
4.1 Introduction 59
4.2 Structure 60
4.3 Solutions of Maxwell Equations for the Static Magnetic field-B_y: 63
4.3.1 The Solutions for the TM Mode 66
4.3.2 TE Modes 78
4.4 Perturbation Matrices 83
4.5 TM Mode Orthogonality 87
4.6 Laser-Isolator Boundary Conditions 90
4.7 Isolation Ratio and Insertion Loss 95
4.8 The TM Mode Results for the Fe-embedded Case 97
5 OPTICAL WAVEGUIDE ISOLATORS WITH ALTERNATING LAYERS OF MAGNETO-OPTIC LAYER AND SILICON 103
5.1 Introduction and Literature Review 103
5.2 Structure of the Proposed Isolator with Alternating Layers of Magneto-Optic Material 111
5.3 Design and Methodology 114
5.3.1 Methodology for the Proposed Design 116
5.3.2 Alternating Layer Structure 119
5.3.3 Onsager's Relations in Magnetic Fields 121
5.3.4 Nonreciprocal Phase Shift 122
5.3.5 Device Length – Nonreciprocal Phase Shift (NRPS) Relationship 127

5.4 Results and Discussion 130
5.4.1 Iron, Cobalt, and Nickel 130
5.4.1.1 Field Profiles 130
5.4.1.2 Loss Profiles 133
5.4.2 Ce-substituted YIG (Ce:YIG) 137
5.4.2.1 Field Profile 138
5.4.2.2 Loss Profile 139
6 CONCLUSION AND FUTURE WORK 144
6.1 Conclusion 144
6.2 Future Work 151
7 APPENDIX 153
7.1 Appendix 1 153
7.2 Appendix 2 156
7.3 Appendix 3 160
7.4 Appendix 4 163
8 BIBLIOGRAPHY 165

TABLE OF FIGURES

Figure 2.1 The real and imaginary parts of the susceptibility for the Drude model [55]. Experimental values of χ_i and $-\chi_r$ for iron are obtained from Weaver et al. [44]-[45]. 24

Figure 2.2 The real, $-\kappa_r$, and the imaginary parts, κ_i, of the dielectric constant for gold. Small round and square shape circles are for the experimental data of real and imaginary parts, respectively [62]. The solid curves refer to our model, while dashed ones refer to Rakic [42]. 36

Figure 2.3 The real, χ_r and imaginary parts, χ_i of the susceptibility of iron using the proposed BB model [55]. The small circles are the experimental values obtained by Weaver et al. [44]-[45]. 40

Figure 3.1 (a) Polar, (b) longitudinal, and (c) transverse MOKE configurations 52

Figure 3.2 The general illustration of the MO Kerr Effect 54

Figure 4.1 Two-dimensional structure of the proposed isolator 61

Figure 4.2 Magneto-optic region of the proposed device 62

Figure 4.3 Simple representation of the proposed device 91

Figure 4.4 The plot for the real part of the propagation constant β versus resonant layer thickness for Iron-Silicon alternating layer embedded waveguide isolator 98

Figure 4.5 Isolation and insertion loss plot for the waveguide isolator with four thin Fe layers 99

Figure 4.6 Isolation and insertion loss plot for the one Fe layer structure 101

Figure 5.1 Two dimensional structure of the proposed isolator 111

Figure 5.2 (a) The effective index matching and the field profile of the separate two waveguides (b) The combined structure of the two sub-waveguides with the TM_0 and TM_1 modes 117

Figure 5.3 The relative refractive index profile for the alternating layer structure of the isolator design with (a) magneto-optic (MO) metals and (b) Ce:YIG material .. 120

Figure 5.4 The isolation-insertion loss plot versus device length for the semiconductor optical waveguide isolator with thin Ce:YIG layers (a) Loss plot with device length of around 1 mm. (b) Loss plot with device length of around 9 mm 128
Figure 5.5: Hy field profile for the isolator with iron metal layer 131
Figure 5.6 Hy field profile for the isolator with cobalt metal layer 132
Figure 5.7 Hy field profile for the isolator with nickel metal layer 133
Figure 5.8 The loss profile of the isolator with Iron layer in terms of device length 134
Figure 5.9: The loss profile for the Cobalt layer embedded isolator in terms of varying device length 135
Figure 5.10 The loss profile for Nickel implemented isolator 136
Figure 5.11 The field profile for the isolator design with Ce:YIG material. 138
Figure 5.12 Isolation profile for the device length 5.12 mm, while the peak wavelength is 1.54 μm. 140
Figure 5.13 Sensitivity check of the design by changing the refractive indices of the QW laser's layers. Solid lines represent backward propagation while dashed lines are for forward propagation. 141
Figure 7.1 Proposed methodology for the isolator design 164

LIST OF TABLES

Table 2.1 The calculated parameters of gold using the BB model. The first three columns are the parameters from Rakic et al. [42], and the last three columns are from our proposed BB model. All terms are in the eV unit excluding f_j. 34
Table 2.2 The calculated optimization parameters of iron by using the proposed BB model (in eV unit) 37
Table 5.1 The isolator structure with Ce:YIG layer. 112
Table 5.2 The isolator structure with magneto-optic metals Fe, Co, and Ni. 114
Table 5.3 The relationship between the insertion loss and device length of the proposed isolator 129
Table 6.1 The magneto-optical properties of ferromagnetic metals [86], [90] and the insertion loss/isolation results. 149
Table 6.2 The results of the sensitivity check for the Ce:YIG implemented waveguide isolator 150

CHAPTER 1

1 INTRODUCTION

1.1 Motivation and Literature Review

The first transistor was invented in 1947 [1] and following that, Silicon-based electronic integrated circuits (EICs) gained an outstanding attention in literature in short period of time. Main reasons for this significant success were noted by Kaminov as the compatibility of the semiconductor materials and the cost effectiveness of the small-scale devices [2]. In contrast to the rapid progress in the EICs, the developments in the photonic integrated circuits (PICs) followed a slower trajectory, presumably due to the fact that there needs to be a lot of photonic elements of which sizes are supposed to be larger than the elements in the EICs [2]-[3]. To illustrate, even though the very first photonic integrated circuit (PIC) was proposed by Miller in 1969 [4], the earliest industrial application could not have been designed until 2005 [2]. Fortunately, it was understood that the ICs are inevitable for future photonic and opto-electronic systems (OEICs). The key driving factor for the research on PICs is the potential cost effectiveness and robustness of the photonic system since there would be a huge impact on the stability if it is replaced with a monolithically integrated version and fabricated on a single chip [5].

One of the potential limitations for the effective PICs and OEICs is considered to be the lack of realistically integrated optical isolators [6] since optical isolators are fundamental components in optical communications to protect lasers from undesired back reflections [7]-[8]. Although there are some recent advancements in the design of optical integrated isolators, commercially available isolators are still bulk and expensive devices, which cannot be integrated with InP-based and/or Silicon-based opto-electronic devices. Moreover, early studies about isolators use TE-TM mode conversion, which in a way is similar to bulk Faraday rotators [9]-[10]. To facilitate the expected level of mode conversion within these isolators, the phase matching of TE and TM modes is essential. This would render the device sensitive to the variations in waveguide parameters, which in turn would make it impractical.

In order to develop integrated optical isolators, some ferromagnetic metals and compounds (e.g. Fe, Co, Ni, MnAs) have been inserted into the optical isolators that are monolithically integrated with semiconductor optical amplifiers (SOA) [9]-[16]. A magnetic bias is transversely applied to facilitate the magneto-optic Kerr effect (MOKE) in these devices. The optical gain generated by the active SOA layer helps compensate the forward loss. On the other hand, backward loss is not fully compensated, which in turn yields optical isolation. In the opto-electronics field, the integration of optical isolators with SOA has a critical role. However, using SOA gain to compensate the forward loss is a problematic approach in literature since spontaneous emission provides additional noise to the system [17]. To the best of our knowledge, Hammer *et al.*'s work [18] in 2006 is the

only study so far that did not utilize SOA gain in order to compensate the forward loss. They devised an SOA-type optical isolator with ferromagnetic iron nanoparticles embedded in an InGaAsP layer. However, they reduced the extinction ratio of iron by 1/30, which is in fact impractical, that yielded overly optimistic loss results of 2-4 dB.

Another type of integrated optical isolators is designed by using interferometer type devices [19]-[24]. Yttrium iron garnet ($Y_3Fe_5O_{12}$-YIG) materials are widely utilized for this purpose since they have a significant magneto-optic effect and relatively low optical absorption [6], [24]. However, interferometric isolators suffer from large device footprints which is a limitation for the on-chip applications [25].

According to the abovementioned integrated optical isolator studies, there is a clear gap in literature to be further studied as to how magneto-optic materials would be integrated with SOAs monolithically. The compensation of forward loss with optical gain still remains a problem for the "ferromagnetic metal"-based isolators while being a large device is also a perennial drawback of the interferometric isolators.

1.2 Research Goal and Objectives

In this dissertation, I propose and theoretically analyze the semiconductor active waveguide optical isolators with various ferromagnetic metals (i.e. Fe, Co, Ni) and a ferrimagnetic garnet (i.e. Cerium-substituted Yttrium Iron Garnet--Ce:YIG). To the best of our knowledge, this is the first monolithically integrated isolator study in literature that does not utilize the optical gain as a compensation tool for the forward loss and hence is a novel approach. Our devices perform in the TM mode at a $1.55\ \mu m$ telecommunication wavelength; therefore, there is no need for the TE-TM mode matching. The proposed optical isolator is monolithically integrated with an InGaAsP Multi-Quantum Well (MQW) laser. By the help of proper current injection into the MQW, we could produce laser light in the device itself rather than acquiring it externally as in the case of interferometric isolators. In order to facilitate magneto-optic effects, the optical isolator region is fabricated with various substances (i.e. Fe, Co, Ni, and Ce:YIG). The two isolator modes are excited by the laser light originating from the QW laser. The power can be shared between the QW and isolator regions through the coupling of the two layers. Backward light can be confined primarily into the lossy isolator section via a proper optimization of layer parameters, which is the desired isolator behavior in our currently suggested configuration.

It is needed to characterize optical properties of ferromagnetic materials (especially of iron) to be used in the design of optical waveguide isolators. Ferromagnetic metals are anisotropic and are identified by a susceptibility tensor with nonzero off-diagonal elements.

Therefore, accurate knowledge of such susceptibility tensors, which are obtained from the electronic band structure of materials, is required for the design of such isolators. In Chapter 2, we accordingly analyze optical characteristics of iron for this aforementioned purpose.

Different types of integrated optical isolators utilize different magneto-optic effects. To exemplify, some of the SOA-type isolators that are incorporated with ferromagnetic metal utilize the Magneto-optic Kerr Effect [14]-[16], whereas some of the interferometric isolators utilize the Faraday effect [20], [22]. Therefore, a brief explanation of magneto-optic effects is provided in Chapter 3.

The theory of the proposed optical waveguide isolators is explained in Chapter 4. The mathematical derivations of Maxwell Equations are performed by considering the flexibility in the numbers of layers. Through TE and TM mode solutions, it is observed that TE mode is not associated with the magnetic bias. This demonstrates that the TE mode follows the isotropic behavior along the magnetic field direction.

A comparative study of semiconductor active waveguide optical isolators with Fe, Co, Ni ferromagnetic metals and low-loss Ce:YIG is conducted in Chapter 5. The isolation ratios and the insertion losses are presented as performance metrics. It is illustrated that by the determination of optimum layer parameters, the low-loss integrated optical isolators can be realized practically.

CHAPTER 2

2 OPTICAL PROPERTIES OF METALS

2.1 Introduction and Literature Review

This chapter is motivated by the need for the optical characteristics of ferromagnetic materials, especially iron, for use in waveguide optical isolators. These metals may be used as one or more layers of an optical waveguide or they may be used as metal dopant atoms or clusters of metal atoms in a host material such as a semiconductor, glass or polymer to form one or more ferromagnetic layers in an optical waveguide [12], [26]-[29]. Ferromagnetic materials are anisotropic and are characterized by a susceptibility tensor with nonzero off-diagonal elements whose values change with an applied magnetic field. Designing waveguide isolators requires accurate knowledge of such susceptibility tensors, which are obtained from the electronic band structure of materials [31]-[36].

Ehrenheich et al. [31] analyzed experimental data for the dielectric constants for silver and copper from 1 to 25 eV by the help of three mechanisms which are free electron effects, interband transitions, and plasma oscillations. In order to distinguish plasma transitions from interband transitions, theoretical values of the real and imaginary parts of the dielectric constant as well as the loss function was plotted as a function of photon

energy. They acquire average optical mass values for silver and copper for the free electron effect region by combining the theoretical and experimental values of the dielectric constant. In 1987, Adachi used a harmonic oscillator model with a critical point-parabolic band model that incorporated Lorentzian broadening and temperature dependence to find optical constants as a function of alloy composition for zinc-blende semiconductors [32]. The resulting model showed that contributions from indirect transitions could be significant [32].

The Drude model for the permittivity [37]-[39] is based on free electrons and it was extensively used until the late 1980s to obtain the optical constants of metals. An extension of this model, referred to as the Lorentz-Drude (LD) model included bound electrons by assuming damped harmonic oscillators at critical wavelengths that correspond to interband transitions [40]-[43].

Brendel and Bormann (BB) extended previous work to obtain optical constants of amorphous solids in the infrared by including a superposition of oscillators at critical wavelengths with linewidths that were a convolution of Gaussian and Lorentzian linewidths (Voigt profiles) [34], resulting in good agreement with experimental values at room temperatures [36]. Rakic *et al.* applied the BB approach to obtain optical constants for various metals in the infrared, visible and ultraviolet regions [42].

In this work, we build on the BB model and the work of Rakics' to obtain a model for the optical constants of iron based on experimental data [44]-[45]. We verify our model

by comparing our theoretical calculations to the experimental data for gold and to Rakics' theoretical model for gold. Our modified BB model used a reduced number of parameters yet provides excellent agreement with experimental data.

2.2 Drude Free Electron Model

After the discovery of electron by J. J. Thomson, Drude built his theory for electrons by utilizing kinetic theory of gases [46]. In his theory, he considered metallic electrons as gaseous particles. Since there is no modern quantum theory at this time, he assumed that there are some immobile heavy particles as electrons, which hold the mobile positive particles. The quantum theory shows that the heavy immobile particles are the nucleus filled with positive particles. However, The Drude's Theory states that when a solid is built by bringing the metallic atoms together, the core electrons remain immobile as positive particles in Drude's original assumption and valence electrons move around the metal freely [46]. We called those valence electrons as conduction electrons. According to Free Electron Theory, there is no electron-electron and electron-ion interaction, which makes the electrons to be in uniform motion if there is no external electromagnetic field. If the system is under the effect of an external electromagnetic field, then Drude's theory only take into account that field without considering the fields coming from electrons and ions [46].

When it comes to collisions, he defined that electrons only bounce off impassable ion cores not off other electrons. The probability per unit time for the collision of an electron is $1/\tau$, and τ is known as mean free time or collision time. Mean free time, τ, is a time period that is accumulated for an electron in between its two collisions [46]. The relaxation time, τ, is assumed to be free from the changes of the position and the velocity of the electron [46].

To get the optical characterization of metals we need to utilize the equation of motion for valence electrons in that metal. The equation of motion for the Drude model, which accepts the valence electrons as completely free, is described as:

$$m^* \left(\frac{\partial^2 \vec{r}}{\partial t^2} + \gamma_1 \frac{\partial \vec{r}}{\partial t} \right) = \vec{F} \tag{1}$$

m^* is the effective mass of an electron, $\vec{r}$ is the relative position to atom, γ_1 is the damping factor related to collisions with atomic sites, and $\vec{F}$ is the driving force acting on the electron, which is shown as in Eq. (2):

$$\vec{F} = q\left[\vec{e}(t) + \vec{v} \times \left(\vec{b}(t) + \vec{B}_s\right)\right] \tag{2}$$

where q is the charge of an electron. For the time-harmonic electromagnetic field, the displacement vector for electrons from the nucleus is defined as $\vec{r} = \vec{R}.\exp(j\omega t)$, and electron velocity is defined as $\vec{v} = j\omega\vec{R}.\exp(j\omega t)$, while local electric field is $\vec{e}(t) =$

$\vec{E}.\exp(j\omega t)$ and local magnetic field is $\vec{b}(t) = \vec{B}.\exp(j\omega t)$. $\vec{B}_s$ is the externally applied magnetic field, which is $\vec{B}_s = \hat{x}B_1 + \hat{y}B_2 + \hat{z}B_3$. Given that $\vec{b}(t) = \mu_0\vec{h}(t)$ and $\left|\vec{h}(t)\right| = \left(\frac{\varepsilon_0}{\mu_0}\right)^{1/2}|\vec{e}(t)|$, $\left|\vec{b}(t)\right|$ is on the order of $\frac{1}{c}|\vec{e}(t)|$. This demonstrates that $|\vec{e}(t)|$ is much greater than $v \times \left|\vec{b}(t)\right|$. Accordingly, the effect of local magnetic field is insignificant compared to the local electric field. Therefore, we would include the externally applied static magnetic field, $\vec{B}_s$ to the force equation and omit the effect of the local magnetic field, $\vec{b}(t)$. Then, the force equation is as follows:

$$\vec{F} \cong q\left[\vec{e}(t) + \vec{v} \times \vec{B}_s\right] \tag{3}$$

Considering the time varying electromagnetic field and displacement vectors, the equation of motion for the Drude model is

$$(j\omega\gamma_1 - \omega^2)\vec{R} = \frac{q}{m^*}\left(\vec{E} + j\omega\vec{R} \times \vec{B}_s\right) \tag{4}$$

while;

$$\begin{aligned}\vec{R} \times \vec{B}_s &= \begin{bmatrix} \hat{x} & \hat{y} & \hat{z} \\ R_1 & R_2 & R_3 \\ B_1 & B_2 & B_3 \end{bmatrix} \\ &= \hat{x}(R_2B_3 - B_2R_3) + \hat{y}(R_3B_1 - B_3R_1) + \hat{z}(R_1B_2 - B_1R_2)\end{aligned} \tag{5}$$

The final form of the equality becomes as in Eq. (6):

$$\vec{R} \times \vec{B}_s = \begin{bmatrix} 0 & B_3 & -B_2 \\ -B_3 & 0 & B_1 \\ B_2 & -B_1 & 0 \end{bmatrix} \cdot \begin{bmatrix} R_1 \\ R_2 \\ R_3 \end{bmatrix} = \overleftrightarrow{B}_s \cdot \vec{R} \rightarrow \vec{R} \times \vec{B}_s = \overleftrightarrow{B}_s \cdot \vec{R} \tag{6}$$

This shows that the asymmetric external static magnetic field dyadic $\overleftrightarrow{B}_s$ is

$$\overleftrightarrow{B}_s = \begin{bmatrix} 0 & B_3 & -B_2 \\ -B_3 & 0 & B_1 \\ B_2 & -B_1 & 0 \end{bmatrix} \tag{7}$$

Then, the equation of motion is given as:

$$(j\omega\gamma_1 - \omega^2)\vec{R} = \frac{q}{m^*}\vec{E} + \frac{q}{m^*} j\omega \overleftrightarrow{B}_s \cdot \vec{R} \tag{8}$$

Therefore, the displacement vector of an electron from the nucleus can be defined as:

$$\vec{R} = \frac{1}{(j\omega\gamma_1 - \omega^2)} \frac{q}{m^*}\vec{E} + \frac{1}{(j\omega\gamma_1 - \omega^2)} \frac{q}{m^*} j\omega \overleftrightarrow{B}_s \cdot \vec{R} \tag{9}$$

The equation of motion with the introduction of identity dyadic, $\vec{I}$ is:

$$\left(\vec{I} + \frac{j\omega}{(\omega^2 - j\omega\gamma_1)} \frac{q}{m^*} \overleftrightarrow{B}_s\right) \cdot \vec{R} = \frac{1}{(j\omega\gamma_1 - \omega^2)} \frac{q}{m^*}\vec{E} \tag{10}$$

where $\vec{I}$ represents the identity matrix. After rearranging Eq. (10), it can now be rewritten as in Eq. (11):

$$\left(\overleftrightarrow{I}-\frac{1}{j\omega\left(1-j\frac{\gamma_1}{\omega}\right)}\frac{q}{m^*}\overleftrightarrow{B}_s\right)\cdot\vec{R}=\frac{1}{j\omega}\frac{1}{j\omega\left(1-j\frac{\gamma_1}{\omega}\right)}\frac{q}{m^*}\vec{E} \tag{11}$$

If we define

$$\frac{1}{\widetilde{\Lambda}_1}=\frac{1}{j\omega\left(1-j\frac{\gamma_1}{\omega}\right)}\frac{q}{m^*} \tag{12}$$

Then, the simpler form of the equation of motion is described as:

$$\left(\overleftrightarrow{I}-\frac{1}{\widetilde{\Lambda}_1}\overleftrightarrow{B}_s\right)\cdot\vec{R}=\frac{1}{j\omega.\widetilde{\Lambda}_1}\vec{E} \tag{13}$$

After dividing the $\overleftrightarrow{B}_s$ dyadic over $\widetilde{\Lambda}_1$, the static magnetic field dyadic for the Drude model can be defined as in Eq. (14):

$$\overleftrightarrow{B}_1=\begin{bmatrix}0 & b_3 & -b_2\\ -b_3 & 0 & b_1\\ b_2 & -b_1 & 0\end{bmatrix}=\frac{1}{\widetilde{\Lambda}_1}\begin{bmatrix}0 & B_3 & -B_2\\ -B_3 & 0 & B_1\\ B_2 & -B_1 & 0\end{bmatrix} \tag{14}$$

where $b_i=B_i/\widetilde{\Lambda}_1$, $i=x,y,z$. The solution of the electron displacement vector for free electrons is as follows:

$$\vec{R}_1=\frac{1}{j\omega\widetilde{\Lambda}_1}\left(\overleftrightarrow{I}-\overleftrightarrow{B}_1\right)^{-1}\cdot\vec{E} \tag{15}$$

Since the charged particle is electron, q is equal to $-e$. It has a charge of $1.602 \times 10^{-19}C$. The charge to mass ratio, e/m is $1.759 \times 10^{11}\ C/kg$. At $\lambda = 1.55\ \mu m$, the frequency of light would be $\omega = 1.216 \times 10^{15}\ rads/sec$. According to Ordal *et al*. damping frequency is defined as $\gamma_1(cm^{-1}) = \frac{1}{2\pi\tau}$, while τ is the lifetime for the electrons [39]. The damping frequencies for different metals are listed in Babiskin *et al*. who stated the damping frequency of iron as $\gamma_1 = 147\ cm^{-1}$ [47]. After adapting the numbers above into Eq. (12), the value of $\widetilde{\Lambda}_1$ would be $-j6913\ Weber/m^2$.

2.3 Lorentz Oscillator Model

The concept of oscillating dipoles was first discovered by Hendrik Antoon Lorentz in 1878 [48]. Even if the electron and the nuclei could not have been discovered until 1897 and 1911, respectively, by J. J. Thomson and E. Rutherford; Lorentz achieved to combine the outcomes of classical mechanics and electromagnetic theory very thoroughly to hypothesize the existence of dipoles [48], [49]. Lorentz stated that the electron with a smaller mass is bound to the nucleus with a larger mass under the impact of spring-like force, widely known as Hooke's Law [49]. Since the nucleus has larger mass, it is approximately stationary, and electrons oscillate around the nucleus. The natural resonant frequency, ω_0 of the oscillating dipoles can be computed using the restoring force and the reduced masses of the electron and nucleus [48]:

$$\frac{1}{\mu} = \frac{1}{m_e} + \frac{1}{m_N} \tag{16}$$

where m_e and m_N are the masses of the electron and the nucleus, respectively, and μ is the reduced mass of the electric dipole. Since $m_N \gg m_e$, the reduced mass μ will be nearly equal to m_e. The restoring force and the natural frequency of dipoles are shown in the Eq. (17):

$$F(r) = -kr \quad , \quad \omega_0 = \sqrt{\frac{k}{m_e}} \tag{17}$$

where k refers to the spring constant and r refers to the displacement from the equilibrium position. Previously, the absorption and emission spectra of some materials at certain frequencies were discovered; then, Lorentz explained the physics behind these brand-new electromagnetic concepts [48]. The resonant frequencies of transitions can be found using absorption and emission spectra of materials in various regions of electromagnetic spectrum. The spring-like Lorentz equation of motion with the inclusion of damping force is described as in Eq. (18):

$$m^* \frac{\partial^2 \vec{r}}{\partial t^2} = \vec{F} - \gamma_2 m^* \frac{\partial \vec{r}}{\partial t} - \omega_0^2 m^* \vec{r} \tag{18}$$

Unlike free electrons, which are not bound to any atoms, bound electrons experience a restoring force while they are displaced, so their natural frequencies are not equal to zero. γ_2 is the damping coefficient which originates from the atomic collisions in a solid and the spontaneous emission radiated by the accelerating electron [48], [49]. The damping term mainly diminishes the peak of the absorption coefficient, and it causes the broadening in the line-shape of the absorption peak [48]. When we take into account the time-varying electromagnetic fields and the time-varying displacement, the Lorentz equation of motion under an externally applied magnetic field is as follows:

$$(j\omega\gamma_2 + \omega_0^2 - \omega^2)\vec{R} = \frac{q}{m^*}\left(\vec{E} + j\omega\vec{R} \times \vec{B}_s\right) \tag{19}$$

The electric part of the driving force is applied by the time-varying electric field, which causes oscillations in the atom with frequency ω. If ω, frequency of the system of particles is concurrent with one of the resonant frequencies, the resonance property occurs. Under the resonance condition, the atom gains large amount of energy from the incoming electromagnetic wave, which is called absorption. Considering Eq. (6), the equation of motion for Lorentz model can be described as:

$$(j\omega\gamma_2 + \omega_0^2 - \omega^2)\vec{R} = \frac{q}{m^*}\left(\vec{E} + j\omega\vec{B}_s \cdot \vec{R}\right) \tag{20}$$

After rearranging Eq. (20), the equation is

$$\vec{R} = \frac{1}{(j\omega\gamma_2 + \omega_0^2 - \omega^2)} \frac{q}{m^*} \vec{E} + \frac{1}{(j\omega\gamma_2 + \omega_0^2 - \omega^2)} \frac{q}{m^*} j\omega \overleftrightarrow{B}_s \cdot \vec{R} \tag{21}$$

After some mathematical manipulations, we would obtain Eq. (22):

$$\left(\overleftrightarrow{I} - \frac{1}{j\omega \left(1 - \frac{\omega_0^2}{\omega^2} - j\frac{\gamma_2}{\omega}\right)} \frac{q}{m^*} \overleftrightarrow{B}_s \right) \cdot \vec{R} = \frac{1}{j\omega . j\omega \left(1 - \frac{\omega_0^2}{\omega^2} - j\frac{\gamma_2}{\omega}\right)} \frac{q}{m^*} \vec{E} \tag{22}$$

In order to simplify Eq. (22), Eq. (23) would be defined:

$$\frac{1}{\widetilde{\Lambda}_2} = \frac{1}{j\omega \left(1 - \frac{\omega_0^2}{\omega^2} - j\frac{\gamma_2}{\omega}\right)} \frac{q}{m^*} \tag{23}$$

If we define normalized damping frequency and normalized resonant frequency as $\Gamma_2 = \frac{\gamma_2}{\omega}$ and $\Omega_2 = \frac{\omega_0}{\omega}$ respectively, Eq. (23) is now reduced to:

$$\frac{1}{\widetilde{\Lambda}_2} = \frac{1}{j\omega(1 - \Omega_2^2 - j\Gamma_2)} \frac{q}{m^*} \tag{24}$$

Furthermore, the complex normalized frequency can be defined as $\widetilde{\Omega}_2 = (1 - \Omega_2^2 - j\Gamma_2)$, while for the other bound electron groups it would be $\widetilde{\Omega}_j = \left(1 - \Omega_j^2 - j\Gamma_j\right)$. After

introducing the new variables into the equation of motion, the electron displacement vector from the nucleus is written as:

$$\vec{R}_2 = \frac{1}{j\omega\tilde{\Lambda}_2}\left(\overleftrightarrow{I} - \overleftrightarrow{B}_2\right)^{-1} \cdot \vec{E} \tag{25}$$

while $\overleftrightarrow{B}_2$ is represented as:

$$\overleftrightarrow{B}_2 = \frac{1}{\tilde{\Lambda}_2}\begin{bmatrix} 0 & B_3 & -B_2 \\ -B_3 & 0 & B_1 \\ B_2 & -B_1 & 0 \end{bmatrix} \tag{26}$$

Moreover, the displacement equations will be used in the polarization equation to reach the susceptibility parameter for these two types of electron models.

2.4 Electric Susceptibility for Anisotropic Materials

The dipole moment for a single dipole is shown as $\vec{p} = q\vec{R}$, which is a vector from the electron to the nucleus. For a system of particles, we need to define polarization vector, which is the collection of dipole moments per unit volume:

$$\vec{P} = N\vec{p} \quad \Rightarrow \quad \vec{P} = Nq\vec{R} \tag{27}$$

In this equation, N is the number of dipoles per unit volume, which is exactly the same as the number of valence electrons per unit volume −Given that the valence electrons are the

ones which are characterized optically−. Another formula for the polarization of isotropic materials is:

$$\vec{P} = \varepsilon_0 \chi \vec{E} \tag{28}$$

where χ is the electric susceptibility and ε_0 is the vacuum permittivity. The amount of polarization is related to the present electric field in the material, which causes the formation of dipoles. The amount of susceptibility is unique for each material, which enhances the impact of the electric field to cause the formation of dipoles. The number of dipoles for an iron atom is $N = 8.46 \times 10^{28}\ dipoles/m^3$ while the density of iron is $\rho = 7850\ kg/m^3$ [50]. There is one more term called *plasma*, which is a collection of various electrons and the ionized nuclei [49], [51]. The outermost electrons tend to be collectively volatile that leaves the nuclei ionized under the condition of high temperatures or lower particle densities. In equilibrium, the electric field vectors on electron gas and ionized nuclei cancel each other, but it is not easy to protect that status. Therefore, if there is a separation in between electron gas and ionized nuclei, Coulomb force enters to the picture to rebuild their equilibrium position, which makes them to have oscillatory behavior [49], [51]. *Plasma frequency* ω_P is the natural frequency when these oscillations resonate:

$$\omega_P^2 = \frac{q^2 N}{m^* \varepsilon_0} \tag{29}$$

The plasma frequency for non-plasma materials refers to the natural oscillation frequency of the collective electrons instead of the individual dipoles [49]. For isotropic medium, according to the constitutive relations $\vec{D} = \varepsilon\vec{E}$ and $\vec{B} = \mu\vec{H}$; $\vec{D}$ and $\vec{E}$ are parallel to each other as well as $\vec{B}$ and $\vec{H}$. Moreover, the permittivity, ε, and the permeability, μ, of the medium are constant. However, for the anisotropic medium, neither $\vec{D}$ and $\vec{E}$, nor $\vec{B}$ and $\vec{H}$ are parallel to each other. Therefore, the electric permittivity would be a tensor rather than a scalar for anisotropic materials. This is because the constants of permittivity and permeability are different for each principal direction in $3D$ Cartesian coordinate system for anisotropic media. Therefore, for anisotropic media the permittivity relations would be as follows:

$$\overleftrightarrow{\varepsilon} = \overleftrightarrow{\kappa}\varepsilon_0 \quad while \quad \overleftrightarrow{\kappa} = \overleftrightarrow{I} + \overleftrightarrow{\chi} \tag{30}$$

when $\overleftrightarrow{\kappa}$ is the relative permittivity of the medium, and $\overleftrightarrow{I}$ is the identity matrix. The susceptibility tensor would be represented as:

$$\overleftrightarrow{\chi} = \begin{bmatrix} \chi_{11} & \chi_{12} & \chi_{13} \\ \chi_{21} & \chi_{22} & \chi_{23} \\ \chi_{31} & \chi_{32} & \chi_{33} \end{bmatrix} \tag{31}$$

For anisotropic materials, the polarization formula is defined as:

$$\vec{P} = \varepsilon_0\overleftrightarrow{\chi}.\vec{E} \tag{32}$$

If the Eq. (27) and Eq. (32) are solved together, the dot product of the susceptibility tensor and the electric field vector would be illustrated as in Eq. (33):

$$\overleftrightarrow{\chi}.\vec{E} = \frac{Nq\vec{R}}{\varepsilon_0} \tag{33}$$

Considering the displacement relation for free electrons in Eq. (15), Eq. (33) can now be rewritten as:

$$\overleftrightarrow{\chi}_1.\vec{E} = \frac{Nq}{\varepsilon_0 j\omega\widetilde{\Lambda}_1}\left(\overleftrightarrow{I} - \overleftrightarrow{B}_1\right)^{-1} \cdot \vec{E} \tag{34}$$

The dot products of the electric field on both sides could cancel each other and the susceptibility relation would be simplified.

$$\overleftrightarrow{\chi}_1 = \frac{Nq}{\varepsilon_0 j\omega\widetilde{\Lambda}_1}\left(\overleftrightarrow{I} - \overleftrightarrow{B}_1\right)^{-1} \tag{35}$$

If we place Eq. (12) into Eq. (35), the susceptibility due to free electrons is:

$$\overleftrightarrow{\chi}_1 = \frac{Nq^2}{\varepsilon_0 m^* j\omega j\omega\left(1 - j\frac{\gamma_1}{\omega}\right)}\left(\overleftrightarrow{I} - \overleftrightarrow{B}_1\right)^{-1} \tag{36}$$

Complex normalized frequency can be defined as $\widetilde{\Omega}_1 = \left(1 - j\frac{\gamma_1}{\omega}\right)$, while plasma frequency is defined in Eq. (29). After introducing the complex normalized frequency and the plasma frequency into Eq. (36), the simplified susceptibility relation would be as follows:

$$\overleftrightarrow{\chi}_1 = -\frac{\omega_P^2}{\omega^2\widetilde{\Omega}_1}\left(\overleftrightarrow{I} - \overleftrightarrow{B}_1\right)^{-1} \tag{37}$$

If there is no external magnetic field, the complex susceptibility constant due to free electrons is:

$$\chi_1 = -\frac{\omega_P^2}{\omega^2\widetilde{\Omega}_1} = -\frac{\omega_P^2}{(\omega^2 + \gamma_1^2)} - j\frac{\omega_P^2\gamma_1}{\omega(\omega^2 + \gamma_1^2)} \tag{38}$$

In that equation, we could find out that the real and imaginary parts are negative, and there is a singularity at $\omega = 0$ in the imaginary part of the susceptibility. The conductance is determined as $\sigma = \varepsilon_0\omega_{P_1}^2/\gamma_1$ for the low frequency limit. In an anisotropic susceptibility tensor for a specific magnetic field direction, there are two different terms mainly; one is the diagonal term and the other one is the off-diagonal term. As an example, for the magnetic field along $\hat{y}$ −direction, the exemplary susceptibility tensor is:

$$\overleftrightarrow{\chi} = \begin{bmatrix} \chi_v & 0 & \chi_0 \\ 0 & \chi_c & 0 \\ -\chi_0 & 0 & \chi_v \end{bmatrix} \tag{39}$$

In this relation, the diagonal part is $\chi_c = \chi_1$, and the other diagonal element, χ_v, is represented as:

$$\chi_v = \frac{\chi_c}{1 + \left(B_s/\widetilde{\Lambda}_1\right)^2} \approx \chi_c \tag{40}$$

The off-diagonal term, χ_0, due to free electrons is:

$$\chi_0 \cong \frac{\omega_{P_1}^2}{\omega^2 \widetilde{\Omega}_1} \frac{B_s/\widetilde{\Lambda}_1}{1 + \left(B_s/\widetilde{\Lambda}_1\right)^2} \approx \frac{\omega_{P_1}^2}{\omega^2 \widetilde{\Omega}_1} \frac{\vec{B}_s}{\widetilde{\Lambda}_1} = j \frac{\Omega_{P_1}^2}{\widetilde{\Omega}_1{}^2} \frac{\Omega_{cy}}{M_1^*} \tag{41}$$

while the normalized plasma frequency is $\Omega_{P_1} = \omega_{P_1}/\omega$, and the normalized free electron cyclotron frequency is $\Omega_{cy} = \frac{e\vec{B}_s}{m_e \omega}$. Also M_1^* is the ratio of the effective mass over rest mass of an electron, that is m_1^*/m_e. One can notice that the effective mass term explicitly exists in the off-diagonal element while it is implicitly present in the diagonal term. If we apply a static magnetic field, there would be splitting of the energy levels. The amount of splitting at around energy eigenvalue, E_k, can be obtained by using the formula in Eq. (42):

$$\gamma \hbar \vec{B}_z \quad \Rightarrow \quad splitted\ energies \quad \Rightarrow \quad \begin{matrix} E_k + \dfrac{\gamma \hbar \vec{B}_z}{2} \\ E_k - \dfrac{\gamma \hbar \vec{B}_z}{2} \end{matrix} \tag{42}$$

In Eq. (42), $\vec{B}_z$ is the external magnetic field along $\hat{z}$ −direction and γ is the gyromagnetic ratio, which is the ratio of the magnetic dipole moment to the angular momentum. γ is defined as $\not{g}e/(2m_e)$, where $\not{g}$ is the spectroscopic splitting factor [52]. The unit of the gyromagnetic ratio is $[Radian/s/T]$ or $[C/kg]$, where T refers to Tesla, and C refers to Coulomb. The spectroscopic splitting factor $\not{g}$ for an electron is 2.0023193043617 [53]. NIST provides the value of the electron gyromagnetic ratio as $1.760859708 \times 10^{11}\ Radian/s/T$, which is the same value in $[C/kg]$ unit [54]. After calculating Eq. (42), the cyclotron frequency of an electron for the magnetic field of 1 Tesla is obtained as $\omega_{cy} = 0.116\ meV$.

The Drude model was used in various studies to model the optical constants of metals and alloys [37]-[39]. According to the Drude model, there are only two unknown fit parameters for free electrons, which are, ${\omega_{P_1}}^2$ and γ_1. The parameters that are used in our ongoing paper is $\omega_{P_1} = 3.5\ eV$, and the low frequency conductance is $\sigma = 1.044 \times 10^7\ Siemens/m$. The calculated γ_1 from the formula for damping coefficient $\gamma_1 = \varepsilon_0 \omega_{P_1}^2/\sigma$ is $0.0158\ eV$. For the Drude model, the real part of the susceptibility for lower values of γ_1 can be shown as in Eq. (43):

$$Re(\chi_1) \approx -\frac{\omega_{P_1}^2}{\omega^2} \tag{43}$$

The real part is less affected from the low values of damping parameter than the imaginary part since it does not have any dependency of γ_1. The imaginary part can be illustrated as:

$$Im(\chi_1) \approx -\frac{\omega_{P_1}^2 \gamma_1}{\omega^3} \tag{44}$$

Since the imaginary part has an explicit multiplication of γ_1, it is more vulnerable to the lower values of the damping factor. The behavior of the real and imaginary parts of the susceptibility can be seen in Fig. 2.1, in which the real part reasonably fit to the experimental data up to 2 eV, while the imaginary part fails to converge.

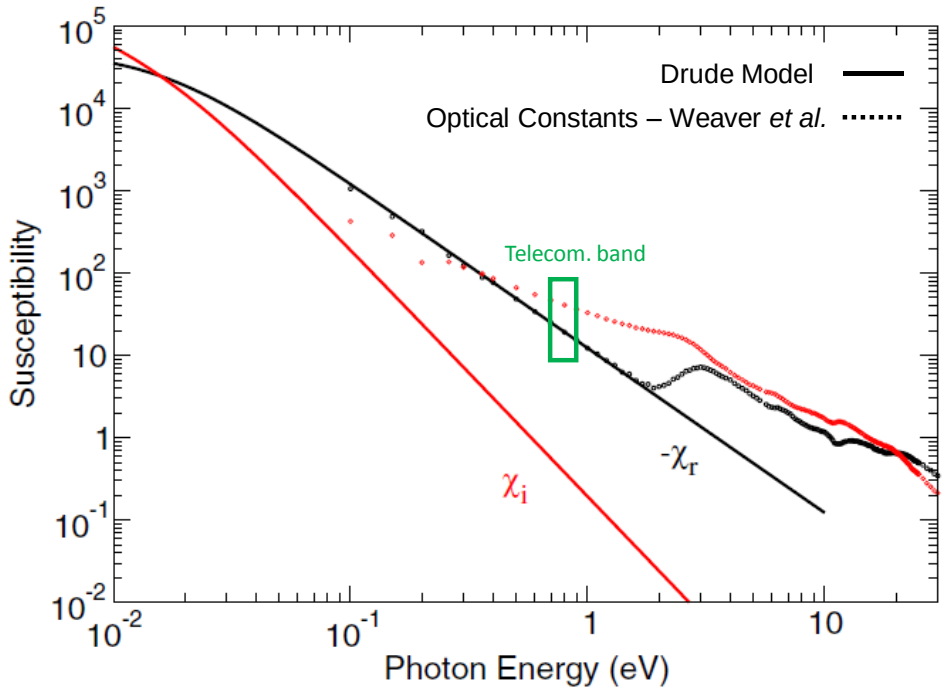

Figure 2.1 The real and imaginary parts of the susceptibility for the Drude model [55]. Experimental values of χ_i and $-\chi_r$ for iron are obtained from Weaver et al. [44]-[45].

The experimental data in Figure 2.1, for the optical constants up to $30\ eV$ is adapted from Weaver et al. [44]-[45]. The real part of the susceptibility for the Drude model shows agreeable behavior mainly in the infrared region up to $2\ eV$. We focus on the telecommunication band, which is from $\lambda = 1.55\ \mu m$ ($\approx 0.8\ eV$) to $\lambda = 1.3\ \mu m$ ($\approx 0.95\ eV$). The data for the susceptibility of iron at $\lambda = 1.55\ \mu m$ is $\chi \approx -19 - j41$ while the Drude model provides as $\chi \approx -19 - j0.37$. Therefore, the complex refractive index of iron from the susceptibility data would be $3.66 - j5.6$ whereas it would be $0.44 - j4.24$ from the free electron model. As can be inferred from these results, the Drude model cannot depict the complete behavior of the valence electrons for metals. Since the valence electrons might be either free or bound, there needs to be a more comprehensive model, which considers bound electrons as well. Lorentz Oscillator Model can be entitled as *Lorentz-Drude Model* (LD Model) since it is a correction of the Drude free electron model. According to LD Model, the collective anisotropic susceptibility due to all valence electrons of a metal is represented as:

$$\overleftrightarrow{\chi} = \sum_{i=1}^{Z} \overleftrightarrow{\chi}_i \tag{45}$$

where the susceptibility is defined as $\overleftrightarrow{\chi_i} = -\frac{\Omega_{P_i}^2}{\widetilde{\Omega}_i}\left(\overleftrightarrow{I} - \overleftrightarrow{B_i}\right)^{-1}$. In this equation, $\widetilde{\Omega}_i = (1 - \Omega_i^2 - j\Gamma_i)$, while $\Omega_i = \omega_i/\omega$ is the normalized resonant frequency, and $\Gamma_i = \gamma_i/\omega$ is the normalized collision frequency. In Eq. (45), Z refers to the number of electrons in a group while N_i is the number of electrons per unit volume within each group. N_1 is for free electrons, and the group of electrons starting from N_2 to N_Z are for bound electrons. Since iron has 26 electrons in one atom, the total number of electrons per unit volume cannot be higher than $26N_{Fe}$, while N_{Fe} is the number of atoms per cubic meter, which has a value of 8.46×10^{28}. The off-diagonal part of the susceptibility tensor can be illustrated as:

$$\chi_o(\omega) = -\sum_{i=1}^{Z} \chi_i(\omega) \frac{B_s/\widetilde{\Lambda}_i}{1 + \left(B_s/\widetilde{\Lambda}_i\right)^2} \tag{46}$$

$$\chi_o(\omega) \cong B_s \sum_{i=1}^{Z} \frac{\Omega_{P_i}^2}{\widetilde{\Omega}_i \widetilde{\Lambda}_i} = j\Omega_{cy} \sum_{i=1}^{Z} \frac{\Omega_{P_i}^2}{M_i^* \widetilde{\Omega}_i{}^2} \tag{47}$$

When there is no magnetic field, the susceptibility constant would be $\chi_i = -\frac{\Omega_{P_i}^2}{\widetilde{\Omega}_i}$. Therefore, the susceptibility tensor is defined as in Eq. (48), while the first group ($i = 1$) is due to free electrons, and the rest of them ($i = 2, 3, .., N$) are due to bound electron groups:

$$\overleftrightarrow{\chi} = \sum_{i=1}^{Z} \chi_i \left(\overleftrightarrow{I} - \overleftrightarrow{B}_i(\omega)\right)^{-1} \tag{48}$$

As stated earlier, free electrons have two unknown parameters; ${\omega_{P_1}}^2$ and γ_1, and bound electrons have three; ${\omega_{P_i}}^2$, γ_i and ω_i. ω_i refers to the resonant frequency of electrons. If the first free electron group is identified as $\{{\omega_{P_1}}^2, \gamma_1\} = \{X_1, X_2\}$, the second group (for the smallest resonant frequency of bound electrons) can be selected as $\{{\omega_{P_2}}^2, \gamma_2, \omega_2\} = \{X_3, X_4, X_5\}$. Therefore, for n group of electrons, the n^{th} group is shown as $\{{\omega_{P_n}}^2, \gamma_n, \omega_n\} = \{X_{(3n-3)}, X_{(3n-2)}, X_{(3n-1)}\}$. $\tau_1 = \frac{1}{2\pi\gamma_1}$ is the mean time between collisions of free electrons, whereas $\tau_i = \frac{1}{2\pi\gamma_i}$ is the lifetime at an energy level for bound electrons.

2.5 Brendel-Bormann (BB) Model

Brendel and Bormann proposed a model in order to describe the behavior of dielectric constants of amorphous solids in infrared region [34]. They proposed to use Voigt profile to model the optical constants. The main reason of compensating pure Lorentzian profile to the Voigt profile is to provide a reliable model for optical constants, since at room temperatures; LD model is stated as incorrect for elements and compounds [36], [58]. The superiority of Gaussian approach over Lorentzian has been explained in

terms of broadening approximation [59], [60]. At the invariability condition of oscillator strength and full width at half maximum (FWHM), the Lorentzian approach has wider wings compared to the Gaussian [42].

2.5.1 The superiority of BB model over LD model

As explained in previous sections, the complex susceptibility consists of the contributions from both intraband and interband transitions, which are free and bound electron contributions, respectively. The susceptibility function due to the bound electrons is a Lorentzian function that can be illustrated as in Eq. (49):

$$\chi_r^{(b)}(\omega) = \sum_{j=1}^{k} \frac{f_j \omega_P^2}{\left(j\omega\gamma_j + \omega_j^2 - \omega^2\right)} \tag{49}$$

where k is the number of oscillators, ω_P is the plasma frequency, ω_j is the transition frequency at critical points, f_j is the oscillator strength and $1/\gamma_j$ is the lifetime for each vibrational mode. The critical points are the turning points in the absorbance spectra of a specific material, which means that electrons make transitions to a higher-level empty energy band by absorbing required energy at around those critical points. The absorption (or emission) profiles are Lorentzian for the LD model. The other line shape function, which provides better broadening approximation than Lorentzian, is Gaussian broadening [36], [42], [57]. An exemplary Gaussian function can be shown as in Eq. (50):

$$\chi_j(\omega) = \frac{1}{\sigma_j\sqrt{2}} \int_{-\infty}^{+\infty} exp\left(-\frac{\left(\omega - \omega_j\right)^2}{2{\sigma_j}^2}\right) d\omega \tag{50}$$

In that equation, ω_j refers to the mean, which is the peak point, and σ_j refers to standard deviation around that peak point, which quantifies the amount of variation from the peak value of the line. The decay rate for the Lorentzian function is $\approx \frac{1}{\left(\omega-\omega_j\right)^2}$, for which the large amount of emission (or absorption) is under the wings of the line-shape [56]. However, for the Gaussian profile, the decay rate is proportional to $\approx \exp\left(-\left(\omega - \omega_j\right)^2\right)$, which provides a rapid decline in the line-shape. Accordingly, there would be very small emission under the wings of the line for the Gaussian function [56]. Therefore, we can theoretically conclude that the Gaussian profile has less amounts of broadening than the Lorentzian profile. Now, we could discuss about the Voigt type of line broadening which is the convolution of Lorentzian and Gaussian broadening mechanisms [34], [56]. The convolution of those two functions can be expressed as [34], [42]:

$$\chi_j(\omega) = \frac{1}{\sigma_j\sqrt{2\pi}} \int_{-\infty}^{+\infty} exp\left(-\frac{\left(\bar{\omega}_j - \omega_j\right)^2}{2{\sigma_j}^2}\right) \frac{f_j\omega_P^2}{\left(j\omega\gamma_j + {\bar{\omega}_j}^2 - \omega_j^2\right)} d\bar{\omega}_j \tag{51}$$

By the help of this convolution integral, we have chance to select the amount of broadening which enables to have nearly Gaussian or purely Lorentzian profiles. Nearly Gaussian can

be obtained by the determination of $\gamma_j \approx 0$, and pure Lorentzian can be obtained by the definition of $\sigma_j \approx 0$ [42].

2.5.2 Electric Susceptibility from the BB Model

In the Brendel-Bormann (BB) model of bound electrons, one Lorentz oscillator is compensated with a superposition of numbers of oscillators described as in Eq. (51). Gaussian function decides the numbers of harmonic oscillators. Brendel and Bormann describe that model just for amorphous solids in IR region [34], but seven years later, Rakic *et al.* shows that the same model is applicable to various kinds of materials containing metals in any regions up to 6 eV [42].

The infinitesimal resonant frequencies are accepted as random variables, $\bar{\omega}_j$ which are distributed around the main oscillator frequency, ω_j while $j = 2, 3 \ldots Z$. Since the Gaussian distributions are independent for each oscillator frequency, the joint probability density function is illustrated as:

$$p(\bar{\omega}_2, \bar{\omega}_3, \ldots \bar{\omega}_Z) = \frac{1}{(2\pi)^{\frac{(Z-1)}{2}} \sigma_2 \sigma_3 \ldots \sigma_Z} e^{-\left[\frac{(\bar{\omega}_2-\omega_2)^2}{2\sigma_2^2}+\frac{(\bar{\omega}_3-\omega_3)^2}{2\sigma_3^2}+\cdots+\frac{(\bar{\omega}_Z-\omega_Z)^2}{2\sigma_Z^2}\right]} \tag{52}$$

The expected value of the collective susceptibility tensor is in Eq. (53):

$$\langle \overleftrightarrow{\chi} \rangle = \chi_1(\omega)\left(\overleftrightarrow{I} - \overleftrightarrow{B}_1(\omega)\right)^{-1} + \sum_{j=2}^{Z} \frac{1}{\sqrt{2\pi}\sigma_j} \int_{-\infty}^{+\infty} \chi_j(\omega, \bar{\omega}_j)\left(\overleftrightarrow{I} - \overleftrightarrow{B}_j(\omega, \bar{\omega}_j)\right)^{-1} e^{-\frac{(\bar{\omega}_j - \omega_j)^2}{2\sigma_j^2}} d\bar{\omega}_j \quad (53)$$

while the first term on the right hand side is due to free electrons and the second one is due to bound electrons. In addition to that, the expected values of the diagonal and the off-diagonal elements can be seen as in Eq.'s (54) and (55):

$$\langle \overleftrightarrow{\chi}_c \rangle = -\frac{\Omega_{P_1}^2}{\widetilde{\Omega}_1} - \sum_{j=2}^{Z} \Omega_{P_j}^2 \langle \frac{1}{\widetilde{\Omega}_j} \rangle \quad (54)$$

$$\langle \overleftrightarrow{\chi}_o \rangle = \frac{\Omega_{P_1}^2}{\widetilde{\Omega}_1} \frac{B_s/\widetilde{\Lambda}_1}{1 + \left(B_s/\widetilde{\Lambda}_1\right)^2} + \sum_{j=2}^{Z} \Omega_{P_j}^2 \langle \frac{1}{\widetilde{\Omega}_j} \frac{B_s/\widetilde{\Lambda}_j}{1 + \left(B_s/\widetilde{\Lambda}_j\right)^2} \rangle = j\Omega_{cy}\left(\frac{\Omega_{P_1}^2}{M_1^* \widetilde{\Omega}_1{}^2} + \sum_{j=2}^{Z} \frac{\Omega_{P_j}^2}{M_j^*} \langle \frac{1}{\widetilde{\Omega}_j{}^2} \rangle\right) \quad (55)$$

$\langle \overleftrightarrow{\chi}_c \rangle$ is the diagonal element which does not have any magnetic bias dependency, while $\langle \overleftrightarrow{\chi}_v \rangle$ in Eq. (39) has some dependency to it. However, the dependency of $\langle \overleftrightarrow{\chi}_v \rangle$ to the magnetic bias is too small, therefore, we can accept that $\langle \overleftrightarrow{\chi}_v \rangle \cong \langle \overleftrightarrow{\chi}_c \rangle$.

2.6 Methodology and Discussion

As an extension to LD model, BB model suggests having a Gaussian distribution consolidated at resonant frequencies ω_j with a standard deviation of σ. Despite the fact that LD model has 3 unknown parameters, BB model has an additional 4th parameter that is σ_j for the j^{th} oscillator. Considering that there are 2 unknowns in the first free electron group, the $X*$ vector for the second group of electrons would be defined as $\{{\omega_{P_2}}^2, \gamma_2, \omega_2, \sigma_2\} = \{X_3, X_4, X_5, X_6\}$ for the BB model. Thus, the $X*$ vector for n^{th} group can be represented as $\{{\omega_{P_n}}^2, \gamma_n, \omega_n, \sigma_n\} = \{X_{(4n-5)}, X_{(4n-4)}, X_{(4n-3)}, X_{(4n-2)}\}$.

In order to fit the susceptibility from our proposed model to the experimental data, a mean-square relative error function is defined as:

$$E(X*) = \sum_m W(\omega_m)[E_r^2(X*, \omega_m) + E_i^2(X*, \omega_m)] \tag{56}$$

while the real part is:

$$E_r(X*, \omega_m) = \frac{[\chi_r(X*, \omega_m) - \chi_{re}(\omega_m)]}{\chi_{re}(\omega_m)} \tag{57}$$

The real part of the susceptibility from our model is $\chi_r(X*, \omega_m)$, and the experimental data is $\chi_{re}(\omega_m)$. The imaginary part of the error function in Eq. (56) is:

$$E_i(X*, \omega_m) = \frac{[\chi_i(X*, \omega_m) - \chi_{ie}(\omega_m)]}{\chi_{ie}(\omega_m)} \tag{58}$$

when the imaginary part of the susceptibility from our model is $\chi_i(X*, \omega_m)$ and the experimental data is $\chi_{ie}(\omega_m)$. $W(\omega_m) = (\omega_{m+1} - \omega_{m-1})/(2\omega_m)$ is the weight function, which also helps to evenly distribute the sparse data and the bunched data. NAG Mark 23 optimization library routine; E04LBF is used for the minimization purposes of Eq. (56) [61]. Brendel and Bormann developed the model for amorphous solids in the IR region by assuming a set of resonant frequencies around the main absorption line. Then, Rakic *et al.* utilized that model in a much broader spectrum up to $6\ eV$ for various metals. However, he does not show the behavior of the BB model for iron. The aim of this work is to show the superiority of the improved BB model for finding optical constants of iron metal. For the sake of comparison with Rakic's work, we have selected gold to analyze the behavior of our model. In section 2.6.1, the analysis for gold data can be observed and in section 2.6.2, the model is investigated for the case of iron.

2.6.1 Dielectric Constant of Gold

Table 2.1 lists the output of appropriate BB model parameters for gold. The first three columns are the optimization results from Rakic's work [42], while the last three columns are the parameters from our proposed model. The experimental data of gold is obtained from Handbook of Optical Constants of Solids [62].

Table 2.1 The calculated parameters of gold using the BB model. The first three columns are the parameters from Rakic et al. [42], and the last three columns are from our proposed BB model. All terms are in the eV unit excluding f_j.

$\boldsymbol{X_1}$	$\boldsymbol{\omega_P}$	9.030	$\boldsymbol{X_1}$	$\boldsymbol{\omega_{P_1}^2}$	61.754
$\boldsymbol{X_2}$	f_1	0.770	X_2	γ_1	0.0521
$\boldsymbol{X_3}$	γ_1	0.050			
$\boldsymbol{X_4}$	f_2	0.054	X_3	$\omega_{P_2}^2$	4.4306
$\boldsymbol{X_5}$	γ_2	0.074	X_4	γ_2	0.0643
$\boldsymbol{X_6}$	ω_2	0.218	X_5	ω_2	0.0100
$\boldsymbol{X_7}$	σ_2	0.742	X_6	σ_2	0.7954
$\boldsymbol{X_8}$	f_3	0.050	X_7	$\omega_{P_3}^2$	4.7123
$\boldsymbol{X_9}$	γ_3	0.035	X_8	γ_3	0.0001
$\boldsymbol{X_{10}}$	ω_3	2.885	X_9	ω_3	2.8913
$\boldsymbol{X_{11}}$	σ_3	0.349	X_{10}	σ_3	0.3678
$\boldsymbol{X_{12}}$	f_4	0.312	X_{11}	$\omega_{P_4}^2$	35.859
$\boldsymbol{X_{13}}$	γ_4	0.083	X_{12}	γ_4	0.0001

$\boldsymbol{X_{14}}$	ω_4	4.069	X_{13}	ω_4	4.2778
$\boldsymbol{X_{15}}$	σ_4	0.830	X_{14}	σ_4	0.8598
$\boldsymbol{X_{16}}$	f_5	0.719	X_{15}	${\omega_{P_5}}^2$	42.881
$\boldsymbol{X_{17}}$	γ_5	0.125	X_{16}	γ_5	0.0001
$\boldsymbol{X_{18}}$	ω_5	6.137	X_{17}	ω_5	6.1026
$\boldsymbol{X_{19}}$	σ_5	1.246	X_{18}	σ_5	0.6107
$\boldsymbol{X_{20}}$	f_6	1.648	X_{19}	${\omega_{P_6}}^2$	–
$\boldsymbol{X_{21}}$	γ_6	0.179	X_{20}	γ_6	–
$\boldsymbol{X_{22}}$	ω_6	27.970	X_{21}	ω_6	–
$\boldsymbol{X_{23}}$	σ_6	1.795	X_{22}	σ_6	–

Rakic *et al.* utilized 6 groups of electrons which gives a total of 23 unknowns, yet ours has 5 electron groups and a total of 18 unknowns. In addition to this, our model uses 1 less unknown for free electrons, since the multiplication of the oscillator strength and the plasma frequency for all groups is accepted as a single variable, $\omega_{P_i}^2 = \omega_P^2 f_i$, without the constraint of $\sum f_i = 1$. A comparative plot for the dielectric constant of gold can be seen in

Figure 2.2 The experimental data, Rakic's model and the proposed model of real and imaginary parts of the dielectric constants are shown.

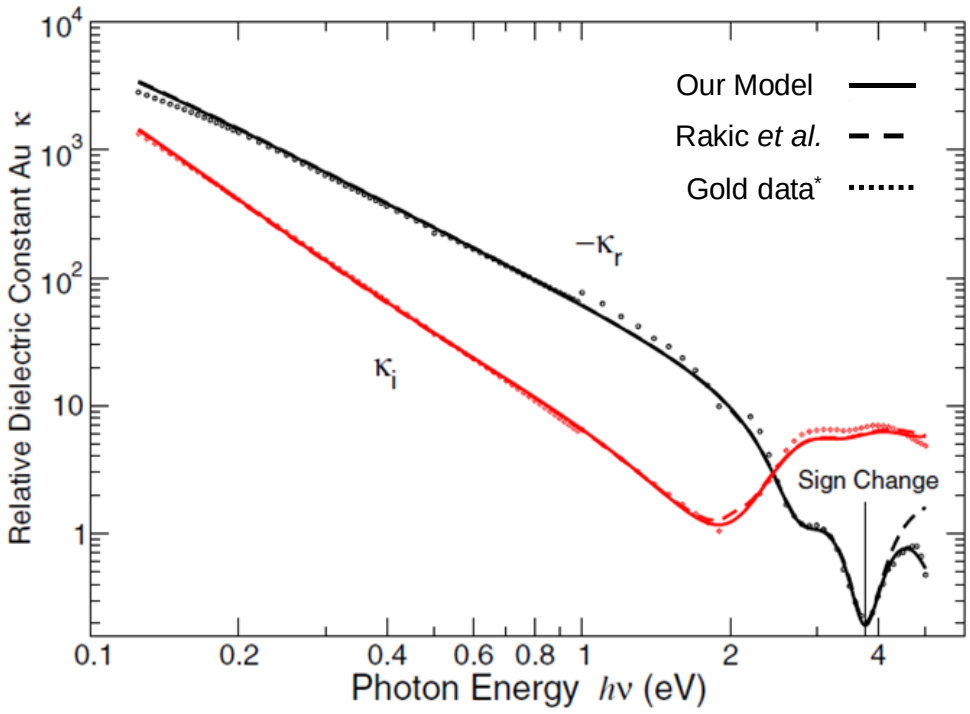

Figure 2.2 The real, $-\kappa_r$, and the imaginary parts, κ_i, of the dielectric constant for gold. Small round and square shape circles are for the experimental data of real and imaginary parts, respectively [62]. The solid curves refer to our model, while dashed ones refer to Rakic [42].

The most prominent interband transitions for gold is at $650\ nm$ and $500\ nm$, which refer to $1.9\ eV$ and $2.45\ eV$, respectively [63]-[65]. As shown in Figure 2.2, the improved model fits accurately at around both transitions. Our model is comparable to Rakic *et al.*'s up to

the energies of $4\ eV$. For the photon energies greater than $4\ eV$, our model is superior to Rakic *et al.*'s model.

2.6.2 Susceptibility of Iron

The optimization parameters of proposed BB model for iron can be seen in Table 2.2. Since Rakic did not apply the BB model to iron, only our own results are tabulated.

Table 2.2 The calculated optimization parameters of iron by using the proposed BB model (in eV unit)

$\boldsymbol{X_1}$	$\boldsymbol{\omega_{P_1}^2}$	11.50
$\boldsymbol{X_2}$	γ_1	0.0084
$\boldsymbol{X_3}$	$\omega_{P_2}^2$	163.8
$\boldsymbol{X_4}$	γ_2	5.051
$\boldsymbol{X_5}$	ω_2	0.2060
$\boldsymbol{X_6}$	σ_2	0.0006
$\boldsymbol{X_7}$	$\omega_{P_3}^2$	19.50
$\boldsymbol{X_8}$	γ_3	1.214

$\boldsymbol{X_9}$	ω_3	2.464
$\boldsymbol{X_{10}}$	σ_3	0.3078
$\boldsymbol{X_{11}}$	${\omega_{P_4}}^2$	9.758
$\boldsymbol{X_{12}}$	γ_4	2.169
$\boldsymbol{X_{13}}$	ω_4	6.301
$\boldsymbol{X_{14}}$	σ_4	0.0003
$\boldsymbol{X_{15}}$	${\omega_{P_5}}^2$	6.077
$\boldsymbol{X_{16}}$	γ_5	0.0000
$\boldsymbol{X_{17}}$	ω_5	8.892
$\boldsymbol{X_{18}}$	σ_5	1.032
$\boldsymbol{X_{19}}$	${\omega_{P_6}}^2$	25.25
$\boldsymbol{X_{20}}$	γ_6	4.014
$\boldsymbol{X_{21}}$	ω_6	12.25
$\boldsymbol{X_{22}}$	σ_6	0.0072

$\boldsymbol{X_{23}}$	${\omega_{P_7}}^2$	268.5
$\boldsymbol{X_{24}}$	γ_7	24.06
$\boldsymbol{X_{25}}$	ω_7	19.47
$\boldsymbol{X_{26}}$	σ_7	0.0077

As tabulated for gold in Table 2.1, the square of the plasma frequency, $\omega_{P_i}^2$, is assigned to be $\omega_P^2 f_i$ for the free electron group of iron in Table 2.2, which helps with the parsimony of having one fewer parameter.

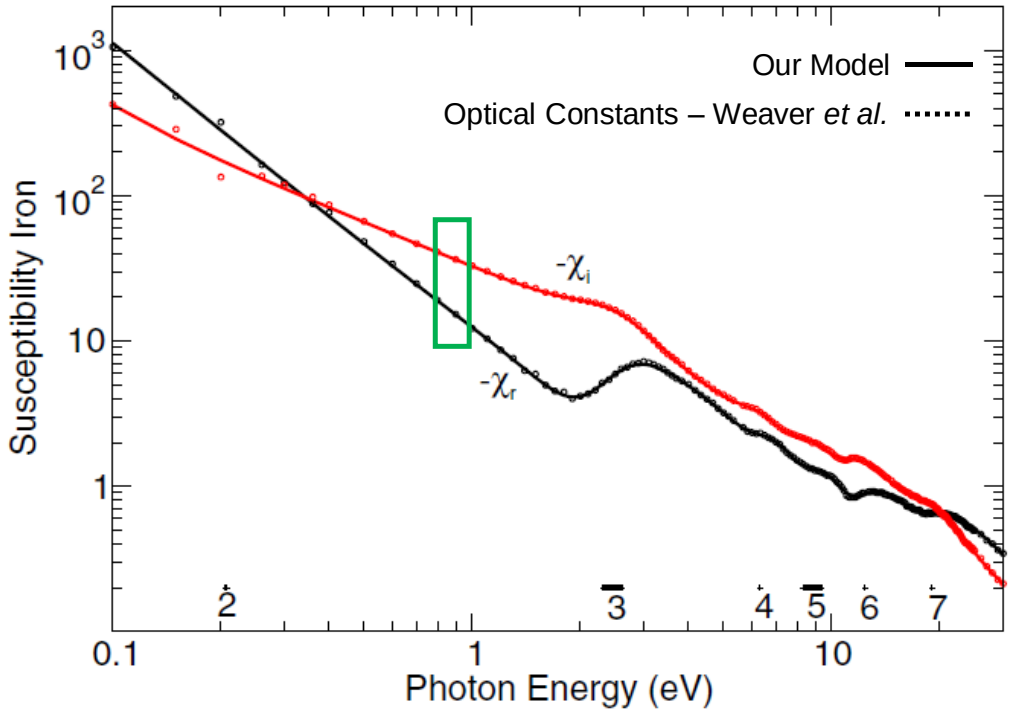

Figure 2.3 The real, χ_r and imaginary parts, χ_i of the susceptibility of iron using the proposed BB model [55]. The small circles are the experimental values obtained by Weaver et al. [44]-[45].

The experimental data for iron is obtained from Weaver *et al.* [44]-[45]. In Figure 2.3, the numbers above the abscissa refer to the transition frequencies, and the dashes above the numbers refer to the comparative amounts of line broadenings. It is also inferred that our model fits to the iron data at the strongest interband transition of $\sim 2.4\ eV$ [66]. In addition to that, Figure 2.3 proves that a perfect fit for iron up to $30\ eV$ can be obtained using our proposed BB model.

2.7 Conclusion

The optical properties of iron and gold are analyzed. At first, the susceptibility of iron is modeled by using the Drude free electron theory as seen in Figure 2.1. The large discrepancies among the experimental data and the Drude model show that Drude model cannot depict the behavior of all electrons in an atom. The alternative approach to free electron model is the Lorentz-Drude model, which introduces the concept of inter-band transitions at critical points. However, the Lorentzian profile have wider wings compared to the Gaussian line-shape, which directs us to use the convolution of Lorentzian and Gaussian profiles. Brendel and Bormann utilized this Voigt line shape to model the optical constants of amorphous solids in the near-IR region [34]. They suggested having a set of resonant frequencies around the main absorption line. Then, Rakic *et al.* used the same model for higher energies up to 6 eV for various metals [42].

In this work, we improve the Rakic *et al.*'s BB model by reducing the number of unknowns and relaxing a constraint from the system [55]. As a benchmark study, the optimization parameters for gold using our proposed model is compared against the parameters of Rakic *et al.* in Table 2.1. Furthermore, the better accuracy of the proposed model for gold can be clearly seen in Figure 2.3 for the photon energies greater than 4 eV. In this study, we showed the applicability of BB model to Iron up to 30 eV. To the best of our knowledge, we are the first in literature to fit the BB model to Iron. The optimization results for iron can be seen in Table 2.2. The largest electron concentration is at the 7^{th}

group of electrons. The real and imaginary parts of the susceptibility of iron can be seen in Figure 2.3. Based on these results, it can be claimed that our proposed model accurately fits to iron data up to 30 eV.

CHAPTER 3

3 MAGNETO-OPTIC EFFECTS

3.1 Introduction to Magneto-optic Effects

The interaction of light and matter has attracted a lot of attention in the physical sciences literature. When a magnetic field is applied to the matter, the concept of magneto-optics emerges because of the interaction of light with matter. When the light interacts with the magnetized matter, the polarization plane of linearly polarized light is rotated, which was discovered by Faraday in 1845 [68]-[69]. Soon after Faraday's discovery, John Kerr revealed the analogous effect in reflection in 1876 [69]-[70]. He found that the polarization plane of the linearly polarized light had rotated after reflection from the magnetized matter. He discovered the polar magneto-optic Kerr effect (P-MOKE) first and found the longitudinal MOKE two years later [69].

Although these magneto-optic effects showed that light has an electromagnetic nature, there was still a lack of information about its microscopic origin until 1897 [69]-[70]. Then, Zeeman discovered the splitting of the spectral lines into two circularly polarized components under the influence of a longitudinally applied magnetic field. This is called the *Zeeman Effect*. For the case of transversely applied magnetic field, he observed that the spectral lines split into three linearly polarized components of light. The refractive indices of the right and left circularly polarized light for the longitudinal Zeeman effect, as

well as the linearly polarized components of light for the transverse Zeeman effect are different from each other. The difference of refractive indices, called birefringence, results in the rotation of the polarization plane for the above-mentioned magneto-optic effects. Because of the discoveries of these Normal Zeeman Effects, the microscopic origin of the magneto-optics began to be understood. Soon after the observation of Normal Zeeman Effects, the Anomalous Zeeman Effect was discovered. This refers to the concept of splitting of an energy level into its number of components under the influence of magnetic field. The meaning of the Anomalous Zeeman Effect would be better comprehended with the emergence of quantum mechanics, since it encapsulates the concept of spin.

Based on the above explanations, we understand that there is also a spectral line shift of the absorption coefficients for the two orthogonal polarizations, in addition to the splitting of refractive indices under an applied magnetic field. Therefore, there is a dichroism concept in Zeeman effect that points out the difference between the absorption coefficients of the two orthogonal polarizations in addition to the birefringence [70]-[71].

As noted at the beginning of this chapter, the explanation of the magneto-optic effects lies under the Zeeman effect. Accordingly, the rotations of the polarization planes (upon light going through or reflecting from a magnetic substance) indicate that orthogonal polarizations have different refractive indices as well as different absorption coefficients. The linearly polarized light is composed of RCP (right-circularly polarized) and LCP (left-circularly polarized) waves which both have equal refractive indices, n_0. Therefore, for a

specific emission, there is one spectral line. According to the above-mentioned Zeeman Effect, this line of energy splits into two if there is a longitudinally applied magnetic field. Now, we know that it is the same as having two different refractive indices for the two orthogonal polarizations which are RCP and LCP light-waves. The refractive indices can be named as n_+ and n_- for the RCP and LCP waves, respectively. Because of the birefringence of the medium, there is a phase shift, δ after traveling for a length, L, which is:

$$\delta = kL = \frac{2\pi}{\lambda_0}(n_+ - n_-)L \tag{59}$$

while k is the wave-vector, and λ_0 is the wavelength when there is no magnetic field. For the case of *Faraday Effect*, that phase difference causes the polarization plane to rotate for a degree of θ [71]:

$$\theta = \frac{\omega}{2c}(n_+ - n_-)L \tag{60}$$

while ω is the angular frequency, and c is the speed of light. There are two other magneto-optic effects known as the Voigt Effect and the Cotton-Mouton Effect. *The Voigt Effect* occurs when the magnetic field is perpendicular to the light propagation, which leads to the transverse Zeeman Effect. Likewise, the emission lines of the linearly polarized light splits into three linearly polarized spectral lines. One is the un-displaced component parallel to the magnetic field, the other two are perpendicular to the magnetic field and

equally distributed around the un-displaced one [70]. The spectral splitting is the result of the birefringence between the perpendicular and parallel components which can be represented as, $n_{\perp}$ and $n_{\parallel}$.

The Cotton-Mouton Effect is a magneto-optic effect in liquids, which was discovered in 1907. The source of birefringence in this case is the transversely applied magnetic field. The Cotton-Mouton Effect is much stronger than the Voigt Effect. For the Voigt and Cotton-Mouton Effects, the birefringence comes from the phase shift between the parallel and perpendicular components -after traveling for a length L- which is defined as [71]:

$$\delta = \frac{\omega}{c}(n_{\parallel} - n_{\perp})L \tag{61}$$

For the *Magneto-optic Kerr Effect* (MOKE), the plane of polarization of the linearly polarized light had rotated after reflection from the magnetized material. The Fresnel reflection coefficients are the main parameters for the rotation of polarization plane. Since the MOKE depends on the direction of applied magnetic field, the representations for the Kerr rotations differ for each direction. The equations for the Kerr Effect will be analyzed in the upcoming parts of this chapter.

3.2 The Solutions of the Refractive Index for the Faraday and Voigt Effects

In order to find the normal mode solutions for Faraday and Voigt geometries, we can consider the time harmonic plane-wave solutions for the electric field and the magnetic flux density as $\vec{E}(\boldsymbol{r},t) = E_0 e^{j(\omega t - \boldsymbol{k}.\boldsymbol{r})}$ and $\vec{B}(\boldsymbol{r},t) = B_0 e^{j(\omega t - \boldsymbol{k}.\boldsymbol{r})}$, respectively. When electric current density, $\vec{J} = 0$, the two of the Maxwell equations are as follows:

$$\nabla \times \vec{E} = -\frac{\partial \vec{B}}{\partial t} \tag{62}$$

$$\nabla \times \vec{H} = \frac{\partial \vec{D}}{\partial t} \quad \rightarrow \quad \nabla \times \frac{\vec{B}}{\mu_0} = \varepsilon \frac{\partial \vec{E}}{\partial t} \quad \rightarrow \quad \nabla \times \vec{B} = \frac{1}{c^2}\frac{\partial \vec{E}}{\partial t} \tag{63}$$

The velocity of light is defined as $c = \frac{1}{\sqrt{\mu\varepsilon}}$ and $\mu = \mu_0$ for optical frequencies [72]. Furthermore, ε is defined as $\varepsilon = \varepsilon_0 \epsilon_r$ for isotropic materials while ε_0 is vacuum permittivity and ϵ_r is the dielectric constant of the medium. However, ϵ_r would be a dielectric tensor, $\overleftrightarrow{\epsilon_r}$, for anisotropic media which is the medium for magneto-optic materials. If we apply the curl operator to Eq. (62), the new relation is:

$$\nabla \times \nabla \times \vec{E} = -\frac{\partial\left(\nabla \times \vec{B}\right)}{\partial t} \tag{64}$$

After simplifying the curl of curl operator and inserting Eq. (63) into Eq. (64), the wave equation would be as follows:

$$\nabla\left(\nabla.\vec{E}\right) - \nabla^2\vec{E} = -\frac{\partial\left(\nabla\times\vec{B}\right)}{\partial t} \tag{65}$$

The first term in Eq. (65) is a scalar times unit vector while the second term is a Laplacian of the electric field vector which is equal to $(\nabla.\nabla)\vec{E}$. According to the plane wave solutions for the electric field and magnetic flux density, Maxwell Equations can be shown as [73]:

$$\nabla.\vec{E} = -jk.\vec{E} \tag{66}$$

$$\nabla\times\vec{B} = -jk\times\vec{B} \tag{67}$$

Therefore, the wave equation in Eq. (65) can be rewritten as:

$$(\mathbf{k}.\mathbf{k})\vec{E} - k^2\left(\overleftrightarrow{\mathrm{I}}.\vec{E}\right) = \omega^2\mu_0\varepsilon_0\overleftrightarrow{\epsilon_r}\vec{E} = k_0^2\overleftrightarrow{\epsilon_r}\vec{E} \tag{68}$$

where $\overleftrightarrow{\mathrm{I}}$ is the unit dyadic and $\overleftrightarrow{\epsilon_r}$ is the dielectric tensor for anisotropic media. $(\mathbf{k}.\mathbf{k})$ is a dyadic which can be seen in Eq. (69):

$$(\mathbf{k}.\mathbf{k}) = \begin{bmatrix} k_xk_x & k_xk_y & k_xk_z \\ k_yk_x & k_yk_y & k_yk_z \\ k_zk_x & k_zk_y & k_zk_z \end{bmatrix} \tag{69}$$

Let's find the solutions for the propagation along $\hat{z}$ −direction: The wavevector $\boldsymbol{k}$ is defined as $\boldsymbol{k} = k_z\hat{z}$ while $k_z k_z = k^2$. For the case of Voigt Effect in which the magnetic bias is perpendicular to the propagation direction, the dielectric tensor $\overleftrightarrow{\epsilon_r}$ is shown as:

$$\overleftrightarrow{\epsilon_r} = \begin{bmatrix} \epsilon_v & 0 & \epsilon_o \\ 0 & \epsilon_c & 0 \\ -\epsilon_o & 0 & \epsilon_v \end{bmatrix} \tag{70}$$

while the direction of the magnetic field is along $\hat{y}$ −direction and the off-diagonal element, ϵ_o, is a complex number (different than ε_0 which is vacuum permittivity). Considering Eq. (70), Eq. (68) is

$$\left[\begin{bmatrix} 0 & 0 & 0 \\ 0 & 0 & 0 \\ 0 & 0 & k^2 \end{bmatrix} - k^2 \begin{bmatrix} 1 & 0 & 0 \\ 0 & 1 & 0 \\ 0 & 0 & 1 \end{bmatrix} - k_0^2 \begin{bmatrix} \epsilon_v & 0 & \epsilon_o \\ 0 & \epsilon_c & 0 \\ -\epsilon_o & 0 & \epsilon_v \end{bmatrix}\right] . \vec{E} = 0 \tag{71}$$

To get nontrivial solutions for k, the determinant of the matrix in Eq. (72) must be equal to zero:

$$det \begin{bmatrix} -k^2 - k_0^2\epsilon_v & 0 & -k_0^2\epsilon_o \\ 0 & -k^2 - k_0^2\epsilon_c & 0 \\ k_0^2\epsilon_o & 0 & -k_0^2\epsilon_v \end{bmatrix} = 0 \tag{72}$$

The normal mode solutions of k for the case of Voigt Effect is:

$$k_{\parallel} = \pm j\sqrt{\epsilon_c}k_0$$

$$k_{\perp} = \pm j\sqrt{\frac{{\epsilon_o}^2 + {\epsilon_v}^2}{\epsilon_v}}k_0 \tag{73}$$

Since $\boldsymbol{k} = \boldsymbol{n}k_0$, the two normal mode solutions for the refractive index can be shown as:

$$n_{\parallel} = \pm j\sqrt{\epsilon_c}$$

$$n_{\perp} = \pm j\sqrt{\frac{{\epsilon_o}^2 + \varepsilon_v^2}{\epsilon_v}} \tag{74}$$

For the Faraday case, the magnetic field is parallel to the light propagation (both in the $\hat{z}$ −direction). Therefore, the dielectric tensor, $\overleftrightarrow{\epsilon_r}$ would be represented as:

$$\overleftrightarrow{\epsilon_r} = \begin{bmatrix} \epsilon_v & \epsilon_o & 0 \\ -\epsilon_o & \epsilon_v & 0 \\ 0 & 0 & \epsilon_c \end{bmatrix} \tag{75}$$

And the wave equation in Eq. (68) is:

$$\left[\begin{bmatrix} 0 & 0 & 0 \\ 0 & 0 & 0 \\ 0 & 0 & k^2 \end{bmatrix} - k^2\begin{bmatrix} 1 & 0 & 0 \\ 0 & 1 & 0 \\ 0 & 0 & 1 \end{bmatrix} - k_0^2\begin{bmatrix} \epsilon_v & \epsilon_o & 0 \\ -\epsilon_o & \epsilon_v & 0 \\ 0 & 0 & \epsilon_c \end{bmatrix}\right].\vec{E} = 0 \tag{76}$$

The secular determinant is as follows:

$$det\begin{bmatrix} -k^2 - k_0^2\epsilon_v & -k_0^2\epsilon_o & 0 \\ k_0^2\epsilon_o & -k^2 - k_0^2\epsilon_v & 0 \\ 0 & 0 & -k_0^2\epsilon_c \end{bmatrix} = 0 \quad (77)$$

The normal mode solutions for k is:

$$k_{\pm} = \pm k_0\sqrt{-\epsilon_v \pm j\epsilon_o} \quad (78)$$

The two normal mode solutions of the refractive indices for Faraday geometry are:

$$n_{\pm} = \pm\sqrt{-\epsilon_v \pm j\epsilon_o} \quad (79)$$

3.3 Magneto-optic Kerr Effect (MOKE)

Another important magneto-optic effect is the Kerr Effect, which takes place when light reflects from a magnetic material. The applied magnetization affects the physical properties of light that is reflected from the substance. Magneto-optic Kerr effect (MOKE) is classified according to the direction of the applied magnetic field, which consists of a magnetic and a non-magnetic medium. In the polar MOKE (P-MOKE), the magnetization is perpendicular to the sample surface as seen in Figure 3.1.

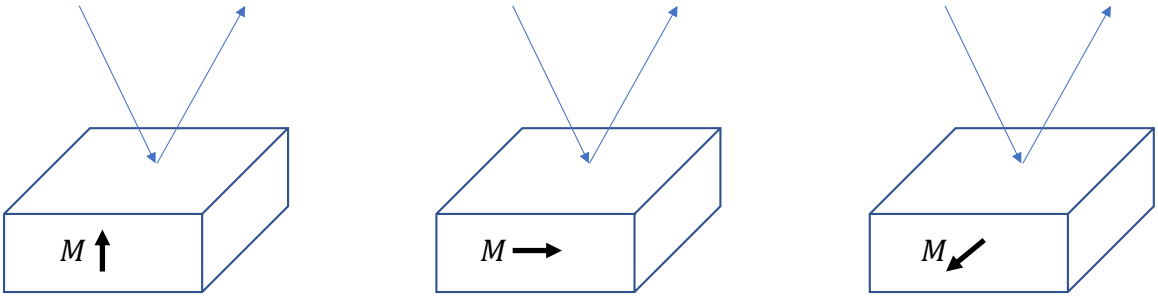

(a) Polar (b) Longitudinal (c) Transverse

Figure 3.1 (a) Polar, (b) longitudinal, and (c) transverse MOKE configurations

In the case of longitudinal MOKE (L-MOKE), the magnetization is parallel to the sample surface and the plane of incidence as well. The only MO Kerr Effect type which has perpendicular magnetization to the plane of incidence is the transverse MOKE (T-MOKE). For the cases of P-MOKE and L-MOKE, there are two types of changes of the linearly polarized light upon reflection from a magnetized material: One is the rotation of the plane of polarization for an angle of θ_K, called Kerr rotation, the other one is the elliptical polarization of the reflected light which is defined with the Kerr ellipticity, ε_K. The incident linearly polarized light is composed of right (RCP) and left (LCP) circularly polarized light. Since the phase differences upon reflection from magnetic medium are different for the RCP and LCP lights, linearly polarized light would be elliptically polarized after reflection

from a magnetic surface. The Kerr ellipticity, ε_K is the ratio of the minor axis to the major axis of the ellipse. The combined complex Kerr angle is illustrated as in Eq. (80):

$$\phi_K = \theta_K + i\varepsilon_K \tag{80}$$

Complex Kerr angle is found from the analysis of the Fresnel reflection coefficients, which are simple for normally incident light. However, the equations for oblique incidence are somewhat complicated since they consist of parallel (p −polarized) and perpendicular (s −polarized) electric field components. For the sake of simplicity, the two diagonal elements ε_c and ε_v of the dielectric tensor in Eq. (11), can be considered nearly equal, $\varepsilon_c \cong \varepsilon_v$. The exemplary dielectric tensor for the magnetic field along $\hat{y}$ −direction is defined by several authors [74]-[76] as:

$$\overleftrightarrow{\epsilon_r} = \varepsilon_c \begin{bmatrix} 1 & 0 & i\mathbb{Q} \\ 0 & 1 & 0 \\ -i\mathbb{Q} & 0 & 1 \end{bmatrix}$$

while complex off-diagonal element, $\mathbb{Q}$ is defined as $\mathbb{Q} = i\frac{\varepsilon_o}{\varepsilon_c}$.

3.4 Parameters for The Types of MOKE

The general structure for the MO Kerr Effect can be seen in Figure 3.2. n_0 is the refractive index of the non-magnetic medium, while n_1 is the refractive index of the magnetic medium. θ_i, θ_r, and θ_t are the incidence, reflection and transmission angles, respectively.

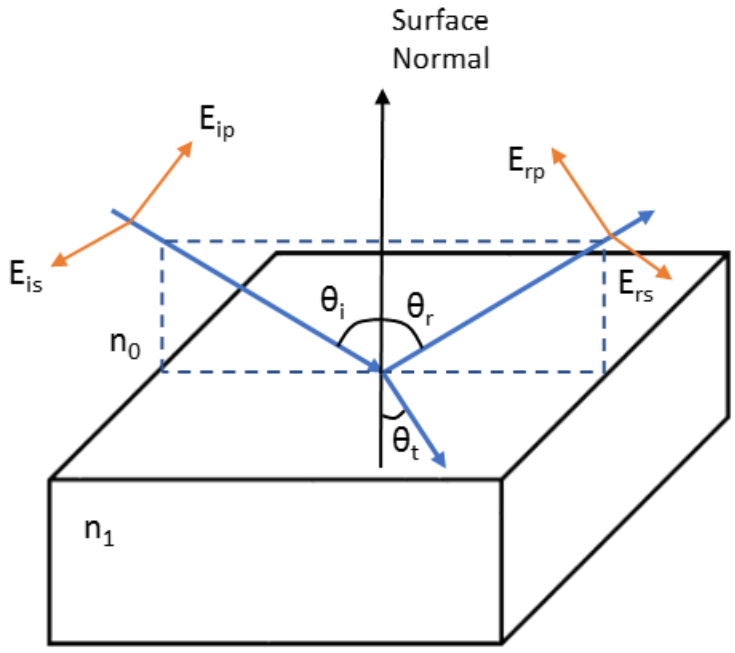

Figure 3.2 The general illustration of the MO Kerr Effect

E_p refers to the p −polarized light, while E_s refers to the s −polarized light. The Fresnel reflection equations are different for p −polarized and s −polarized electric fields. When

the medium is non-magnetic, the two reflection coefficients are independent of each other which are named as r_p and r_s. If the wave is reflected from a magnetic medium, the s −polarized and p −polarized reflection coefficients start to couple. Then, there would be two more terms which are called Kerr components [77] and shown as r_{ps} and r_{sp}. Therefore, the Fresnel reflection coefficient matrix can be illustrated as:

$$\Re = \begin{pmatrix} r_{pp} & r_{ps} \\ r_{sp} & r_{ss} \end{pmatrix} \tag{81}$$

while r_{ij} is the ratio of the reflected i −polarized electric field to the incident j −polarized electric field. The first derivations of the Fresnel reflection coefficients were done by Voigt in 1908. Robinson extended Voigt's analysis by changing the non-magnetic medium to a dielectric one instead of air [77]. Then, Hunt expanded Robinson's analysis for the case of arbitrary magnetization [74]. There are some studies for the Kerr effect with normal incidence [78]-[79]. However, there is not much study on MOKE for oblique incidence since the derivations of Fresnel reflection coefficients are somewhat complicated [80].

The reflection matrix elements for the case of P-MOKE -while the light is obliquely incident- can be seen as follows [76], [80]:

$$r_{pp} = \frac{n_1 \cos(\theta_i) - n_0 \cos(\theta_t)}{n_1 \cos(\theta_i) + n_0 \cos(\theta_t)} \tag{82}$$

$$r_{ss} = \frac{n_0 \cos(\theta_i) - n_1 \cos(\theta_t)}{n_0 \cos(\theta_i) + n_1 \cos(\theta_t)} \tag{83}$$

$$r_{sp} = r_{ps} = \frac{i n_0 n_1 \cos(\theta_i) \cos(\theta_t) \mathbb{Q}}{(n_1 \cos(\theta_i) + n_0 \cos(\theta_t))(n_0 \cos(\theta_i) + n_1 \cos(\theta_t)) \cos(\theta_t)} \tag{84}$$

$\mathbb{Q}$ refers to the off-diagonal element of the dielectric tensor which is defined above as $\mathbb{Q} = i\frac{\varepsilon_o}{\varepsilon_c}$. The reflection matrix elements for the L-MOKE are illustrated as [76], [80]:

$$r_{pp} = \frac{n_1 \cos(\theta_i) - n_0 \cos(\theta_t)}{n_1 \cos(\theta_i) + n_0 \cos(\theta_t)} \tag{85}$$

$$r_{ss} = \frac{n_0 \cos(\theta_i) - n_1 \cos(\theta_t)}{n_0 \cos(\theta_i) + n_1 \cos(\theta_t)} \tag{86}$$

$$r_{sp} = -r_{ps} = \frac{i n_0 n_1 \cos(\theta_i) \sin(\theta_t) \mathbb{Q}}{(n_1 \cos(\theta_i) + n_0 \cos(\theta_t))(n_0 \cos(\theta_i) + n_1 \cos(\theta_t)) \cos(\theta_t)} \tag{87}$$

The reflection matrix elements for the T-MOKE are different from the L- MOKE and the P-MOKE in that the *s*- and *p*-waves do not couple to each other. Therefore, the values of

the transverse Kerr parameters, r_{sp} and r_{ps} are equal to zero. The reflection matrix elements for the T-MOKE are shown as [76], [80]:

$$r_{pp} = \frac{n_1 \cos(\theta_i) - n_0 \cos(\theta_t)}{n_1 \cos(\theta_i) + n_0 \cos(\theta_t)} - \frac{i2n_0 n_1 \cos(\theta_i) \sin(\theta_t)\, \mathbb{Q}}{n_1 \cos(\theta_i) + n_0 \cos(\theta_t)} \tag{88}$$

$$r_{ss} = \frac{n_0 \cos(\theta_i) - n_1 \cos(\theta_t)}{n_0 \cos(\theta_i) + n_1 \cos(\theta_t)} \tag{89}$$

$$r_{sp} = r_{ps} = 0 \tag{90}$$

The general Kerr angle, θ_K and ellipticity, ε_K for the *s*- and *p*- waves for the longitudinal and the polar MOKE are given by [75], [81]-[82]:

$$\begin{aligned} \theta_{Ks} &= -Re\left[\frac{r_{ps}}{r_{ss}}\right] \\ \theta_{Kp} &= Re\left[\frac{r_{sp}}{r_{pp}}\right] \end{aligned} \tag{91}$$

$$\begin{aligned} \varepsilon_{Ks} &= \frac{Im\left[\frac{r_{ps}}{r_{ss}}\right]}{Re\left[\frac{r_{ps}}{r_{ss}}\right]} \\ \varepsilon_{Kp} &= \frac{Im\left[\frac{r_{sp}}{r_{pp}}\right]}{Re\left[\frac{r_{sp}}{r_{pp}}\right]} \end{aligned} \tag{92}$$

Since there are no Kerr parameters, ($r_{sp} = 0$ and $r_{ps} = 0$) for the transversal MOKE case, Kerr angle and ellipticity cannot be calculated with the formulas in Eq. (91) and (92). Ferguson *et al.* stated that the characterization of the T-MOKE can be done by finding the normalized total reflectivity difference for the opposite magnetic field directions [83]. Furthermore, the magneto-optic effect for the transversal effect can only be seen in the r_{pp} term, since there is no off-diagonal dependency for the r_{ss} term. Therefore, magnetization modulated reflectivity difference for the transversal effect, called δ, is shown as [69], [83]:

$$\delta = \frac{\left(\left|r_{pp}(M^{+})\right|^{2} - \left|r_{pp}(M^{-})\right|^{2}\right)}{{r_{pp}}^{2}} \tag{93}$$

while M^{+} stands for the magnetization along " $+$ " direction, and M^{-} stands for the magnetization along the " $-$ " direction. Since magnetization can only be seen for the *p*-polarized wave, r_{pp} has an off-diagonal $\mathbb{Q}$ dependency like longitudinal and polar MOKE cases.

CHAPTER 4

4 THEORY OF MAGNETO-OPTIC LAYER EMBEDDED OPTICAL WAVEGUIDE ISOLATORS

4.1 Introduction

Optical isolators are indispensable components in optical communications for protecting lasers from undesired back reflections [7]-[8]. Commercially available isolators are large and expensive devices, which prevents them from being integrated with InP-based and/or Silicon-on-Insulator-based optoelectronic devices. Therefore, as an alternative to them, there have been numerous studies conducted to fabricate an integrated optical isolator. Two main approaches are interferometric optical isolators with ferrimagnetic garnets as magneto-optic material [19]-[20], [24] and semiconductor active waveguide optical isolators (SOA-type) with common ferromagnetic elemental metals like Fe, Co, or Ni [12]-[14], [84]. A comprehensive literature review on these two studies will be presented in more detail in Chapter 5.

In Chapter 5, we propose and theoretically analyze SOA-type optical isolators operating at $1.55\ \mu m$ telecommunication wavelength. In this chapter, we present the theory behind the work in Chapter 5. The mathematical derivations of Maxwell Equations are

performed while magnetic bias is applied along the $\hat{y}$ −direction. The TE and TM mode solutions demonstrate that the TE mode does not depend on the magnetic bias, which translates into the fact that it has isotropic behavior along that magnetic field direction. In contrast to the TE mode, the TM mode shows anisotropic behavior, which is shown in the following sections of this chapter. There is a custom-designed NAG-Fortran based programming tool, which helps optimize the waveguide layer parameters, develops the solutions of the modes, provides the field profiles, and generates intensity plots. This tool helps us observe the loss profiles for forward and backward direction, which in turn aids in seeing the isolation ratio as well as the insertion losses.

4.2 Structure

The general structure of the proposed and theoretically analyzed SOA-type optical isolator is illustrated in Figure 4.1. In the design of each structure, there are two main sub-waveguides, which are monolithically integrated to each other to form one waveguide. One of them is a tunable multi-quantum well (MQW) InGaAsP/InP laser operating at $1.55\ \mu m$. The other one is the isolator region proposed as a combination of alternating layers of Silicon and one of the following magneto-optic materials at a time: Fe, Co, Ni and Ce:YIG.

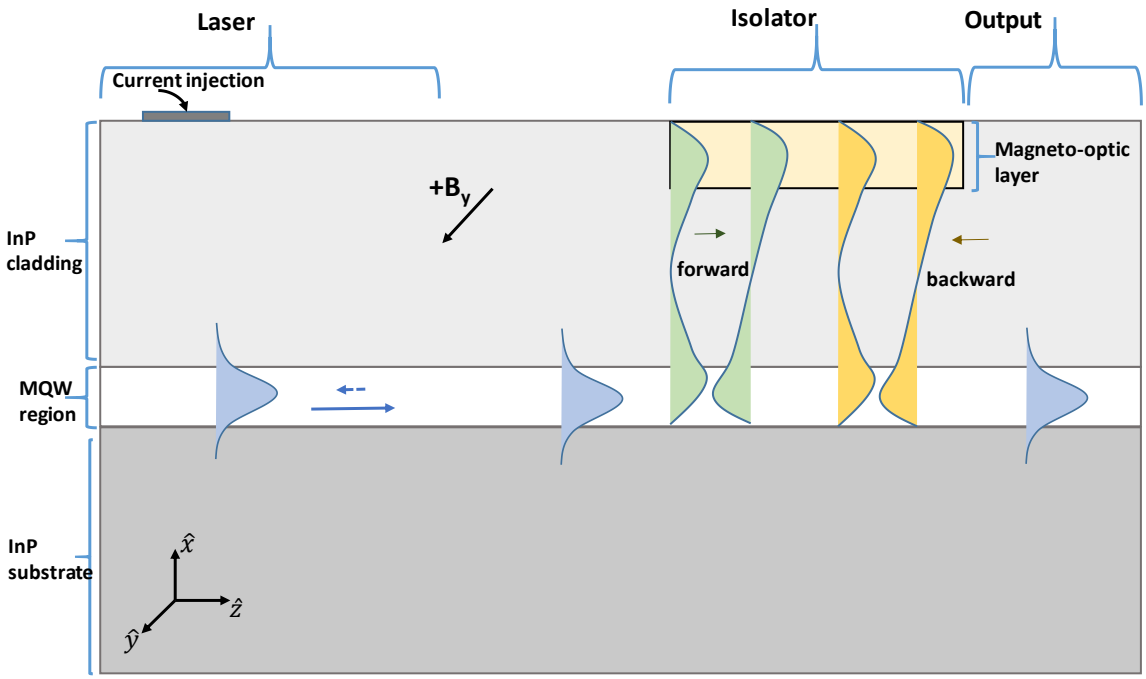

Figure 4.1 Two-dimensional structure of the proposed isolator

In this study, there is an applied magnetic field B_y through $\hat{y}$ −direction and its direction is then reversed to simulate forward and backward lights. As can be seen in Figure 4.1, after sending an injection current, the laser light forms on the left side of InGaAsP multi-quantum well (MQW) region. The laser light excites the two isolator modes when it reaches the isolator region and the power can be distributed in between MQW and isolator regions via coupling of the two layers. With proper optimization of layer parameters, we can confine backward light primarily in the lossy isolator section, which is the desired isolator behavior in the proposed device configuration. Moreover, by the help of the

aforementioned programming tool, it is possible to comparatively check the loss configurations along forward and backward directions upon the change of Si-layer thicknesses in the isolator region. Through the iterative alterations of various Si-layer thickness values, we select the one at which the amount of backward loss makes a peak. At that highest backward loss point, the intensity is confined mainly in the lossy magneto-optic region instead of the MQW layer. This is the main principle of the isolator approach proposed in this current work. Further detailed information about all layers is presented in Chapter 5.

Since the isolator region is located on the right side of the structure in Figure 4.1, we will now focus on the right isolator region as seen in Figure 4.2.

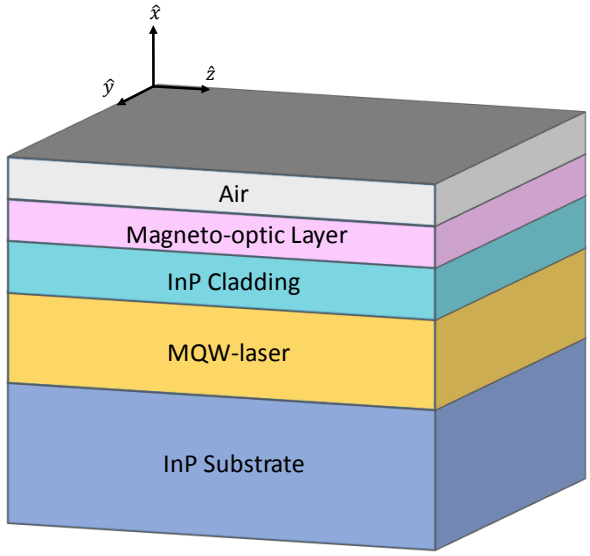

Figure 4.2 Magneto-optic region of the proposed device

The basic five-layer structure is shown in Figure 4.2. We choose the five-layer structure for mathematical simplicity. However, in our programming tool we have the flexibility to add as many layers as we can. First, we need to solve the Maxwell's equations while the static magnetic field is observed along the $\hat{y}$ −direction. Afterwards, the TM and TE mode solutions are analyzed separately.

4.3 Solutions of Maxwell Equations for the Static Magnetic field-B_y:

The system of Maxwell Equations is described as follows while the charge density and the current density is zero, i.e. $\rho = 0, J = 0$:

$$\nabla \times \vec{E} = -\frac{\partial \vec{B}}{\partial t} \tag{94}$$

$$\nabla \times \vec{H} = \frac{\partial \vec{D}}{\partial t} \tag{95}$$

$$\nabla . \vec{D} = 0 \tag{96}$$

$$\nabla . \vec{B} = 0 \tag{97}$$

$\vec{E}$ and $\vec{H}$ are electric and magnetic field intensities, while $\vec{D}$, and $\vec{B}$ refer to electric and magnetic flux densities, respectively. Before solving Maxwell equations, we need to define dielectric tensor ($\overleftrightarrow{\kappa}$) when the magnetic field is along the $\hat{y}$ −direction. As stated earlier in

Chapter 2, for anisotropic media, magnetic energy of the system changes according to the direction of magnetization [85]. Although isotropic materials have a permittivity constant, anisotropic ones have a permittivity tensor that includes their dependence on the propagation direction. The form of the dielectric tensor and its inverse for static magnetic field along the $\hat{y}$ −direction can be represented as follows:

$$\overleftrightarrow{\kappa} = \begin{bmatrix} \kappa_v & 0 & -\kappa_0 \\ 0 & \kappa_c & 0 \\ \kappa_0 & 0 & \kappa_v \end{bmatrix} \tag{98}$$

$$\overleftrightarrow{\kappa}^{-1} = \begin{bmatrix} \kappa_v/\Delta & 0 & -\kappa_0/\Delta \\ 0 & 1/\kappa_c & 0 \\ \kappa_0/\Delta & 0 & \kappa_v/\Delta \end{bmatrix} \tag{99}$$

"Δ" in the inverse dielectric tensor, $\overleftrightarrow{\kappa}^{-1}$, refers to $\Delta = {\kappa_0}^2 + {\kappa_v}^2$. The main difference of anisotropic materials compared to the isotropic ones is their off-diagonal elements "κ_0" in their dielectric tensors. Therefore, the off-diagonal data must be acquired to model the waveguide optical isolator behavior with a magneto-optic layer. Krinchik *et al.* [86]-[87] measured the off-diagonal data for Fe, Co, Ni ferromagnetic pure metals. While evaluating the complex off-diagonal data, Krinchik *et al.* evaluated the polar and equatorial Kerr effects in the 0.22 to 6 eV range. Based on that information, Maxwell equations can be solved while the static magnetic bias is along the $\hat{y}$ −direction. $\vec{D}$ and $\vec{B}$ in Eq. (96) and Eq. (97) are on the order of $e^{j\omega t}$. Assuming the fields are invariant along the $\hat{y}$ −direction, the Maxwell equations would take the form as follows:

$$\nabla \times \vec{H} = \begin{vmatrix} \hat{x} & \hat{y} & \hat{z} \\ \partial/\partial x & 0 & \partial/\partial z \\ H_x & H_y & H_z \end{vmatrix} = j\omega\varepsilon_0 \vec{\kappa}.\vec{E} \tag{100}$$

$$\nabla \times \vec{E} = \begin{vmatrix} \hat{x} & \hat{y} & \hat{z} \\ \partial/\partial x & 0 & \partial/\partial z \\ E_x & E_y & E_z \end{vmatrix} = -j\omega\mu_0 \vec{H}. \tag{101}$$

As shown in Eq. (101), the permeability, μ equals to μ_0 for optical frequencies [72]. After solving the determinants in Eq. (100) and Eq. (101), Maxwell equations would be as follows:

$$-\frac{\partial H_y}{\partial z} = j\omega\varepsilon_0(\kappa_v E_x - \kappa_0 E_z) \tag{102}$$

$$\frac{\partial H_x}{\partial z} - \frac{\partial H_z}{\partial x} = j\omega\varepsilon_0\kappa_c E_y \tag{103}$$

$$\frac{\partial H_y}{\partial x} = j\omega\varepsilon_0(\kappa_0 E_x + \kappa_v E_z) \tag{104}$$

$$-\frac{\partial E_y}{\partial z} = -j\omega\mu_0 H_x \tag{105}$$

$$\frac{\partial E_x}{\partial z} - \frac{\partial E_z}{\partial x} = -j\omega\mu_0 H_y \tag{106}$$

$$\frac{\partial E_y}{\partial x} = -j\omega\mu_0 H_z \tag{107}$$

As known, E_x, E_z, and H_y are TM-like fields and H_x, H_z, E_y are TE-like fields. Therefore, we need to solve Eq.'s (102), (104), (106) to get the TM mode solutions, and Eq.'s (103), (105), (107) to get the TE solutions. The brief derivation of the wave equations can be seen separately for the TM and the TE fields in the next two sections.

4.3.1 The Solutions for the TM Mode

Since Eq.'s (102), (104), and (106) are the equations for the TM-like fields, they are to be manipulated to get the final version of the TM wave equation. If Eq. (102) is multiplied by κ_v/κ_0, the equation would be as follows:

$$-\frac{\kappa_v}{\kappa_0}\frac{\partial H_y}{\partial z} = j\omega\varepsilon_0\left(\frac{{\kappa_v}^2}{\kappa_0}E_x - \kappa_v E_z\right) \tag{108}$$

When Eq. (108) and Eq. (104) are added, the new equation depends on two variables, E_x, and H_y. The new relation is

$$\frac{\partial H_y}{\partial x} - \frac{\kappa_v}{\kappa_0}\frac{\partial H_y}{\partial z} = j\omega\varepsilon_0\left(\frac{{\kappa_0}^2 + {\kappa_v}^2}{\kappa_0}\right)E_x. \tag{109}$$

The equation for E_x could be shown in terms of H_y as:

$$E_x = \frac{\kappa_0}{j\omega\varepsilon_0({\kappa_0}^2 + {\kappa_v}^2)}\left[\frac{\partial H_y}{\partial x} - \frac{\kappa_v}{\kappa_0}\frac{\partial H_y}{\partial z}\right] \tag{110}$$

The first derivative of E_x in terms of z is as follows:

$$\frac{\partial E_x}{\partial z} = \frac{\kappa_0}{j\omega\varepsilon_0({\kappa_0}^2 + {\kappa_v}^2)}\left[\frac{\partial^2 H_y}{\partial z \partial x} - \frac{\kappa_v}{\kappa_0}\frac{\partial^2 H_y}{\partial z^2}\right] \tag{111}$$

In addition to $\partial E_x/\partial z$, $\partial E_z/\partial x$ should also be known in order to obtain each term in Eq. (106). To get this, Eq. (102) should be multiplied by $-\kappa_0/\kappa_v$ this time as in Eq. (112):

$$\frac{\kappa_0}{\kappa_v}\frac{\partial H_y}{\partial z} = j\omega\varepsilon_0\left(-\kappa_0 E_x + \frac{{\kappa_0}^2}{\kappa_v}E_z\right) \tag{112}$$

Eq. (104) and Eq. (112) are added and the new equation would depend on E_z and H_y:

$$\frac{\kappa_0}{\kappa_v}\frac{\partial H_y}{\partial z} + \frac{\partial H_y}{\partial x} = j\omega\varepsilon_0\left(\frac{{\kappa_0}^2 + {\kappa_v}^2}{\kappa_v}\right)E_z \tag{113}$$

The equation for E_z in terms of H_y can be formulated as

$$E_z = \frac{\kappa_v}{j\omega\varepsilon_0({\kappa_0}^2 + {\kappa_v}^2)}\left[\frac{\kappa_0}{\kappa_v}\frac{\partial H_y}{\partial z} + \frac{\partial H_y}{\partial x}\right] \tag{114}$$

The first order derivative of E_z in terms of x is given as

$$\frac{\partial E_z}{\partial x} = \frac{\kappa_v}{j\omega\varepsilon_0({\kappa_0}^2 + {\kappa_v}^2)}\left[\frac{\kappa_0}{\kappa_v}\frac{\partial^2 H_y}{\partial x \partial z} + \frac{\partial^2 H_y}{\partial x^2}\right] \tag{115}$$

Since we now have $\partial E_x/\partial z$ and $\partial E_z/\partial x$ terms which are in Eq. (111) and Eq. (115), respectively; those can be plugged into Eq. (106) to have a simplified equation with only one variable, H_y:

$$\frac{\kappa_0}{j\omega\varepsilon_0({\kappa_0}^2+{\kappa_v}^2)}\left[\frac{\partial^2 H_y}{\partial z\partial x}-\frac{\kappa_v}{\kappa_0}\frac{\partial^2 H_y}{\partial z^2}\right]-\frac{\kappa_v}{j\omega\varepsilon_0({\kappa_0}^2+{\kappa_v}^2)}\left[\frac{\kappa_0}{\kappa_v}\frac{\partial^2 H_y}{\partial x\partial z}+\frac{\partial^2 H_y}{\partial x^2}\right] = -j\omega\mu_0 H_y \tag{116}$$

Further simplified version of Eq. (116) can be represented as in Eq. (117), which is the TM-like wave equation, while magnetic bias is along the $\hat{y}$ −direction:

$$\frac{\partial^2 H_y}{\partial z^2}+\frac{\partial^2 H_y}{\partial x^2}+\omega^2\mu_0\varepsilon_0\frac{({\kappa_0}^2+{\kappa_v}^2)}{\kappa_v}H_y=0 \tag{117}$$

When H_y is assigned to be *V* and the wave equation is simplified, it takes the form as

$$\frac{\partial^2 V}{\partial z^2}+\frac{\partial^2 V}{\partial x^2}+k^2\kappa_v\left(1+\left(\frac{\kappa_0}{\kappa_v}\right)^2\right)V=0 \tag{118}$$

$\kappa_v\left(1+\left(\frac{\kappa_0}{\kappa_v}\right)^2\right)$ could be defined as "κ_{el}" which is the effective dielectric constant for each layer "l". Since κ_0/κ_v can be assigned as ϱ, κ_{el} would take the form of $\kappa_v(1+\varrho^2)$. "k" refers to the wavenumber for free space. If the magnetic field as well as the off-diagonal element are equal to zero, κ_{el} would be equal to κ_{vl}. For propagating modes along the $+\hat{z}$ −direction, the transverse magnetic field component, H_y, could be defined as $V(x,z)=$

$v(x)\exp(-\gamma_h z)$ which also shows that the partial derivatives of V with respect to z would be $-\gamma_h$, i.e. the complex propagation constant. The new form of the wave equation, Eq. (118), for layer "l" can be illustrated as in Eq. (119):

$$\frac{\partial^2 v_l(x)}{\partial x^2} + {h_l}^2 v_l(x) = 0 \tag{119}$$

while the square of the transverse wavenumber is

$${h_l}^2 = k^2 \kappa_{el} + {\gamma_h}^2 \tag{120}$$

TM-mode solutions necessitate H_y and E_z continuities along the boundary regions. Eq. (119) gives the solutions for H_y. The solutions for E_z could be obtained by plugging H_y solutions into Eq. (114). The solutions of Eq. (119) for $5-$layer waveguide structure can be illustrated as

$$v_l(x) = \left\{ \begin{array}{ccc} \mathcal{S}_1 e^{-h_1(x-x_1)} & , & l = 1 \\ \mathcal{S}_l \cos h_l(x-x_l) + \mathcal{R}_l \dfrac{\kappa_{el}}{h_l} \sin h_l(x-x_l) & , & l = 2,3,4 \\ \mathcal{S}_5 e^{h_5(x-x_4)} & , & l = 5 \end{array} \right\} \tag{121}$$

The solution at the top of Eq. (121) where $l = 1$ is for the first layer, while the solution at the bottom is for the fifth layer. The squares of the transverse wavenumbers are

$$h_l{}^2 = \begin{Bmatrix} -(k^2\kappa_{el} + \gamma_h{}^2) & l = 1 \\ k^2\kappa_{el} + \gamma_h{}^2 & l = 2,3,4 \\ -(k^2\kappa_{el} + \gamma_h{}^2) & l = 5 \end{Bmatrix}. \tag{122}$$

To be able to generalize this approach, we assume all layers are anisotropic, which means each of them has a κ_0 dependency. Any layer can be transformed into isotropic one by simply placing $\kappa_0 = 0$. The continuity equation for H_y at the first boundary x_1 can be represented as in Eq. (123). If $d_2 = x_1 - x_2$ is assigned, Eq. (124) would be observed

$$v_1(x_1) = v_2(x_1) \tag{123}$$

$$\mathcal{S}_1 = \mathcal{S}_2 \cos h_2 d_2 + \mathcal{R}_2 \frac{\kappa_{e2}}{h_2} \sin h_2 d_2 \tag{124}$$

The continuity relation for E_z can be obtained by plugging the $H_y = v_l$ solutions into Eq. (114) which brings the results for the first boundary ($x = x_1$) as in Eq. (125):

$$-\gamma_h \frac{\varrho_1}{\kappa_{e1}} v_1 + \frac{1}{\kappa_{e1}} \frac{\partial v_1}{\partial x} = -\gamma_h \frac{\varrho_2}{\kappa_{e2}} v_2 + \frac{1}{\kappa_{e2}} \frac{\partial v_2}{\partial x} \tag{125}$$

Since $v_1(x_1) = v_2(x_1)$ holds true, Eq. (125) can be rewritten to follow Eq. (126)

$$\gamma_h \left(\frac{\varrho_2}{\kappa_{e2}} - \frac{\varrho_1}{\kappa_{e1}} \right) v_1 + \frac{1}{\kappa_{e1}} \frac{\partial v_1}{\partial x} = \frac{1}{\kappa_{e2}} \frac{\partial v_2}{\partial x} \tag{126}$$

In turn, Eq. (126) turns out to be

$$\left[\gamma_h\left(\frac{\varrho_2}{\kappa_{e2}}-\frac{\varrho_1}{\kappa_{e1}}\right)+\frac{1}{\kappa_{e1}}\frac{\partial}{\partial x}\right]v_1=\left(\frac{1}{\kappa_{e2}}\frac{\partial}{\partial x}\right)v_2 \tag{127}$$

The derivatives of v_1 and v_2 with respect to x at $x=x_1$ would follow

$$\frac{\partial v_1}{\partial x}|_{x=x_1}=-h_1 v_1|_{x=x_1} \quad \Longrightarrow \quad \frac{\partial v_1}{\partial x}|_{x=x_1}=-h_1\mathcal{S}_1 \tag{128}$$

$$\frac{\partial v_2}{\partial x}|_{x=x_1}=-h_2\mathcal{S}_2\sin h_2 d_2+\mathcal{R}_2\kappa_{e2}\cos h_2 d_2 \tag{129}$$

Eq. (128) and Eq. (129) are plugged into Eq. (127), and hence the simplified form is

$$\gamma_h\left(\frac{\varrho_2}{\kappa_{e2}}-\frac{\varrho_1}{\kappa_{e1}}\right)\mathcal{S}_1-\frac{h_1}{\kappa_{e1}}\mathcal{S}_1=\left(\frac{-h_2}{\kappa_{e2}}\mathcal{S}_2\sin h_2 d_2+\mathcal{R}_2\cos h_2 d_2\right) \tag{130}$$

At the $x=x_1$ boundary, there is just one coefficient $\mathcal{S}_1$ for the first layer. Therefore, $\mathcal{S}_1$ can only take place on the left side of the continuity relation in Eq. (37). At the $x=x_2$ boundary, H_y and E_z continuities are

$$\mathcal{S}_2=\mathcal{S}_3\cos h_3 d_3+\mathcal{R}_3\frac{\kappa_{e3}}{h_3}\sin h_3 d_3 \tag{131}$$

$$\gamma_h\left(\frac{\varrho_3}{\kappa_{e3}}-\frac{\varrho_2}{\kappa_{e2}}\right)\mathcal{S}_2+\mathcal{R}_2=\left(\frac{-h_3}{\kappa_{e3}}\mathcal{S}_3\sin h_3 d_3+\mathcal{R}_3\cos h_3 d_3\right). \tag{132}$$

For the boundary $x=x_3$, the continuity relations would follow the same pattern as Eq. (131) and Eq. (132), which can be formulated as

$$\mathcal{S}_3 = \mathcal{S}_4 \cos h_4 d_4 + \mathcal{R}_4 \frac{\kappa_{e4}}{h_4} \sin h_4 d_4 \tag{133}$$

$$\gamma_h \left(\frac{\varrho_4}{\kappa_{e4}} - \frac{\varrho_3}{\kappa_{e3}} \right) \mathcal{S}_3 + \mathcal{R}_3 = \left(\frac{-h_4}{\kappa_{e4}} \mathcal{S}_4 \sin h_4 d_4 + \mathcal{R}_4 \cos h_4 d_4 \right). \tag{134}$$

Since the pattern changes at the outer boundaries of $x = x_4$ and $x = x_1$, Eq. (136) would hold true, which is a slight deviation from Eq. (134)

$$\mathcal{S}_4 = \mathcal{S}_5 \tag{135}$$

$$\gamma_h \left(\frac{\varrho_5}{\kappa_{e5}} - \frac{\varrho_4}{\kappa_{e4}} \right) \mathcal{S}_4 + \mathcal{R}_4 = \frac{h_5}{\kappa_{e5}} \mathcal{S}_5 \tag{136}$$

We could generalize the continuity relations from Eq. (131) to Eq. (134) for inner boundaries of $x = x_2$ and $x = x_3$ by simply indexing the left-hand side as $(l-1)$ and the right-hand side as l:

$$0 = -\mathcal{S}_{l-1} + \mathcal{S}_l \cos h_l d_l + \mathcal{R}_l \frac{\kappa_{el}}{h_l} \sin h_l d_l \tag{137}$$

$$0 = \gamma_h \left(\frac{\varrho_{l-1}}{\kappa_{e(l-1)}} - \frac{\varrho_l}{\kappa_{el}} \right) \mathcal{S}_{l-1} - \mathcal{R}_{l-1} - \frac{h_l}{\kappa_{el}} \mathcal{S}_l \sin h_l d_l + \mathcal{R}_l \cos h_l d_l \tag{138}$$

Eq.'s (137-138) can be transformed into a transfer matrix by using the expressions in Eq. (121):

$$\begin{pmatrix} v_{l-1} \\ v_{l-1}{}' \end{pmatrix} = \begin{pmatrix} \cos h_l d_l & (\kappa_{el}/h_l)\sin h_l d_l \\ -(h_l/\kappa_{el})\sin h_l d_l & \cos h_l d_l \end{pmatrix} \begin{pmatrix} v_l \\ v_l{}' \end{pmatrix} \tag{139}$$

Since $\mathcal{R}_1$ does not exist for $x = x_1$, the transfer matrix equation for the first boundary is given in Eq. (140):

$$\begin{pmatrix} \mathcal{S}_1 \\ \left(\gamma_h\left(\frac{\varrho_2}{\kappa_{e2}} - \frac{\varrho_1}{\kappa_{e1}}\right) - \frac{h_1}{\kappa_{e1}}\right)\mathcal{S}_1 \end{pmatrix} = \begin{pmatrix} \cos h_2 d_2 & (\kappa_{e2}/h_2)\sin h_2 d_2 \\ -(h_2/\kappa_{e2})\sin h_2 d_2 & \cos h_2 d_2 \end{pmatrix} \begin{pmatrix} \mathcal{S}_2 \\ \mathcal{R}_2 \end{pmatrix} \tag{140}$$

For inner boundaries, the generalized transfer matrix equation can be represented by

$$\begin{pmatrix} \mathcal{S}_{l-1} \\ \gamma_h\left(\frac{\varrho_l}{\kappa_{el}} - \frac{\varrho_{l-1}}{\kappa_{e(l-1)}}\right)\mathcal{S}_{l-1} + \mathcal{R}_{l-1} \end{pmatrix} = \begin{pmatrix} \cos h_l d_l & (\kappa_{el}/h_l)\sin h_l d_l \\ -(h_l/\kappa_{el})\sin h_l d_l & \cos h_l d_l \end{pmatrix} \begin{pmatrix} \mathcal{S}_l \\ \mathcal{R}_l \end{pmatrix} \tag{141}$$

For the sake of presentation simplicity, the elements of transfer matrix can be defined as follows:

$$\mathcal{T}_l^{\,h} = \begin{pmatrix} \mathcal{A}_l{}^h & \mathcal{B}_l{}^h \\ \mathcal{C}_l{}^h & \mathcal{D}_l{}^h \end{pmatrix} \tag{142}$$

Also, due to the $\mathcal{S}_4 = \mathcal{S}_5$ equality, Eq. (136) could be written more simply as:

$$\left[\gamma_h\left(\frac{\varrho_5}{\kappa_{e5}} - \frac{\varrho_4}{\kappa_{e4}}\right) - \frac{h_5}{\kappa_{e5}}\right]\mathcal{S}_4 + \mathcal{R}_4 = 0 \tag{143}$$

After placing all relations coming from boundary conditions and simplifying the transfer matrix elements, the secular equation could be represented as a (7×7) matrix:

$$\begin{pmatrix} -1 & \mathcal{A}_2{}^h & \mathcal{B}_2{}^h & 0 & 0 & 0 & 0 \\ \left(\gamma_h\left(\frac{\varrho_1}{\kappa_{e1}}-\frac{\varrho_2}{\kappa_{e2}}\right)+\frac{h_1}{\kappa_{e1}}\right) & \mathcal{C}_2{}^h & \mathcal{D}_2{}^h & 0 & 0 & 0 & 0 \\ 0 & -1 & 0 & \mathcal{A}_3{}^h & \mathcal{B}_3{}^h & 0 & 0 \\ 0 & \gamma_h\left(\frac{\varrho_2}{\kappa_{e2}}-\frac{\varrho_3}{\kappa_{e3}}\right) & -1 & \mathcal{C}_3{}^h & \mathcal{D}_3{}^h & 0 & 0 \\ 0 & 0 & 0 & -1 & 0 & \mathcal{A}_4{}^h & \mathcal{B}_4{}^h \\ 0 & 0 & 0 & \gamma_h\left(\frac{\varrho_3}{\kappa_{e3}}-\frac{\varrho_4}{\kappa_{e4}}\right) & -1 & +\mathcal{C}_4{}^h & \mathcal{D}_4{}^h \\ 0 & 0 & 0 & 0 & 0 & \left(\gamma_h\left(\frac{\varrho_4}{\kappa_{e4}}-\frac{\varrho_5}{\kappa_{e5}}\right)+\frac{h_5}{\kappa_{e5}}\right) & -1 \end{pmatrix} \begin{pmatrix} \mathcal{S}_1 \\ \mathcal{S}_2 \\ \mathcal{R}_2 \\ \mathcal{S}_3 \\ \mathcal{R}_3 \\ \mathcal{S}_4 \\ \mathcal{R}_4 \end{pmatrix} \equiv A^h \boldsymbol{q} = 0 \quad (144)$$

According to the field continuity relation at x_4, $\mathcal{S}_5 = \mathcal{S}_4$, the secular matrix has one less dimension, which makes the computation easier and faster. The main diagonal of the matrix is highlighted in grey in matrix Eq. (144). In this secular equation, q should be a non-zero vector, which makes A^h a singular matrix and $det[A^h] = 0$ [as explained in Appendix 2]. The program computes the modes by determining the values of γ_h, which confirms the singularity of the A^h transfer matrix. Since there are many zeros above and below the main diagonal of the matrix, it could be easier to store matrix elements as a band matrix that has fewer numbers of elements compared to the original matrix. The band matrix with two super-diagonals $(k_u = 2)$ and two sub-diagonals $(k_l = 2)$ would be

$$A_b{}^h = \begin{pmatrix} 0 & 0 & \mathcal{B}_2{}^h & 0 & \mathcal{B}_3{}^h & 0 & \mathcal{B}_4{}^h \\ 0 & \mathcal{A}_2{}^h & \mathcal{D}_2{}^h & \mathcal{A}_3{}^h & \mathcal{D}_3{}^h & \mathcal{A}_4{}^h & \mathcal{D}_4{}^h \\ -1 & \mathcal{C}_2{}^h & 0 & \mathcal{C}_3{}^h & 0 & +\mathcal{C}_4{}^h & -1 \\ \left(\gamma_h\left(\frac{\varrho_1}{\kappa_{e1}}-\frac{\varrho_2}{\kappa_{e2}}\right)+\frac{h_1}{\mathcal{K}_{e1}}\right) & -1 & -1 & -1 & -1 & \left(\gamma_h\left(\frac{\varrho_4}{\kappa_{e4}}-\frac{\varrho_5}{\kappa_{e5}}\right)+\frac{h_5}{\mathcal{K}_{e5}}\right) & 0 \\ 0 & \gamma_h\left(\frac{\varrho_2}{\kappa_{e2}}-\frac{\varrho_3}{\kappa_{e3}}\right) & 0 & \gamma_h\left(\frac{\varrho_3}{\kappa_{e3}}-\frac{\varrho_4}{\kappa_{e4}}\right) & 0 & 0 & 0 \end{pmatrix} \quad (145)$$

The off-diagonal element ϱ is implicitly embedded in the transfer matrix elements. Since the transfer matrix is a function of h, and h is equal to $\sqrt{k^2\kappa_{el}+{\gamma_h}^2} = \sqrt{k^2\kappa_v(1+\varrho^2)+{\gamma_h}^2}$, the transfer matrix elements are even functions of ϱ. Therefore, changing the direction of magnetic bias does not affect the first three rows of the band matrix while it affects the last two rows since they are odd functions of ϱ. The row dimension of the band matrix is determined by the help of upper and lower diagonals; $k_u{+}k_l+1=5$. The column dimension is equal to the one in the original matrix, which makes the band matrix (5×7) as seen in Eq. (145). The size of the matrix for $5-$layer structure would be (7×7) and the general equation for the matrix dimension is as follows:

$$2n-3 \quad (146)$$

The band matrix dimension for $n-$layer structure should be $5\times(2n-3)$ for our set of TM-mode transfer matrices. The band matrix in Eq. (145) for the TM mode is defined for the $5-$layer structure. However, it would repeat the same pattern even if the number of

layers for the waveguide structure is increased. The representation of the band matrix for many layers can be given as

$$A_b{}^h = \begin{pmatrix} 0 & 0 & \mathcal{B}_2{}^h & 0 & \mathcal{B}_3{}^h & \dots & 0 & \mathcal{B}_{l-1}{}^h \\ 0 & \mathcal{A}_2{}^h & \mathcal{D}_2{}^h & \mathcal{A}_3{}^h & \mathcal{D}_3{}^h & \dots & \mathcal{A}_{l-1}{}^h & \mathcal{D}_{l-1}{}^h \\ -1 & \mathcal{C}_2{}^h & 0 & \mathcal{C}_3{}^h & 0 & \dots & \mathcal{C}_{l-1}{}^h & -1 \\ \left(\gamma_h\left(\frac{\varrho_1}{\kappa_{e1}}-\frac{\varrho_2}{\kappa_{e2}}\right)+\frac{h_1}{\mathcal{K}_{e1}}\right) & -1 & -1 & -1 & -1 & \dots & \left(\gamma_h\left(\frac{\varrho_{l-1}}{\kappa_{e(l-1)}}-\frac{\varrho_l}{\kappa_{el}}\right)+\frac{h_l}{\mathcal{K}_{el}}\right) & 0 \\ 0 & \gamma_h\left(\frac{\varrho_2}{\kappa_{e2}}-\frac{\varrho_3}{\kappa_{e3}}\right) & 0 & \gamma_h\left(\frac{\varrho_3}{\kappa_{e3}}-\frac{\varrho_4}{\kappa_{e4}}\right) & 0 & \dots & 0 & 0 \end{pmatrix} \quad (147)$$

As seen in Eq. (147), the number of rows are the same for l −layer structure, while the number of columns are $(2l-3)$. For 5 −layer waveguide structure, in order to establish an iterative Newton method, the derivative of matrix A^h with respect to γ_h is needed:

$$\frac{\partial A^h}{\partial \gamma_h} \equiv A^h{}_\gamma \quad (148)$$

$$= \begin{pmatrix} 0 & \mathcal{A}_{2\gamma}{}^h & \mathcal{B}_{2\gamma}{}^h & 0 & 0 & 0 & 0 \\ \left(\left(\frac{\varrho_1}{\kappa_{e1}}-\frac{\varrho_2}{\kappa_{e2}}\right)-\frac{\gamma_h}{h_1\kappa_{e1}}\right) & \mathcal{C}_{2\gamma}{}^h & \mathcal{D}_{2\gamma}{}^h & 0 & 0 & 0 & 0 \\ 0 & 0 & 0 & \mathcal{A}_{3\gamma}{}^h & \mathcal{B}_{3\gamma}{}^h & 0 & 0 \\ 0 & \left(\frac{\varrho_2}{\kappa_{e2}}-\frac{\varrho_3}{\kappa_{e3}}\right) & 0 & \mathcal{C}_{3\gamma}{}^h & \mathcal{D}_{3\gamma}{}^h & 0 & 0 \\ 0 & 0 & 0 & 0 & 0 & \mathcal{A}_{4\gamma}{}^h & \mathcal{B}_{4\gamma}{}^h \\ 0 & 0 & 0 & \left(\frac{\varrho_3}{\kappa_{e3}}-\frac{\varrho_4}{\kappa_{e4}}\right) & 0 & \mathcal{C}_{4\gamma}{}^h & \mathcal{D}_{4\gamma}{}^h \\ 0 & 0 & 0 & 0 & 0 & \left(\left(\frac{\varrho_4}{\kappa_{e4}}-\frac{\varrho_5}{\kappa_{e5}}\right)-\frac{\gamma_h}{h_5\kappa_{e5}}\right) & 0 \end{pmatrix}$$

The derivative of A^h with respect to γ_h in the band matrix scheme is illustrated as in Eq. (149):

$$\partial {A_b}^h \Big/ \partial \gamma_h \equiv {A_{b\gamma}}^h = \begin{pmatrix} 0 & 0 & {\mathcal{B}_{2\gamma}}^h & 0 & {\mathcal{B}_{3\gamma}}^h & 0 & {\mathcal{B}_{4\gamma}}^h \\ 0 & {\mathcal{A}_{2\gamma}}^h & {\mathcal{D}_{2\gamma}}^h & {\mathcal{A}_{3\gamma}}^h & {\mathcal{D}_{3\gamma}}^h & {\mathcal{A}_{4\gamma}}^h & {\mathcal{D}_{4\gamma}}^h \\ 0 & {\mathcal{C}_{2\gamma}}^h & 0 & {\mathcal{C}_{3\gamma}}^h & 0 & {\mathcal{C}_{4\gamma}}^h & 0 \\ \left(\left(\frac{\varrho_1}{\kappa_{e1}} - \frac{\varrho_2}{\kappa_{e2}}\right) - \frac{\gamma_h}{h_1 \mathcal{K}_{e1}}\right) & 0 & 0 & 0 & 0 & \left(\left(\frac{\varrho_4}{\kappa_{e4}} - \frac{\varrho_5}{\kappa_{e5}}\right) - \frac{\gamma_h}{h_5 \mathcal{K}_{e5}}\right) & 0 \\ 0 & \left(\frac{\varrho_2}{\kappa_{e2}} - \frac{\varrho_3}{\kappa_{e3}}\right) & 0 & \left(\frac{\varrho_3}{\kappa_{e3}} - \frac{\varrho_4}{\kappa_{e4}}\right) & 0 & 0 & 0 \end{pmatrix} \quad (149)$$

The derivatives of the transfer matrices with respect to γ_h for layer "l" while $l = 2, 3, 4$ would be as in Eq. (150):

$$ {\mathcal{T}_{l\gamma}}^h = \begin{pmatrix} {\mathcal{A}_{l\gamma}}^h & {\mathcal{B}_{l\gamma}}^h \\ {\mathcal{C}_{l\gamma}}^h & {\mathcal{D}_{l\gamma}}^h \end{pmatrix} \quad (150)$$

$$ = \frac{\gamma_h}{h} \begin{pmatrix} -d_l \sin h_l d_l & \mathcal{K}_{el}(h_l d_l \cos h_l d_l - \sin h_l d_l)/{h_l}^2 \\ -(\sin h_l d_l + h_l d_l \cos h_l d_l)/\mathcal{K}_{el} & -d_l \sin h_l d_l \end{pmatrix}$$

4.3.2 TE Modes

The derivation for the TE-like wave equation is simpler than that of the TM-like. If the first derivatives of Eq. (105) with respect to z are taken, and Eq. (107) with respect to x, the required terms of Eq. (103) would be acquired. Then, Eq. (103) can be rewritten in terms of the same variable E_y for this case as in Eq. (151) and Eq. (152):

$$-\frac{\partial^2 E_y}{\partial z^2} = -j\omega\mu_0 \frac{\partial H_x}{\partial z} \tag{151}$$

$$-\frac{\partial^2 E_y}{\partial x^2} = -j\omega\mu_0 \frac{\partial H_z}{\partial x} \tag{152}$$

The first order derivative equations for H_x and H_z would be as

$$\frac{\partial H_x}{\partial z} = \frac{1}{j\omega\mu_0}\frac{\partial^2 E_y}{\partial z^2} \tag{153}$$

$$\frac{\partial H_z}{\partial x} = -\frac{1}{j\omega\mu_0}\frac{\partial^2 E_y}{\partial x^2} \tag{154}$$

After Eq. (153) and Eq. (154) are placed into Eq. (103), the TE-like wave equation would follow as in Eq. (155) and the simplified form would be as in Eq. (156):

$$\frac{1}{j\omega\mu_0}\frac{\partial^2 E_y}{\partial z^2} + \frac{1}{j\omega\mu_0}\frac{\partial^2 E_y}{\partial x^2} = j\omega\varepsilon_0\kappa_c E_y \tag{155}$$

$$\frac{\partial^2 E_y}{\partial z^2} + \frac{\partial^2 E_y}{\partial x^2} + \omega^2 \mu_0 \varepsilon_0 \kappa_c E_y = 0 \tag{156}$$

As can be noticed in Eq. (156), there is no κ_0 dependence in the TE-like wave equation, which means that the system is isotropic, and the external magnetic field has no influence on it. Therefore, for planar waveguides, the TE-like wave equations do not present isolator behavior in contrast to the TM-like ones while the static magnetic field is along the $\hat{y}$ −direction. The wave equation for the TE modes could be written as in Eq. (157) after some mathematical manipulations

$$\frac{\partial^2 U(x,z)}{\partial z^2} + \frac{\partial^2 U(x,z)}{\partial x^2} + k^2 \kappa_c U(x,z) = 0 \tag{157}$$

while $k^2 = \omega^2 \mu_0 \varepsilon_0$ in free space, and $U(x,z) = E_y(x,z)$. Since x and z dependencies of $U(x,z)$ can be represented as $U(x,z) = u(x)\exp(-\gamma_e z)$, it can be stated that $\frac{\partial U}{\partial z} = -\gamma_e$, while γ_e is the complex propagation constant. The wave equation could be further simplified as follows:

$$\frac{\partial^2 u_l}{\partial x^2} + (k^2 \kappa_{cl} + {\gamma_e}^2) u_l = 0 \qquad l = 1,2,\dots,5 \tag{158}$$

where "l" refers to the layer number for the waveguide structure. E_y and H_z need to be continuous across the boundaries of each layer. According to Eq. (14), which is $\frac{\partial E_y}{\partial x} = -j\omega\mu_0 H_z$, H_z is on the order of $\partial E_y/\partial x$. Therefore, u_l and $\partial u_l/\partial x$ should also be

continuous across the boundaries. The solutions for E_y could be written as in Eq. (159) for the 5 −layer waveguide structure:

$$u_l = \begin{Bmatrix} \mathcal{Q}_1 e^{-h_1(x-x_1)} & l=1 \\ \mathcal{Q}_l \cos h_l(x-x_l) + (\mathcal{P}_l/h_l)\sin h_l(x-x_l) & l=2,3,4 \\ \mathcal{Q}_5 e^{-h_5(x-x_4)} & l=5 \end{Bmatrix} \tag{159}$$

The squares of the transverse wavenumbers should satisfy Eq. (160)

$${h_l}^2 = \begin{Bmatrix} -(k^2\kappa_{cl} + {\gamma_e}^2) \ , & l=1 \\ k^2\kappa_{cl} + {\gamma_e}^2 \ , & l=2,3,4 \\ -(k^2\kappa_{cl} + {\gamma_e}^2) \ , & l=5 \end{Bmatrix} \tag{160}$$

Thereafter, the continuity relations for E_y and its first order derivative with respect to x must be provided. The E_y field and its derivative is to be transferred to the next layer by using the transfer matrices as in Eq. (161):

$$\begin{pmatrix} u_{l-1} \\ {u_{l-1}}' \end{pmatrix} = \begin{pmatrix} \cos h_l d_l & (1/h_l)\sin h_l d_l \\ -h_l \sin h_l d_l & \cos h_l d_l \end{pmatrix} \begin{pmatrix} u_l \\ {u_l}' \end{pmatrix} \tag{161}$$

The transfer matrix could also be written as in Eq. (162):

$$\mathcal{T}_l^{\,e} = \begin{pmatrix} {\mathcal{A}_l}^e & {\mathcal{B}_l}^e \\ {\mathcal{C}_l}^e & {\mathcal{D}_l}^e \end{pmatrix} \tag{162}$$

Since $\mathcal{P}_1$ coefficient does not exist for the first layer, the first transfer matrix would be as in Eq. (163) while $l = 2$

$$\begin{pmatrix} \mathcal{Q}_1 \\ -h_1\mathcal{Q}_1 \end{pmatrix} = \begin{pmatrix} \cos h_2 d_2 & (1/h_2)\sin h_2 d_2 \\ -h_2 \sin h_2 d_2 & \cos h_2 d_2 \end{pmatrix} \begin{pmatrix} \mathcal{Q}_2 \\ \mathcal{P}_2 \end{pmatrix} \tag{163}$$

The transfer matrix in Eq. (164) confirms the relation in Eq. (161) for the elements $l = 3, 4, 5$:

$$\begin{pmatrix} \mathcal{Q}_{l-1} \\ \mathcal{P}_{l-1} \end{pmatrix} = \begin{pmatrix} \cos h_l d_l & (1/h_l)\sin h_l d_l \\ -h_l \sin h_l d_l & \cos h_l d_l \end{pmatrix} \begin{pmatrix} \mathcal{Q}_l \\ \mathcal{P}_l \end{pmatrix} \tag{164}$$

After adjusting all fields and derivatives, the secular equation as a (7×7) matrix can be seen as

$$\begin{pmatrix} -1 & \mathcal{A}_2{}^e & \mathcal{B}_2{}^e & 0 & 0 & 0 & 0 \\ h_1 & \mathcal{C}_2{}^e & \mathcal{D}_2{}^e & 0 & 0 & 0 & 0 \\ 0 & -1 & 0 & \mathcal{A}_3{}^e & \mathcal{B}_3{}^e & 0 & 0 \\ 0 & 0 & -1 & \mathcal{C}_3{}^e & \mathcal{D}_3{}^e & 0 & 0 \\ 0 & 0 & 0 & -1 & 0 & \mathcal{A}_4{}^e & \mathcal{B}_4{}^e \\ 0 & 0 & 0 & 0 & -1 & \mathcal{C}_4{}^e & \mathcal{D}_4{}^e \\ 0 & 0 & 0 & 0 & 0 & h_5 & -1 \end{pmatrix} \begin{pmatrix} \mathcal{Q}_1 \\ \mathcal{Q}_2 \\ \mathcal{P}_2 \\ \mathcal{Q}_3 \\ \mathcal{P}_3 \\ \mathcal{Q}_4 \\ \mathcal{P}_4 \end{pmatrix} \equiv A^e \boldsymbol{q} = 0 \tag{165}$$

Since $\mathcal{Q}_5 = \mathcal{Q}_4$ holds true, the numbers of coefficients in the secular matrix is diminished by one dimension. For the sake of computational simplicity, we make use of the band matrix instead of the regular matrix. The elements of the matrix are placed along the diagonals, and there are two super-diagonals ($k_u = 2$) and one sub-diagonal ($k_l = 1$) for the TE-mode band matrix:

$$A_b{}^e = \begin{pmatrix} 0 & 0 & \mathcal{B}_2{}^e & 0 & \mathcal{B}_3{}^e & 0 & \mathcal{B}_4{}^e \\ 0 & \mathcal{A}_2{}^e & \mathcal{D}_2{}^e & \mathcal{A}_3{}^e & \mathcal{D}_3{}^e & \mathcal{A}_4{}^e & \mathcal{D}_4{}^e \\ -1 & \mathcal{C}_2{}^e & 0 & \mathcal{C}_3{}^e & 0 & \mathcal{C}_4{}^e & -1 \\ h_1 & -1 & -1 & -1 & -1 & h_5 & 0 \end{pmatrix} \tag{166}$$

By using the formula $k_u + k_l + 1 = 4$, the row and column dimensions could be found which is a (4×7) matrix as can be seen in Eq. (166). The formula for the dimension of singular matrix, A^e, (in Eq. (165)) is $(2n-3) \times (2n-3)$, which is the same as the one in the TM-mode section (in Eq. (146)). Furthermore, the size of the TE band matrix, $A_b{}^e$, would be $4 \times (2n-3)$, regardless of the number of layers in the waveguide, while the size of the TM band matrix is $5 \times (2n-3)$.

In order to have an iterative Newton method, the derivative of the band matrix $A_b{}^e$ with respect to γ_e should be calculated via Eq. (167)

$$\partial A_b{}^e \Big/ \partial \gamma_e \equiv A_{b\gamma}{}^e = \begin{pmatrix} 0 & 0 & \mathcal{B}_{2\gamma}{}^e & 0 & \mathcal{B}_{3\gamma}{}^e & 0 & \mathcal{B}_{4\gamma}{}^e \\ 0 & \mathcal{A}_{2\gamma}{}^e & \mathcal{D}_{2\gamma}{}^e & \mathcal{A}_{3\gamma}{}^e & \mathcal{D}_{3\gamma}{}^e & \mathcal{A}_{4\gamma}{}^e & \mathcal{D}_{4\gamma}{}^e \\ 0 & \mathcal{C}_{2\gamma}{}^e & 0 & \mathcal{C}_{3\gamma}{}^e & 0 & \mathcal{C}_{4\gamma}{}^e & 0 \\ -\gamma_e/h_1 & 0 & 0 & 0 & 0 & -\gamma_e/h_5 & 0 \end{pmatrix} \tag{167}$$

Additionally, the derivative of $\mathcal{T}_l^e$ –the transfer matrix– with respect to γ_e can be seen in Eq. (168):

$$\mathcal{T}_{l\gamma}{}^{e} = \begin{pmatrix} \mathcal{A}_{l\gamma}{}^{e} & \mathcal{B}_{l\gamma}{}^{e} \\ \mathcal{C}_{l\gamma}{}^{e} & \mathcal{D}_{l\gamma}{}^{e} \end{pmatrix}$$
$$= \frac{\gamma_e}{h} \begin{pmatrix} -d_l \sin h_l d_l & \dfrac{(h_l d_l \cos h_l d_l - \sin h_l d_l)}{h_l{}^2} \\ -(\sin h_l d_l + h_l d_l \cos h_l d_l) & -d_l \sin h_l d_l \end{pmatrix} \tag{168}$$

4.4 Perturbation Matrices

As explained later in further detail in Chapter 5, the off-diagonal element κ_0 is generally smaller than κ_v and κ_c, all of which hold the relationship in Eq. (169):

$$\kappa_v \cong \kappa_c \gg \kappa_0 \tag{169}$$

Since the amount of perturbation in the system, ϱ, is defined as κ_0/κ_v, and κ_0 is very small, the secular equation in terms of ϱ can be polynomially expanded as in Eq. (170)

$$(A_0 + A_1\varrho + A_2\varrho^2 + \cdots)(\mathbf{q_0} + \mathbf{q_1}\varrho + \mathbf{q_2}\varrho^2 + \cdots) = 0 \tag{170}$$

while $A_0\mathbf{q_0} = 0$ represents the secular equation, when there is no magnetic bias that produces ϱ. Therefore, all equations are calculated at the point where $\varrho = 0$. According to Eq. (265) in Appendix 3, $\left(\frac{dA}{d\varrho}\right)_{\varrho=0}$ as well as $\left(\frac{dA}{d\gamma}\right)_{\varrho=0}$ should be computed in order to find the effect of magnetic bias over the propagation constant which can be seen as

$$\left(\frac{\partial\gamma}{\partial\varrho}\right)_{\varrho=0} = -\frac{(q_0{}^L)^\dagger \left(\frac{dA}{d\varrho}\right)_{\varrho=0} q_0}{(q_0{}^L)^\dagger \left(\frac{dA}{d\gamma}\right)_{\varrho=0} q_0} \tag{171}$$

Since matrix $A_b{}^e$ in Eq. (166) does not depend on the off-diagonal element, the differential in the numerator would be zero for the TE mode. Once the numerator is zero, it can be stated that the propagation constant γ does not have any relationship with the magnetic bias in terms of the TE mode. However, for the TM mode, $\left(\frac{dA_b}{d\gamma}\right)_{\varrho=0}$ can be illustrated as

$$\partial A_b{}^h \Big/ \partial\gamma_h \equiv A_{b\gamma}{}^h = \begin{pmatrix} 0 & 0 & \mathcal{B}_{2\gamma}{}^h & 0 & \mathcal{B}_{3\gamma}{}^h & 0 & \mathcal{B}_{4\gamma}{}^h \\ 0 & \mathcal{A}_{2\gamma}{}^h & \mathcal{D}_{2\gamma}{}^h & \mathcal{A}_{3\gamma}{}^h & \mathcal{D}_{3\gamma}{}^h & \mathcal{A}_{4\gamma}{}^h & \mathcal{D}_{4\gamma}{}^h \\ 0 & \mathcal{C}_{2\gamma}{}^h & 0 & \mathcal{C}_{3\gamma}{}^h & 0 & \mathcal{C}_{4\gamma}{}^h & 0 \\ \left(\left(\frac{\varrho_1}{\kappa_{e1}} - \frac{\varrho_2}{\kappa_{e2}}\right) - \frac{\gamma_h}{h_1\mathcal{K}_{e1}}\right) & 0 & 0 & 0 & 0 & \left(\left(\frac{\varrho_4}{\kappa_{e4}} - \frac{\varrho_5}{\kappa_{e5}}\right) - \frac{\gamma_h}{h_5\mathcal{K}_{e5}}\right) & 0 \\ 0 & \left(\frac{\varrho_2}{\kappa_{e2}} - \frac{\varrho_3}{\kappa_{e3}}\right) & 0 & \left(\frac{\varrho_3}{\kappa_{e3}} - \frac{\varrho_4}{\kappa_{e4}}\right) & 0 & 0 & 0 \end{pmatrix} \tag{172}$$

For the $\left(\frac{dA_b}{d\varrho}\right)_{\varrho=0}$, all of the $\mathcal{A}, \mathcal{B}, \mathcal{C}, \mathcal{D}$ terms in the transfer matrices have explicit ϱ dependence which assigns a value of zero to them while $\varrho = 0$. The magnetic bias dependency of the band matrix for the TM mode can be shown as

$$\left(\frac{\partial {A_b}^h}{\partial \varrho}\right)_{\varrho=0} \equiv {A_{b\varrho}}^h =$$

$$\begin{pmatrix} 0 & 0 & 0 & 0 & 0 & 0 & 0 \\ 0 & 0 & 0 & 0 & 0 & 0 & 0 \\ 0 & 0 & 0 & 0 & 0 & 0 & 0 \\ \left(\gamma_h\left(\frac{1}{\kappa_{e1}}-\frac{1}{\kappa_{e2}}\right)\right) & 0 & 0 & 0 & 0 & \left(\gamma_h\left(\frac{1}{\kappa_{e4}}-\frac{1}{\kappa_{e5}}\right)\right) & 0 \\ 0 & \left(\gamma_h\left(\frac{1}{\kappa_{e2}}-\frac{1}{\kappa_{e3}}\right)\right) & 0 & \left(\gamma_h\left(\frac{1}{\kappa_{e3}}-\frac{1}{\kappa_{e4}}\right)\right) & 0 & 0 & 0 \end{pmatrix} \quad (173)$$

As later explained in Chapter 5, we want to minimize the reflected power along the backward direction while maximizing the output power in the forward direction. Therefore, the waves through backward direction need to provide destructive interference while the waves through forward need to contribute to constructive interference, which could be demonstrated as in Eq. (174) and Eq. (175):

$$(\beta_{e-} - \beta_{o-})L = (2m \pm 1)\pi \quad (174)$$

$$(\beta_{e+} - \beta_{o+})L = 2m\pi \quad (175)$$

βs with subscript "e" represent the propagation constant for the even mode, while βs with "o" represent that of the odd mode. "L" is the length of the device, and "m" is the number of interference fringes. Additionally, the subscript " $-$ " is for the backward wave and the subscript " $+$ " is for the forward wave. To be able to obtain the relationship between the propagation constant for even and odd modes, these two equations should be solved

simultaneously. The derivative of complex propagation constant "γ_h" with respect to ϱ can be identified as in Eq. (176):

$$\left(\frac{\partial \gamma_h}{\partial \varrho}\right)_{\varrho=0} = \left(\frac{\partial \alpha_h}{\partial \varrho}\right)_{\varrho=0} + j\left(\frac{\partial \beta_h}{\partial \varrho}\right)_{\varrho=0} \tag{176}$$

When we expand the complex propagation constant to the first order using ϱ as a perturbation term, the relations for even and odd modes of forward-backward directions would be as follows:

$$\begin{aligned} {\gamma_{ho}}^{+}(\varrho) &= \gamma_{ho} + \gamma_{ho\varrho}\varrho, \quad {\gamma_{ho}}^{-}(\varrho) = \gamma_{ho} - \gamma_{ho\varrho}\varrho \\ {\gamma_{he}}^{+}(\varrho) &= \gamma_{he} + \gamma_{he\varrho}\varrho, \quad {\gamma_{he}}^{-}(\varrho) = \gamma_{he} - \gamma_{he\varrho}\varrho \end{aligned} \tag{177}$$

where $\gamma_{ho\varrho}$ refers to $\partial\gamma_{ho}/\partial\varrho$, and $\gamma_{he\varrho}$ refers to $\partial\gamma_{he}/\partial\varrho$. Off-diagonal element ϱ is also a complex number, which can be identified as $\varrho' + j\varrho''$. Considering all these relations above, Eq.'s (174) and (175) should be solved together, and the resulting equation for the number of interference fringes "m" would be as in Eq. (178):

$$\begin{aligned} 4m\left[\varrho''\left(\frac{\partial \alpha_e}{\partial \varrho} - \frac{\partial \alpha_o}{\partial \varrho}\right) + \varrho'\left(\frac{\partial \beta_e}{\partial \varrho} - \frac{\partial \beta_o}{\partial \varrho}\right)\right] \pm \varrho''\left(\frac{\partial \alpha_e}{\partial \varrho} - \frac{\partial \alpha_o}{\partial \varrho}\right) \pm \varrho'\left(\frac{\partial \beta_e}{\partial \varrho} - \frac{\partial \beta_o}{\partial \varrho}\right) \\ = \mp(\beta_e - \beta_o). \end{aligned} \tag{178}$$

4.5 TM Mode Orthogonality

For dielectric slab waveguides, all transverse modes in either the TE or TM field are orthogonal to each other. For example, for the TM mode, there are two transverse fields: one is E_x and the other one is H_y, while longitudinal field is E_z. Two transverse fields E_x and H_y of the two different modes are orthogonal to each other and the orthogonality equation, while the system is $\hat{y}$ −invariant, is

$$\int_{-\infty}^{+\infty} dx\, E_{x\nu} \times H^*{}_{y\mu} = 0 \quad while\ \mu \neq \nu \tag{179}$$

where

$$H_y = \nu(x) \exp(-\gamma z) \tag{180}$$

Considering $\kappa_0 \ll {\kappa_0}^2 + {\kappa_\nu}^2$, E_x is simplified as follows

$$E_x = -\frac{\kappa_\nu}{j\omega\varepsilon_0({\kappa_0}^2 + {\kappa_\nu}^2)} \frac{\partial H_y}{\partial z}. \tag{181}$$

Since κ_0 takes either zero or a constant value for each magneto-optic material that is being used in the waveguide layer, it can be accepted as a step function along the x-axis.

$({\kappa_0}^2 + {\kappa_\nu}^2)/\kappa_\nu$ is mostly defined as κ_{el} in this chapter, but we can call it as $\kappa_{el}(x)$ since it changes along the $\hat{x}$ −direction. The transverse electric field would change to Eq. (182):

$$E_{x\mu} \sim + \gamma_\mu \frac{\nu_\mu(x)}{\kappa_{el}(x)} \tag{182}$$

For our structure, which supports two modes along the forward direction, the orthogonality equation would be as follows:

$$(\nu_1, \nu_2) \approx \int_{-\infty}^{+\infty} dx \frac{\nu_1(x)}{\kappa_{el}(x)} \nu_2(x)^* = 0 \tag{183}$$

Since $\kappa_{el}(x)$ does not have explicit $\hat{x}$ −dependency, the derivative of $\kappa_{el}(x)$ with respect to x would be zero. Therefore, the first term of the wave equation in Eq. (118), can be multiplied by $\kappa_{el}(x)/\kappa_{el}(x)$ as in Eq. (184):

$$\kappa_{el}(x) \frac{d}{dx}\left(\frac{1}{\kappa_{el}(x)} \frac{d\nu_\mu}{dx}\right) + k^2 \kappa_{el}(x) \nu_\mu + {\gamma_\mu}^2 \nu_\mu = 0 \tag{184}$$

If Eq. (184) is multiplied by ${\nu_\nu}^*$ from the left side of the equation, the result would be as follows:

$${\nu_\nu}^* \frac{d}{dx}\left(\frac{1}{\kappa_{el}(x)} \frac{d\nu_\mu}{dx}\right) + k^2 {\nu_\nu}^* \nu_\mu + {\gamma_\mu}^2 {\nu_\nu}^* \frac{1}{\kappa_{el}(x)} \nu_\mu = 0 \tag{185}$$

Eq. (185) can be applied interchangeably to first and second modes, which would give the results as in Eq.'s (186) and (187):

$$\nu_2{}^* \frac{d}{dx}\left(\frac{1}{\kappa_{el}(x)}\frac{d\nu_1}{dx}\right) + k^2\nu_2{}^*\nu_1 + \gamma_1{}^2\nu_2{}^* \frac{1}{\kappa_{el}(x)}\nu_1 = 0 \tag{186}$$

$$\nu_1 \frac{d}{dx}\left(\frac{1}{\kappa_{el}(x)}\frac{d\nu_2{}^*}{dx}\right) + k^2\nu_1\nu_2{}^* + \gamma_2^{*2}\nu_1 \frac{1}{\kappa_{el}(x)}\nu_2{}^* = 0 \tag{187}$$

After subtracting Eq. (187) from Eq. (186) and integrating over the region of $-L < x < L$, Eq. (188) would be obtained:

$$\left(\gamma_1{}^2 - \gamma_2^{*2}\right)(\nu_1, \nu_2)\Big|_{-L}^{+L} + \int_{-L}^{+L}\left[\nu_2{}^* \frac{d}{dx}\left(\frac{1}{\kappa_{el}}\frac{d\nu_1}{dx}\right) - \nu_1 \frac{d}{dx}\left(\frac{1}{\kappa_{el}}\frac{d\nu_2{}^*}{dx}\right)\right] dx = 0 \tag{188}$$

The first term is the orthogonality relation, which is shown to be zero in Eq. (183) whereas the second and the third integrands can be solved via the help of integration by parts. The result of the second integrand is

$$I_1 = \nu_2{}^* \frac{1}{\kappa_{el}}\frac{d\nu_1}{dx}\Big|_{-L}^{+L} - \int_{-L}^{+L} \frac{1}{\kappa_{el}}\frac{d\nu_1}{dx}\frac{d\nu_2{}^*}{dx} dx \tag{189}$$

while the third integrand is

$$I_2 = v_1 \frac{1}{\kappa_{el}} \frac{dv_2{}^*}{dx}\Big|_{-L}^{+L} - \int_{-L}^{+L} \frac{1}{\kappa_{el}} \frac{dv_2{}^*}{dx} \frac{dv_1}{dx} dx \tag{190}$$

The second terms in Eq. (189) and Eq. (190) are cancelled while the first terms go to zero for the values of $L \rightarrow \infty$. Since all terms are vanished, and $\gamma_1 - \gamma_2$ are different from each other, the relation for orthogonality is proven as in Eq. (191):

$$(v_1, v_2) = 0 \tag{191}$$

This validates the orthogonality of the transverse electric field and transverse magnetic fields of the two different TM modes in our slab waveguide structure.

4.6 Laser-Isolator Boundary Conditions

As shown in Figure 4.1 in the previous sections of this chapter, there are three regions in the structure along the z propagation direction. One is the input laser region, the second one is the isolator region, and the third one is the laser-like output region, which are simply redrawn in Figure 4.3:

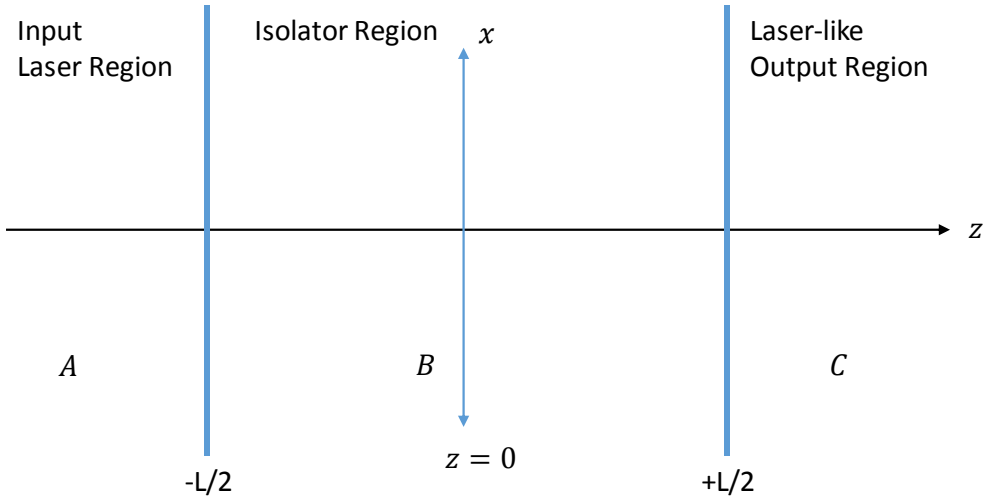

Figure 4.3 Simple representation of the proposed device

Regions A and C are laser-like waveguides, while region B is designed as an isolator. The laser-like regions support only one bound mode, while the isolator region supports two bound modes since it has two sub-waveguides in its geometry. TM modes propagating along the positive $\hat{z}$ −direction are named as $V_{r1}(x,z)$ and $V_{r2}(x,z)$, whereas the ones propagating along the negative $\hat{z}$ −direction are called as $V_{s1}(x,z)$ and $V_{s2}(x,z)$. The boundary conditions for all interfaces need to be administered by verifying the equalities of H_y and E_x fields. After the simplification of $E(x,z)$ in Eq. (182), the electromagnetic fields in region A can be shown as:

$$H_A(x,z) = v_A(x)\left(e^{-\gamma_A\left(z+\frac{L}{2}\right)} + R_{AB}e^{\gamma_A\left(z+\frac{L}{2}\right)}\right) \tag{192}$$

$$E_A(x,z) \cong \gamma_A \frac{\nu_A(x)}{\kappa_A(x)} \left(e^{-\gamma_A\left(z+\frac{L}{2}\right)} - R_{AB} e^{\gamma_A\left(z+\frac{L}{2}\right)} \right) \tag{193}$$

R_{AB} is the reflection coefficient along the $z = -L/2$ boundary. The TM transverse fields in region C can be represented as in Eq. (194) and Eq. (195):

$$H_C(x,z) = T_{BC} \nu_A(x) e^{-\gamma_A\left(z-\frac{L}{2}\right)} \tag{194}$$

$$E_C(x,z) \cong T_{BC} \gamma_A \frac{\nu_A(x)}{\kappa_A(x)} e^{-\gamma_A\left(z-\frac{L}{2}\right)} \tag{195}$$

while T_{BC} is the transmission coefficient along the $z = +L/2$ interface. Since both laser-like regions have the same wave function, the x −dependent part, i.e. $\nu(x)$, is the same as the one in region A. In the isolator region, H_y field would be defined as

$$\begin{aligned} H_B(x,z) = {} & a_{r1}\nu_{r1}(x)e^{-\gamma_{r1}z} + a_{r2}\nu_{r2}(x)e^{-\gamma_{r2}z} + a_{s1}\nu_{s1}(x)e^{\gamma_{s1}z} \\ & + a_{s2}\nu_{s2}(x)e^{\gamma_{s2}z} \end{aligned} \tag{196}$$

where "a" refers to the amplitudes of the modes, and "$r1, r2$" are used for the first and second forward modes, while "$s1, s2$" are used for the first and second backward ones respectively. On the other hand, the simplified transverse electric field can be represented as

$$E_B(x,z) \cong a_{r1}\gamma_{r1}\frac{\nu_{r1}(x)}{\kappa_B(x)}e^{-\gamma_{r1}z} + a_{r2}\gamma_{r2}\frac{\nu_{r2}(x)}{\kappa_B(x)}e^{-\gamma_{r2}z} - a_{s1}\gamma_{s1}\frac{\nu_{s1}(x)}{\kappa_B(x)}e^{\gamma_{s1}z} - a_{s2}\frac{\nu_{s2}(x)}{\kappa_B(x)}e^{\gamma_{s2}z} \quad (197)$$

If we match the fields at the $z = +L/2$ interface, the continuity equations would be

$$a_{r1}\nu_{r1}(x)e^{\frac{-\gamma_{r1}L}{2}} + a_{r2}\nu_{r2}(x)e^{\frac{-\gamma_{r2}L}{2}} + a_{s1}\nu_{s1}(x)e^{\frac{\gamma_{s1}L}{2}} + a_{s2}\nu_{s2}(x)e^{\frac{\gamma_{s2}L}{2}} = T_{BC}\nu_A(x) \quad (198)$$

$$a_{r1}\gamma_{r1}\frac{\nu_{r1}(x)}{\kappa_B(x)}e^{\frac{-\gamma_{r1}L}{2}} + a_{r2}\gamma_{r2}\frac{\nu_{r2}(x)}{\kappa_B(x)}e^{\frac{-\gamma_{r2}L}{2}} - a_{s1}\gamma_{s1}\frac{\nu_{s1}(x)}{\kappa_B(x)}e^{\frac{\gamma_{s1}L}{2}} - a_{s2}\frac{\nu_{s2}(x)}{\kappa_B(x)}e^{\frac{\gamma_{s2}L}{2}} = T_{BC}\gamma_A\frac{\nu_A(x)}{\kappa_A(x)} \quad (199)$$

Eq. (199) should be multiplied by $\kappa_B(x)$ so that the two boundary conditions at $z = +L/2$ would be in the same form. Also, the overlap integrals for each mode direction is to be defined by Eq. (200):

$$(r1, r2) = \int_{-\infty}^{+\infty} dx\, \nu_{r1}(x)\nu_{r2}(x), \quad (s1, s2) = \int_{-\infty}^{+\infty} dx\, \nu_{s1}(x)\nu_{s2}(x) \quad (200)$$

In the same fashion, the overlap integrals for the modes in two different regions are

$$(r1, H_A) = \int_{-\infty}^{+\infty} dx\, \nu_{r1}(x)\nu_A(x), \quad (s1, H_A) = \int_{-\infty}^{+\infty} dx\, \nu_{s1}(x)\nu_A(x) \quad (201)$$

$$(r1, E_A) = \int_{-\infty}^{+\infty} dx\, v_{r1}(x) \frac{\kappa_B(x)}{\kappa_A(x)} v_A(x), \quad (s1, E_A) = \int_{-\infty}^{+\infty} dx\, v_{s1}(x) \frac{\kappa_B(x)}{\kappa_A(x)} v_A(\quad (202)$$

where the modes are normalized. In order to include the overlap integrals, Eq.'s (198) and (199) need to be multiplied by the transverse mode n where $n = r1, r2, s1, s2$. After integrating Eq. (198), the result would be

$$a_{r1}(n, r1) e^{\frac{-\gamma_{r1} L}{2}} + a_{r2}(n, r2) e^{\frac{-\gamma_{r2} L}{2}} + a_{s1}(n, s1) e^{\frac{\gamma_{s1} L}{2}} + a_{s2}(n, s2) e^{\frac{\gamma_{s2} L}{2}} = T_{BC}(n, H_A) \quad (203)$$

After integrating Eq. (199), Eq. (204) would be obtained:

$$a_{r1}\gamma_{r1}(n, r1) e^{\frac{-\gamma_{r1} L}{2}} + a_{r2}\gamma_{r2}(n, r2) e^{\frac{-\gamma_{r2} L}{2}} - a_{s1}\gamma_{s1}(n, s1) e^{\frac{\gamma_{s1} L}{2}} - a_{s2}(n, s2) e^{\frac{\gamma_{s2} L}{2}} = T_{BC}\gamma_A(n, E_A) \quad (204)$$

After executing the same equations (i.e. from Eq.'s (198) to (204)) for the input interface at $z = -L/2$, the electric and the magnetic field boundary conditions would be

$$a_{r1}(n, r1) e^{\frac{\gamma_{r1} L}{2}} + a_{r2}(n, r2) e^{\frac{\gamma_{r2} L}{2}} + a_{s1}(n, s1) e^{\frac{-\gamma_{s1} L}{2}} + a_{s2}(n, s2) e^{\frac{-\gamma_{s2} L}{2}} = (1 + R_{AB})(n, H_A) \quad (205)$$

$$a_{r1}\gamma_{r1}(n,r1)e^{\frac{\gamma_{r1}L}{2}} + a_{r2}\gamma_{r2}(n,r2)e^{\frac{\gamma_{r2}L}{2}} - a_{s1}\gamma_{s1}(n,s1)e^{\frac{-\gamma_{s1}L}{2}} - a_{s2}(n,s2)e^{\frac{-\gamma_{s2}L}{2}} = (1-R_{AB})\gamma_A(n,E_A) \quad (206)$$

There would be sixteen equations in total with six unknown coefficients following the match of all boundary conditions. Our programming tool solves these relations by utilizing them as an $Ax = b$ matrix. Solving all these orthogonality and overlap integral relations, the field and intensity profiles as well as the isolation and insertion loss plots would be generated for each trial.

4.7 Isolation Ratio and Insertion Loss

The *isolation ratio* is one of the critical performance metrics for optical isolators. It is described as the ratio of the backward output power to the forward output power [11]. If the output power is defined with P_o, and the input power is with P_i, the relationship between them after a length L in μm is

$$P_o = P_i e^{-2\alpha L} \quad (207)$$

when 2α is the power loss in μm^{-1}.

$$log_{10}\left(\frac{P_o}{P_i}\right) = -2\alpha L.\, log_{10}e \quad (208)$$

and $log_{10}e$ is in the order of 0.43. Power loss in dB is defined as [89]:

$$10.log_{10}\left(\frac{P_o}{P_i}\right) \tag{209}$$

which refers to the equation of

$$Power\ Loss\ (dB) = 8.6 * \alpha L \tag{210}$$

Therefore, the isolation ratio in dB unit would be

$$10.log_{10}\left(\frac{P_{ob}/P_{ib}}{P_{of}/P_{if}}\right) \tag{211}$$

when subscript "b" is for the backward power, and the subscript "f" is for the forward one. Then, the equation for the isolation ratio is

$$10.\left[log_{10}(P_{ob}/P_{ib}) - log_{10}(P_{of}/P_{if})\right] \tag{212}$$

Therefore, the difference between the backward and forward output power losses in dB unit would be the isolation ratio, which is seen in the figures of the following sections. Then, the *insertion loss* is the forward power loss in dB, which is as follows

$$10.log_{10}\left(P_{of}/P_{if}\right) \quad (213)$$

4.8 The TM Mode Results for the Fe-embedded Case

Because ferromagnetic metals show promising magneto-optic effect, which will be explained in more detail in Chapter 5, Fe metal is focused on first in this section. In the quantum-well region of the device −with Fe metal as a magneto-optic layer− in Figure 4.1, there is an InP substrate; five InGaAsP multi-quantum wells (each $10\,nm$); four InGaAsP barriers in between the quantum well layers (each $10\,nm$); two InGaAsP barriers outside the quantum well layers (each $50\,nm$); and an InP upper-cladding layer. There is also a metal contact layer in order to inject appropriate current into the quantum well laser region on the left. The same laser region on the left side is extended through the right isolator region, as shown in Figure 4.1. On top of the laser region, there is an InP cladding layer with a thickness of $1.61\,\mu m$, and on top of the cladding layer there is an isolator region. Within the isolator region, there are four thin iron layers (each of which is $1\,nm$-thick). These layers are stacked alternatingly with four Silicon layers. Our programming tool changes the Silicon layer thicknesses iteratively from $\sim 90\,nm$ to $\sim 77.5\,nm$ at each algorithmic run.

After running this iterative process, the $x-\beta$ plot of the Iron-Silicon alternated waveguide isolator is obtained as in Figure 4.4. The region where the modes get close to

each other can easily be observed in the dashed lines within Figure 4.4 where the thickness of the overall Silicon layer versus β-profile is varying. βs refer to the propagation constants for the TM_0 and TM_1 modes. They get close when the two modes highly couple to each other.

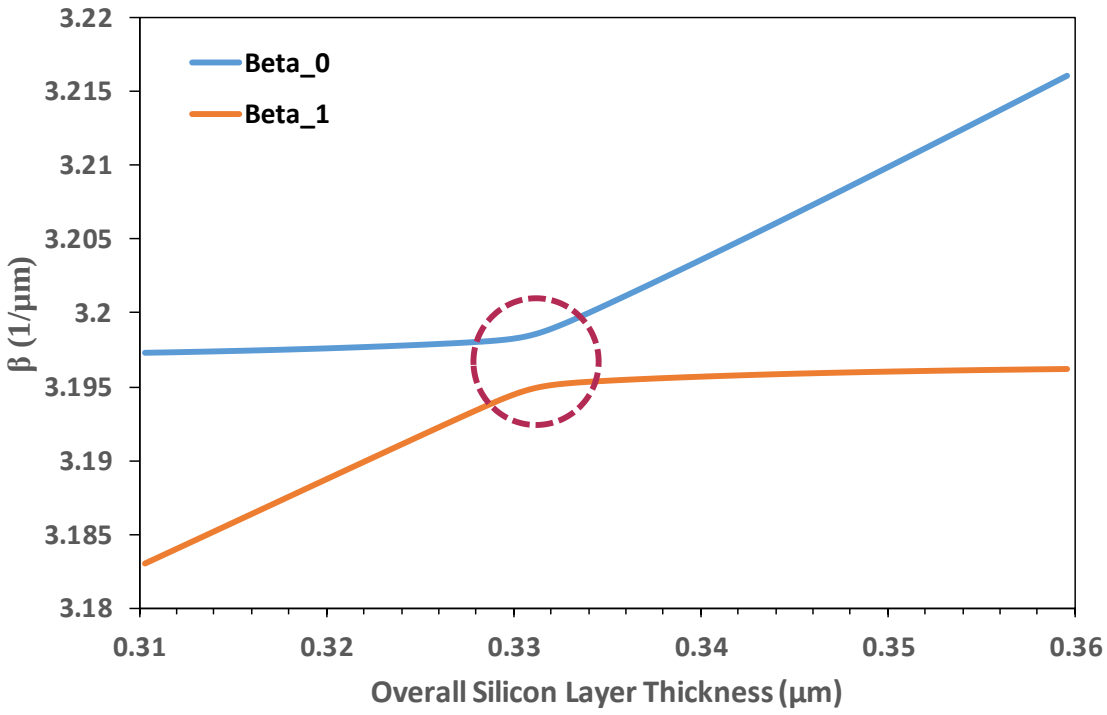

Figure 4.4 The plot for the real part of the propagation constant β versus resonant layer thickness for Iron-Silicon alternating layer embedded waveguide isolator

Figure 4.4 shows that at around 0.33 μm total Silicon layer thickness (indicated by the dashed lines), the two modes –TM_0 and TM_1– approach each other showing that the amount

of coupling between them is large. The total power can be distributed in between MQW and isolator regions via coupling of the two layers. By utilizing our custom-designed NAG-Fortran based programming tool (ISOLATOR software), the layer parameters are effectively and efficiently optimized. As the performance metric of our device, the isolation/insertion loss behavior can be observed in Figure 4.5. ISOLATOR software is used to reveal the loss configurations along the forward and backward directions (i.e. H+ and H- respectively), with regard to the change in the device length.

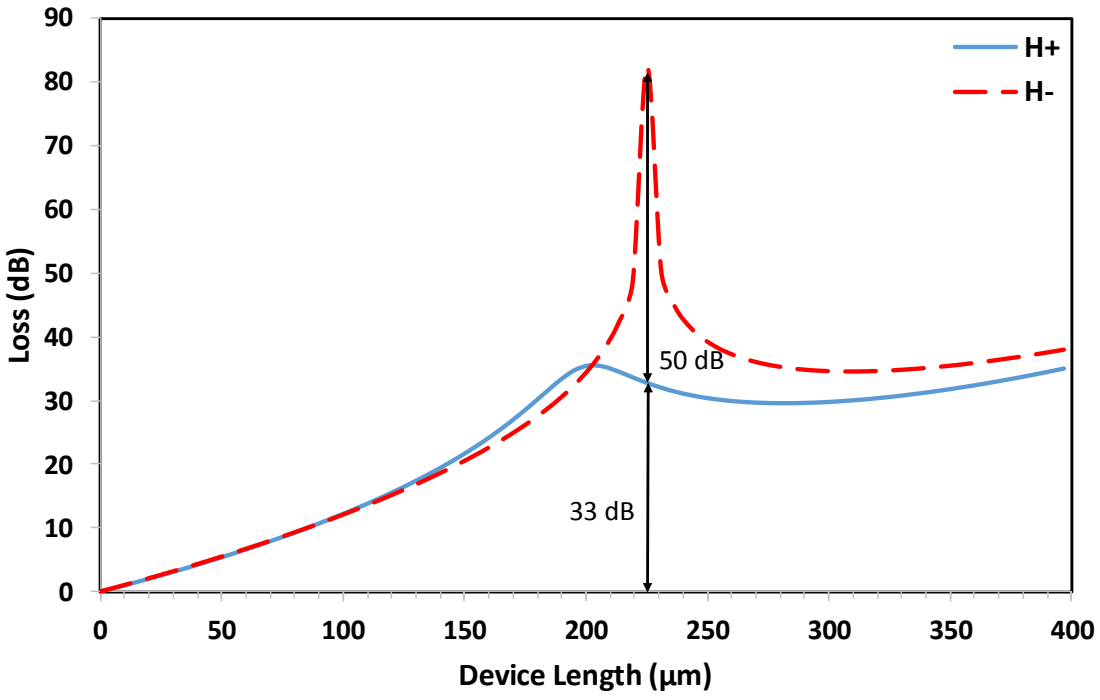

Figure 4.5 Isolation and insertion loss plot for the waveguide isolator with four thin Fe layers

The program iteratively changes the Si-layer thickness. We choose the one, as illustrated in Figure 4.5, in which the amount of backward loss is at its peak. For that structure, this peak value is yielded when the resonant layer thickness of the Iron-Silicon isolator is $0.335\ \mu m$. At the highest backward loss case, the intensity is confined mainly in the lossy magneto-optic region instead of the MQW layer. The main principle of the isolator behavior proposed in this current work is the confinement of backward loss in the isolator region. When the backward light is confined in the isolator region, that prevents the reflections coming back to the laser. Due to the non-reciprocity in magnetically biased magneto-optical devices along + and – directions of the propagation, the forward loss is observed to be completely different than the backward loss. The isolation/insertion loss of the device with four thin iron layers (in total thickness of $4\ nm$) is seen in Figure 4.5. The isolation ratio is $\sim 50\ dB$ while the insertion loss is $\sim 33\ dB$. The main reason of the significantly considerable isolation ratio can be attributed to the large off-diagonals of iron (i.e. $Im[\varepsilon_{xy}] = 1.82$ [86]). On the other hand, having a big amount of insertion loss of iron is due to its large extinction coefficient, which is 5.6 [90].

In the proposed alternating layer structure, there are four thin iron layers at the thickness of $1\ nm$ each ($4\ nm$ in total). When the number of iron layers is gradually decreased from four to one (and concurrently the silicon layers reduced from four to two) iteratively by keeping the overall iron thickness the same level at $4\ nm$, it is demonstrated

that the insertion loss reduces to $\sim 23\ dB$ which is $10\ dB$ less than the case with four iron layers. The isolation/insertion loss behavior for one iron layer is plotted in Figure 4.6.

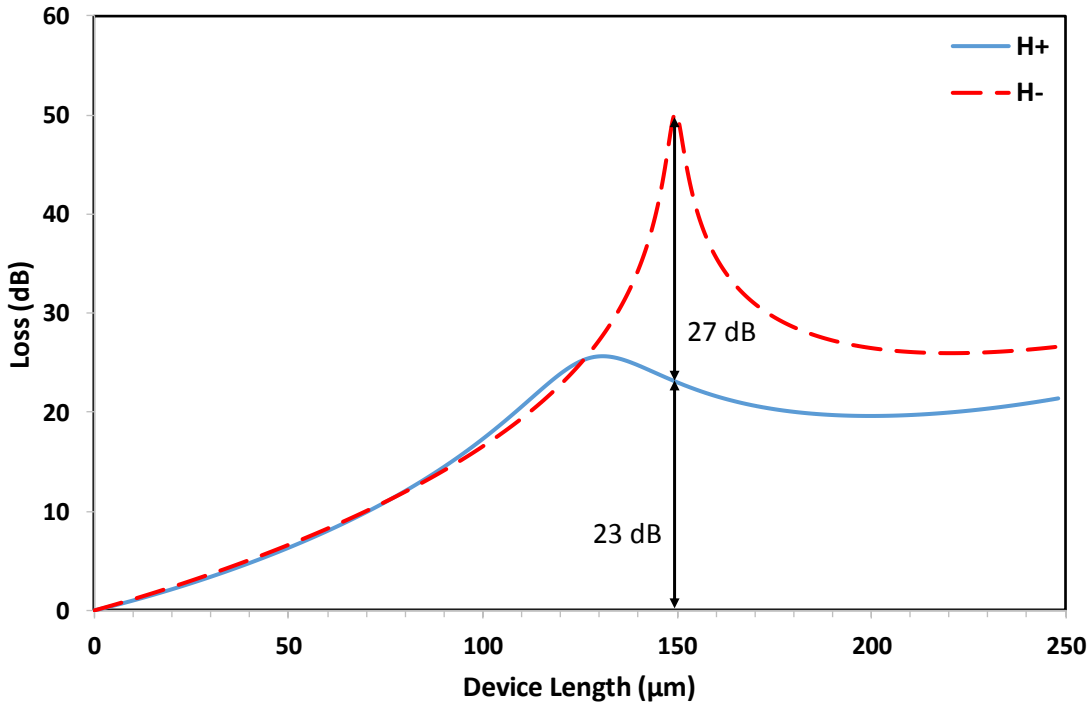

Figure 4.6 Isolation and insertion loss plot for the one Fe layer structure

The thickness of the resonant layer is observed to be $\sim 0.335\ \mu m$ with the one iron layered structure as it was with the four iron layered one. The isolation ratio observed in Figure 4.6 is $\sim 27\ dB$ which is smaller than with the four iron layered structure. However, the insertion loss becomes $23\ dB$, which indicates the one-iron layer is superior to the four-layer case. Although smaller insertion loss values can be yielded once the number of lossy

ferromagnetic layers is decreased, this study shows that pure ferromagnetic metals are not suitable candidates to be used in optical isolators.

CHAPTER 5

5 OPTICAL WAVEGUIDE ISOLATORS WITH ALTERNATING LAYERS OF MAGNETO-OPTIC LAYER AND SILICON

5.1 Introduction and Literature Review

Optical isolators are imperative components in optical communication systems for protecting lasers from undesirable back reflections in addition to the fact that they are crucial in terms of restraining the injection noise of a laser coming from the reflected light [7]-[8]. Currently, commercial optical isolators are free-space Faraday rotators which cannot be integrated to InP-based or Silicon-based optoelectronic devices monolithically. Since free-space, bulk optical isolators are large and expensive, numerous researches have been done to propose integrated optical isolators [7], [11]- [16], [19]-[24], [92]-[93]. Some benefits of on-chip integrated isolators are low cost, small size fabrication ability on a single wafer, and mechanical stableness of the optical system [7], [94]-[95]. Magneto-optic materials are commonly used in optical isolators to break the time-reversal symmetry by the help of the off-diagonal elements' presence in the dielectric tensor, ε [95]-[96]. By breaking the time-reversal symmetry, the degeneracy between forward and backward light could be removed which permits nonreciprocal propagation of light [95]-[98]. Initial isolator studies utilize TE-TM mode conversion [9]-[10], which basically resembles bulk

Faraday rotators. In order to have enough mode conversion for isolator operations, there needs to be phase matching for TE and TM modes which would make the device sensitive to changes in waveguide parameters and as a result practically unusable.

Initial works for proposing integrated isolators are basically depends on two different systems: One is the interferometric optical isolators with ferrimagnetic garnets as magneto-optic material [7], [19]-[24], the other one is the active waveguide optical isolators with common ferromagnetic elemental metals like Fe, Co, or Ni [11]-[16], [92]-[93]. Firstly, the semiconductor optical amplifier (SOA) type optical isolators with ferromagnetic metal layer will be reviewed.

Some of the ferromagnetic elemental metals, such as Fe, Co, or Ni, have been widely utilized in SOA-type isolators as they have a relatively higher magneto-optic effect than other materials [11]-[13], [16], [87], [92], [100]-[101]. This feature can be attributed mainly to their larger imaginary parts of off-diagonal elements, i.e. $Im[\varepsilon_{xy}]$ of the relative permittivity tensor ε, at around $\lambda = 1550\, nm$ telecommunication wavelength [92]. Another reason for pure ferromagnetic metals to be used as a magneto-optic material is that they could be easily deposited on top of the semiconductor layers through sputtering or electron-beam evaporation [14], [92].

The very first two theoretical studies on using ferromagnetic metals in active waveguide isolator systems were completed by Takenaka *et al.* [11] and Zaets *et al.* [12].

Takenaka *et al.* used Fe and Ni while Zaets *et al.* used Co in their analyses. In all ferromagnetic layer-embedded active waveguide devices, there is a semiconductor optical amplifier (SOA) layer which pumps light by the help of a current injection [11]-[16], [92]-[93]. As examples, Vanwolleghem *et al.* [13]-[14] utilized ridge waveguide semiconductor laser as a SOA in his work which was the first experimental demonstration of monolithically integrated waveguide isolator, while Shimizu *et al.* [15] utilized InGaAsP edge-emitting multi-quantum well laser that was the first depiction of nonreciprocal loss shift in semiconductors.

In these systems, a magnetic bias is transversely applied so as to trigger the magneto-optic Kerr effect (MOKE). Their ferromagnetic layers are placed either as an upper clad [13]-[14], [16],[92]-[93] or as a side clad [15]-[16] to provide nonreciprocal loss. The systems that use ferromagnetic layer as an upper clad can also utilize it as a metal contact [13]-[14]. Forward loss in these systems is compensated with the optical gain stemming from the active SOA layer. Since backward loss is not fully compensated, the desired behavior of the isolator can be obtained [13]-[16], [92]-[93], [100]. Even though integration of optical isolators with SOA is an important milestone in the optoelectronics field, utilizing SOA gain to compensate the forward loss remains a problem within the above-mentioned studies, since SOA provides additional noise to the system [17]. To the best our knowledge, until now the only study that does not utilize SOA gain for the compensation of forward loss is Hammer *et al.*'s 2006 work [18]. They propose having a

semiconductor waveguide type optical isolator with ferromagnetic iron nanoparticles embedded in an InGaAsP layer. However, in their work, the extinction ratio of iron is reduced on the order of 1/30, which provides overly optimistic loss results of 2-4 dB.

SOA-type optical isolators with ferromagnetic metal layers are mostly based on the nonreciprocal loss shift [13]-[16], [100]. For example, in Shimizu *et al.*, the TE mode intensity drops for 7 dB at the 1560 nm operating wavelength upon the change of magnetic bias direction [15]. In Amemiya *et al.*[16], the nonreciprocal loss shift obtained as 8.8 dB/mm at 1540 nm wavelength of operation. Different from the works all above, Shimizu *et al.* analyzed the InGaAsP active waveguide interferometric optical isolator with Cobalt layer theoretically [92]. They included the effect of nonreciprocal phase shift (NRPS) in their calculations which estimates the isolation ratio larger than 30 dB at the 1550 nm operating wavelength. Additionally, in 2010, Shimizu and his colleagues fabricated Fe layer embedded InGaAlAs/InP active waveguide optical isolator based on nonreciprocal polarization rotation operating at 1295 nm. Extinction ratio for the system is 18.3 dB while nonreciprocal loss is 3 dB/mm [93].

Although aforementioned ferromagnetic metals' off-diagonal elements demonstrate promising behavior in terms of nonreciprocal property, their optical absorptions are very high as well, which makes the isolators fairly lossy. To solve this problem, Amemiya *et al.* [16] utilize a MnAs compound as a ferromagnetic layer instead of an elemental ferromagnetic metal in their active waveguide optical isolator to decrease

the resistance between metal and InP-based SOA since the resistance gets larger values for Fe and Ni elements. However, insertion loss stemming from the MnAs layer is 25 dB, which is still quite high [16]. Although common ferromagnetic metals -Fe, Co and Ni- can easily be deposited over semiconductors through electron-beam evaporation or sputtering techniques [14], [92], their loss values are very large that negates them from being the best candidates for optical isolators.

In a similar fashion, interferometric isolators were also devised for the purpose of fabricating integrated optical isolators [7], [19]-[24]. Both interferometric isolators as well as built-in semiconductor optical amplifier type isolators do not necessitate strict phase matching requirements -for TE-TM modes- and rigid control of waveguide parameters too that make these isolators easy to operate [19], [103]. Yttrium iron garnet ($Y_3Fe_5O_{12}$-YIG) materials are commonly used as part of Mach-Zender interferometric isolators for nonreciprocal operations, as they have a substantial amount of magneto-optic effect and low optical absorption [7], [104]. Also, Gomi *et al.* discovered that Ce^{+3} substituted yttrium iron garnet has higher Faraday rotation than Bi^{+3} substituted iron garnets [105]. As a well-accepted reference to the literature, Shintaku *et al.* measured the loss for Ce:YIG thin film as $5.8\,dB/cm$ which makes the extinction coefficient as 1.66×10^{-5} while Faraday rotation was $3300\ deg/cm$ for the TM mode [106].

After mentioning the benefits of low-loss YIG materials, next we detail the literature on interferometric isolators which utilized YIG layers as magneto-optic

materials. In 1986, Okamura *et al.* developed a YIG rib waveguide embedded Mach-Zender interferometer and showed the nonreciprocity by using nonreciprocal phase shift [16] and then in 1993, Mizumoto *et al.* [19] fabricated another Mach-Zender interferometer with a tapered coupler at 1310 nm wavelength. Mizumoto *et al.* grew rare earth iron garnet $(\mathrm{LuNdBi})_3(\mathrm{FeAl})_5\mathrm{O}_{12}$ as a magneto-optic material in their work [19]. As it can be understood, Mach-Zender interferometer type optical isolators typically exploit a nonreciprocal phase shift by placing two nonreciprocal phase shifters as well as one reciprocal phase shifter in the two arms of the interferometer [19]-[23]. The phase differences of nonreciprocal and reciprocal phase shifters add up to a $180°$ phase shift in between two light waves coming from the two arms of the interferometer. In 1999 and 2000, Yokoi and Mizumoto developed two different Mach-Zender interferometers as rib waveguides. The difference in between two studies is that the magneto-optical layer was used as a guiding layer in 1999 work [20] while it was utilized as an upper-clad in 2000 work [21]. They reported an isolation value of $4.9\ dB$ (at the operation wavelength of $1550\ nm$) even though for the ideal case they claimed it is possible to achieve an isolation ratio larger than $17\ dB$ [21]. In contrast to the conventional interferometric isolators, Shoji *et al.* theoretically adjusted the amount of reciprocal phase shift to attain wideband operation [22]. In 2006, by doing adjustment in the shifters, they improved the isolation ratios up to 46 dBs theoretically. Then, in 2008, they experimentally developed Si rib wire waveguide type Mach-Zender interferometer, which had an isolation of $21\ dB$ at 1559 nm

wavelength [23]. Total insertion loss for their structure was 8 dB. So far, interferometric isolators have a large footprint because of the phase shift requirements which constitutes a problem for the on-chip applications. Briefly, there is a gap in the literature as to how magneto-optic materials would be integrated with SOAs monolithically.

Integration of magnetic garnets with semiconductor waveguides has been a challenging task, since large lattice mismatches form in between the semiconductor and magnetic garnets. Numerous studies have reported to solve this issue. Direct-bonding technique was commonly used to integrate Ce:YIG and semiconductor layer [21]-[22]. Shoji *et al.* utilized surface-activated direct bonding technique during the integration process of Ce:YIG to Si waveguide [23]. A more recent study of Ghosh et al. touches base upon adhesive bonding usage for integration of Ce:YIG layer to silicon on insulator (SOI) waveguide in a Mach-Zender interferometer type optical isolator [24]. They deposited adhesive polymer in between Ce:YIG and SOI layers. Achieved isolation ratio is 25 dB, while insertion loss is 14 dB at 1550 nm [24]. Mizumoto and his friends worked on interferometric as well as semi-leaky optical waveguide isolators by applying surface activated direct bonding technique [7]. The bonding method was established for bonding between Ce:YIG to III-V semiconductors, as well as Ce:YIG to Silicon and Ce:YIG to $LiNbO_3$ in Mizumoto *et al.*'s previous works [107]-[109]. In that mechanism, they activated the surface by bombarding with argon or other ions in a vacuum chamber for 10-30 seconds. After bringing the two surfaces together, they pressed the layers against each

other at higher temperatures [7]. The temperature for that procedure was kept around $250℃$ which is in fact very low compared to the annealing trials for the same purpose [110]-[111]. To exemplify, Goto *et al.* fabricated a nonreciprocal racetrack resonator [110]. They deposited a thin Ce:YIG layer over Silicon and Silica layers via the use of RF magnetron sputtering and then applied high temperature rapid thermal annealing in order to observe crystallinity behavior as well as magneto-optic behavior after basic sputtering. They claimed that below $600℃$, there is no crystallinity for the Ce:YIG material; therefore, there is no nonreciprocal property either. However, in the case of the integrated SOA type isolator, that high of a temperature can be harmful to the laser.

In this study, we propose and theoretically analyze the first semiconductor active waveguide optical isolator with low-loss Ce:YIG layers as a magneto-optic material, operating at a $1.55\ \mu m$ telecommunication wavelength. Different from the literature [13], [93], [100], our device does not utilize the optical gain as a compensation tool for the forward loss. It performs in the TM-mode; therefore, there is no need for the TE-TM mode matching. By using the ISOLATOR software, we can measure nonreciprocal loss shifts. In addition to the semiconductor waveguide isolator with thin Ce:YIG layers, some of the ferromagnetic metal layers are also used (i.e. Fe, Co, and Ni), as magneto-optic materials, to contribute a novel comparative study to the literature.

5.2 Structure of the Proposed Isolator with Alternating Layers of Magneto-Optic Material

As shown in the 4th chapter, the structure of the semiconductor waveguide optical isolator based on nonreciprocal loss shift is pictorially depicted in Figure 5.1. In the design of all four structures, there are two sub-waveguides, which are monolithically integrated to each other to form one waveguide: One is a tunable multi-quantum well (MQW) InGaAsP/InP laser operating at 1.55 μm and the other one is the isolator region, which is a combination of alternating layers of the magneto-optic material and Silicon.

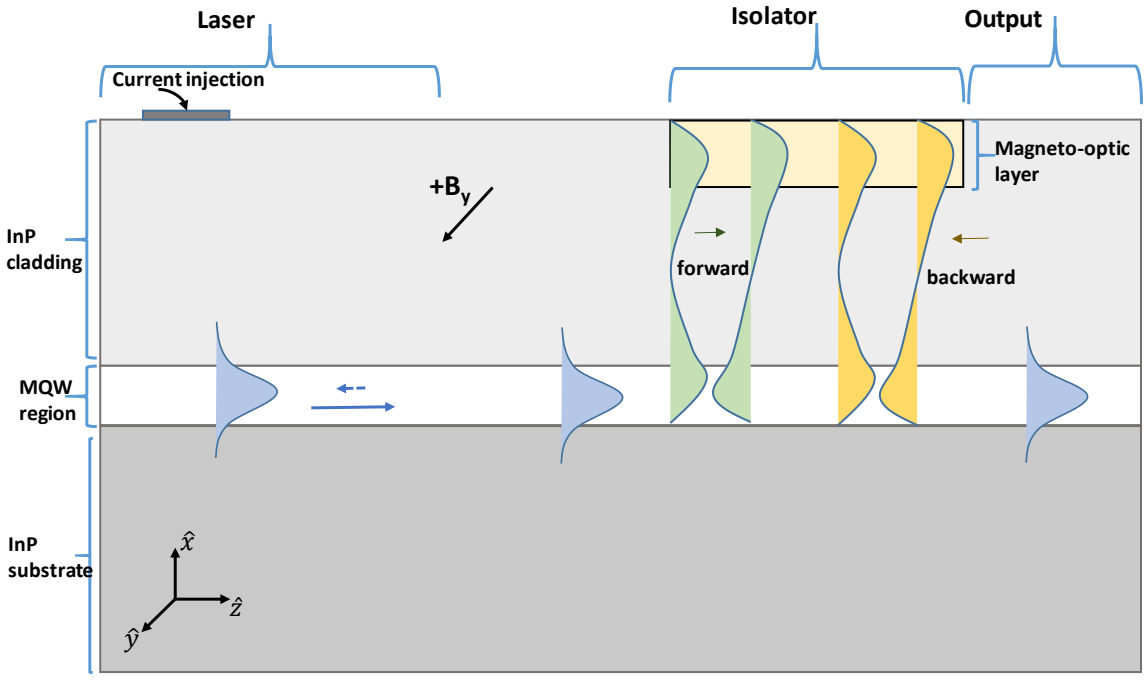

Figure 5.1 Two dimensional structure of the proposed isolator

Table 5.1 The isolator structure with Ce:YIG layer.

Layer material	Thickness (nm)	Refractive index (n)
Air	∞	1
Si	100	3.476
Si	~350	3.476
Ce:YIG	80	2.21
Si	~350	3.476
Ce:YIG	80	2.21
Si	~350	3.476
InP Clad layer	424	3.16492
Barrier InGaAsP	200	3.23858
3 QW InGaAsP	7	3.56288
4 Barriers InGaAsP	10	3.30540
Barrier InGaAsP	200	3.23858
InP substrate	∞	3.16492

In the waveguide region of the isolator with thin Ce:YIG layers, there are an InP substrate, three InGaAsP multi-quantum wells (each 7 nm), four InGaAsP barriers (each 10 nm), two more thick InGaAsP barrier layers deposited on the upper and lower sides of the QW laser (each 0.2 μm), and an InP upper-cladding layer. There is also a metal contact layer for current injection purposes on the left QW active side of the structure. As Figure 5.1 shows, the same laser waveguide is extended through the isolator region. On top of the

laser waveguide, there is a $0.424\ \mu m$-thick InP cladding layer, and on top of the cladding layer there is an isolator region. Within the isolator region, there are two thin Ce:YIG layers (each of which is $80\ nm$-thick), which are stacked in between three Silicon layers. The thicknesses of the Silicon layers change from $\sim 380\ nm$ to $\sim 290\ nm$ for iteration purposes, and there is one more $0.1\ \mu m$-thick Silicon layer on top of the device. The refractive indices of each layer for the isolator structure with Ce:YIG can be seen in Table 5.1.

The structure of the Fe, Co, Ni layer embedded systems are somewhat different than the structure with thin Ce:YIG layers. In the quantum-well region of ferromagnetic pure metal systems, there is an InP substrate, five InGaAsP multi-quantum wells (each $10\ nm$), four InGaAsP barriers inside the quantum well layers (each $10\ nm$), and two InGaAsP barriers outside of the quantum well layers (each $50\ nm$) and a thick InP upper-cladding layer. There is also a metal contact layer for current injection purposes on the left QW active side of the structure the same as the structure with thin Ce:YIG layers. As seen Figure 5.1, the same laser region on the left side is extended through the right isolator region. On top of the laser region, there is an InP cladding layer with a thickness of $1.5\ \mu m$ and on top of the cladding layer there is an isolator region. Within the isolator region, there is a thin ferromagnetic metal layer ($4\ nm$-thick) which are stacked in between two Silicon layers each of whose thicknesses are changing from $\sim 155\ nm$ to $\sim 180\ nm$ for iteration purposes. The refractive indices of each layer for the isolator structure with magneto-optic metals Fe, Co, and Ni can be seen in Table 5.2.

Table 5.2 The isolator structure with magneto-optic metals Fe, Co, and Ni.

Layer material	Thickness (nm)	Refractive index (n)
Air	∞	1
Si	155-180	3.476
Metal	4	n_{metal}
Si	155-180	3.476
InP Clad layer	1500	3.1628
Barrier InGaAsP	50	3.37
5 QW InGaAsP	10	3.46
4 Barriers InGaAsP	10	3.37
Barrier InGaAsP	50	3.37
InP substrate	∞	3.1628

5.3 Design and Methodology

In this study, a magnetic field B_y is applied through $\hat{y}$ −direction and its direction is then reversed to simulate forward and backward lights. The basic principle for this optical waveguide isolator is the coupling of the two main sub-waveguides, which shows different behavior for forward and backward waves due to the non-reciprocity. The alternating layer structure gives us a way to distribute high-loss ferromagnetic metals into thick Si layers to achieve the coupling mechanism between the isolator and the MQW laser structure. Considering Ce:YIG's refractive index, which is as low as 2.21 (whereas the

laser's is ~ 3.26) it is wiser to stack Ce:YIG layers inside the thick Si layers. This helps us adjust the net refractive index of the isolator region. The monolithic integration of these two sub-waveguides, which is important in tandem with the alternating layer structure, can be realized by depositing alternating layers of the isolator structure above the QW laser.

As shown in Figure 5.1, sending an injection current creates the laser light in the left side of the InGaAsP multi-quantum well (MQW) region. The laser light excites the two isolator modes when it reaches the isolator region, and via coupling of the two layers, we can distribute the power in between the MQW and magneto-optic (MO) regions. With proper optimization of layer parameters, we can confine backward light mainly to the lossy isolator section, which is the desired isolator behavior in the proposed device configuration. A home-grown photonic programming tool (ISOLATOR software) is utilized to comparatively check the loss configurations along the forward and backward directions upon the change of silicon layer thicknesses in the isolator region. From all iterations for various Si layer thicknesses in between $\sim 380\, nm$ and $\sim 290\, nm$, we select the one in which the amount of backward loss is at its peak, for the Ce:YIG case. At that high backward loss point, the intensity is confined mainly in the lossy magneto-optic layer instead of the MQW layer, which is the main principle of the isolator behavior proposed in this current work. Because of the non-reciprocity in magnetically biased magneto-optical devices along the + and – directions of the propagation, the forward loss is completely different from the backward loss. For the structure with Ce:YIG layers, we can get a fairly

low forward loss of 0.47 dB/mm by proper optimization of InP clad and Si layers, which also provides high amounts of isolation ratios.

5.3.1 Methodology for the Proposed Design

In order to design the alternating-layered isolator structure, first, each of the two sub-waveguides is to be analyzed separately. By using a simple *Mode Solver Tool*, the equivalent three-layer waveguide for the complex laser structure is formed. Then, we form another three-layer structure for the magneto-optic region. As the following step, we combine the two three-layer waveguides into a five-layer waveguide by properly adjusting the cladding spacer thickness in order to obtain a decent amount of power distribution between the two sub-waveguides. After combining these two waveguides together, two coupled modes would emerge, which are TM_0 and TM_1. Then, we check the β plots for the TM_0 and TM_1 modes as shown in the previous chapter within the Figure 4.4. The β plots are drawn for varying magneto-optic layer thicknesses. The combined waveguide yields considerable amount of coupling when the two modes gets close to each other in the β plot. Therefore, we use the range of the magneto-optic thickness for the isolator design in the WAVEGUIDE software.

As the second step, we use the WAVEGUIDE software to design the actual multi-layer structure including all layers. The laser waveguide parameters are entered to the program to find the effective index of the laser. Then, we design another waveguide which

contains several magneto-optic layers as well as host material layers (silicon for this study). As shown in Figure 5.2 (a), the separate effective indices of each sub-waveguide (i.e. the magneto-optic region and the laser) should be matched with one another.

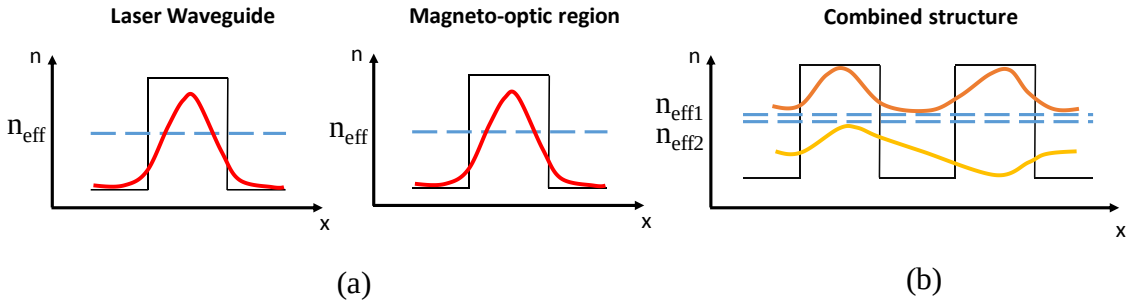

Figure 5.2 (a) The effective index matching and the field profile of the separate two waveguides (b) The combined structure of the two sub-waveguides with the TM_0 and TM_1 modes

By adjusting the thicknesses of each the magneto-optic multi-layer region, we can attain the effective index matching of the isolator with the QW laser, which is the initial step necessary to analyze the two sub-waveguides together. Then, the two separate waveguides are combined into one waveguide. After bringing the two separate waveguides in close proximity, the main effective index is split into two therefore, there would be two TM_0 and TM_1 modes. The second peak formation can be seen in magneto-optic region Figure 5.2 (b). Cladding spacer thickness is adjusted to obtain substantial intensity in both peaks of the TM_0 and TM_1 modes. By the help of coupling between these two sub-

waveguides, we would be able to distribute the power along both waveguides which is one of the main properties of the isolator behavior in this work.

After observing a significant coupling between the two sub-waveguides, we transfer the multi-layer isolator structure to the ISOLATOR software. By the help of this software, we can include the effect of magnetic field as well as the off-diagonal dielectric tensor within the computations and therefore, the nonreciprocity for the forward and backward transmissions of light is obtained. Due to the nonreciprocal behavior originating from the inclusion of magneto-optic materials under the effect of magnetic field, the modes along forward direction are not the same with the modes along the backward direction. Therefore, there would be four modes in total which is a combination of two forward (TM_{F0} and TM_{F1}) and two backward (TM_{B0} and TM_{B1}) modes which can be seen in the field profiles in sections 5.4.1.1, and 5.4.2.1. The isolator behavior in this study could be accomplished by the help of this nonreciprocity along the forward and backward modes.

Since the magnetic effects are included in this software, the program computes and finds new set of β values in terms of varying host material thicknesses for the designed structure (seen in Figure 4.4) across the overall magneto-optic region. As done in the Mode Solver Tool, we focus on the region where the TM_0 and TM_1 modes gets close to each other. The ISOLATOR software provides loss profiles for the forward and backward modes. Forward loss refers to the insertion loss, while backward loss refers to the isolation. Our aim here is to achieve high levels of backward loss and low forward loss. The host

material thickness is altered iteratively by the software to keep track of the isolator's behavior with respect to differing overall magneto-optic region thicknesses. With the help of these loss plots, we can find the best isolation and the lowest insertion loss that the isolator in this study could attain. By following the steps of the same methodology of the ISOLATOR software, different cladding spacer layer thicknesses need to be further investigated to achieve better results for the isolation and insertion loss. The schematic representation of the overall methodology can be found in Figure 7.1 within Appendix 4.

5.3.2 Alternating Layer Structure

We used alternating layer structure in the design of the magneto-optic region in our study. Both the magneto-optic material as well as the thick host material have several layers, which are designed to be located alternatingly one at a time. The host material in our case is silicon layers. The main reason for having alternating layer structure is to achieve coupling between the two sub-waveguides (i.e. the magneto-optic region and the laser). In order to obtain satisfactory levels of coupling, the overall refractive indices of the two sub-waveguides need to be comparable to each other. In our study, thick host material layers are used to achieve a decent amount of coupling in different configurations.

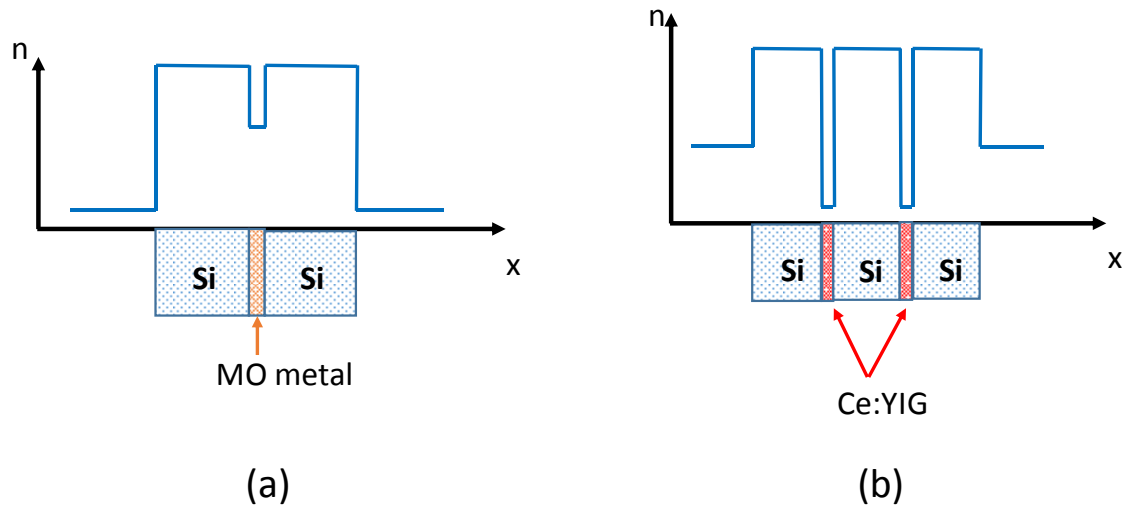

Figure 5.3 The relative refractive index profile for the alternating layer structure of the isolator design with (a) magneto-optic (MO) metals and (b) Ce:YIG material

The alternating layer scheme can be seen in Figure 5.3. For the structure with MO metals, the amount of loss that the Fe, Co, and Ni metals bring to the system is very large. Therefore, it would be more effective to use them as thin metal layers to minimize the optical loss. To maintain the coupling between the two sub-waveguides, a fair amount of thickness in the MO region is essential, which can be obtained by the inclusion of thick semiconductor host material layers. The reason of having such silicon layers for the structures with Ce:YIG material is somewhat different than the reason for the structures with MO metals. The index of refraction is very low for the Ce:YIG material, which is 2.21 (whereas the laser's is ~3.26). Since the refractive index of silicon is 3.476 at the

telecommunication band, in this work we preferred to provide thick layers of silicon to have comparable overall refractive indices of the MO region with the one for the laser.

5.3.3 Onsager's Relations in Magnetic Fields

As mentioned in the previous sections, the static magnetic bias in our system is applied along the $\hat{y}$ −direction, while the light propagation is along the $\hat{z}$ −direction. The relative dielectric tensor for that magnetic bias can be represented as in Eq. (214):

$$\overleftrightarrow{\varepsilon} = \begin{bmatrix} \varepsilon_v & 0 & -\varepsilon_o \\ 0 & \varepsilon_c & 0 \\ \varepsilon_o & 0 & \varepsilon_v \end{bmatrix} \tag{214}$$

ε_c is the diagonal element, which does not have any magnetic field dependence. However, ε_v term has some dependency on the magnetic field. Since the dependency is fairly small, we can assume the relationship between these two diagonal terms to be $\varepsilon_v \cong \varepsilon_c$. The complex off-diagonal element, ε_o is also small compared to the diagonal, ε_c. To simulate the propagation along the forward and backward directions, the polarity of magnetic bias is changed from $+B_y$ to $-B_y$. According to Onsager's reciprocal relationships in magnetic fields [112], off-diagonals of the relative dielectric tensor also change sign upon the change of magnetic field direction, which is outlined as:

$$\varepsilon_{ij}\left(\vec{B}\right) = \varepsilon_{ji}\left(-\vec{B}\right), \qquad i = j \tag{215}$$

When $i = j$ holds true, Eq. (215) refers to the fact that there is no change for the diagonal elements of the dielectric constant. While $i \neq j$ is observed, the relationship in Eq. (216) shows that the change of sign for the off-diagonals in the $\overleftrightarrow{\varepsilon}$ tensor is represented as

$$\varepsilon_{ij}(\vec{B}) = -\varepsilon_{ij}(-\vec{B}), \qquad i \neq j \tag{216}$$

These Onsager relationships reveal the reason for non-reciprocity in magneto-optic isolators under an external magnetic bias.

5.3.4 Nonreciprocal Phase Shift

In our structure there are two separate waveguides which are deliberately designed to accommodate the same propagation constants. When they are merged together by adjusting the separation thickness, there would be coupling of the two separate modes coming from the two waveguides. Then, there would be two different modes which are in close proximity to each other. The newly formed modes are called supermodes. Assume that the propagation constants are assigned as β_e for TM_0 mode and β_o for TM_1. If there is any ferromagnetic or ferrimagnetic inclusion on any parts of the waveguide, and also if we apply an external magnetic field to that system; the off-diagonal elements of the dielectric permittivity tensor would be non-zero. This causes perturbation in the dielectric constant in the order of $\Delta\varepsilon$. The derivations in this section are adopted from Yariv *et al.* [113] and the new form of the dielectric constant can be written as follows:

$$\varepsilon_r(x) = \varepsilon_{ra}(x) + \Delta\varepsilon(x) \tag{217}$$

where $\varepsilon_{ra}(x)$ is the vacuum dielectric tensor and $\Delta\varepsilon(x)$ is the off-diagonal tensor, which are illustrated as

$$\varepsilon_{ra}(x) = \varepsilon \begin{bmatrix} 1 & 0 & 0 \\ 0 & 1 & 0 \\ 0 & 0 & 1 \end{bmatrix} \tag{218}$$

$$\Delta\varepsilon(x) = \begin{bmatrix} 0 & 0 & -\varepsilon_0 \\ 0 & 0 & 0 \\ \varepsilon_0 & 0 & 0 \end{bmatrix} \tag{219}$$

Unperturbed field equation can be defined as

$$\mathbf{E_m} = E_m(x) \exp(i\omega t - i\beta_m z) \tag{220}$$

When we impose the unperturbed field equation into the unperturbed wave equation, the relation would be as:

$$\left[\frac{\partial^2}{\partial x^2} + \omega^2 \mu \varepsilon_{ra}(x)\right] E_m(x) = {\beta_m}^2 E_m(x) \tag{221}$$

The perturbation, $\Delta\varepsilon(x)$, makes the two supermodes β_e and β_o couple to each other. It can be assumed that in Eq. (221), the perturbation would cause small changes in ${\beta_m}^2$ and E_m which are $\delta{\beta_m}^2$ and δE_m, respectively [113]. The perturbed wave equation to the first-order will be

$$\left[\frac{\partial^2}{\partial x^2} + \omega^2\mu\varepsilon_{ra}(x) + \omega^2\mu\Delta\varepsilon(x)\right](E_m + \delta E_m) = \left({\beta_m}^2 + \delta{\beta_m}^2\right)(E_m + \delta E_m) \quad (222)$$

Since the second-order term $(\Delta\varepsilon(x)\delta E_m)$ and the third-order term $(\delta{\beta_m}^2\delta E_m)$ are considerably small, they can be neglected. On the other hand, if we consider the unperturbed wave equation (i.e. Eq. (221)), the newly formed perturbed equation would be as

$$\left[\frac{\partial^2}{\partial x^2} + \omega^2\mu\varepsilon_{ra}(x)\right]\delta E_m + \omega^2\mu\Delta\varepsilon(x)E_m = \left({\beta_m}^2\delta E_m + \delta{\beta_m}^2 E_m\right) \quad (223)$$

Since the modes form a complete orthogonal set, the orthonormalization equation would be as follows [113]:

$$\frac{\beta_m}{2\omega\mu}\iint E_m . {E_n}^* dxdy = \delta_{mn} \quad (224)$$

In addition to that, the perturbation in the field relation $(\delta E_m(x))$ can be written as

$$\delta E_m(x) = \sum_n a_{mn} E_n(x) \quad (225)$$

If we impose Eq. (225) onto Eq. (223), the perturbed wave equation is

$$\left[\frac{\partial^2}{\partial x^2} + \omega^2 \mu \varepsilon_{ra}(x)\right] \sum_n a_{mn} E_n(x) + \omega^2 \mu \Delta\varepsilon(x) E_m = \left(\beta_m{}^2 \sum_n a_{mn} E_n(x) + \delta\beta_m{}^2 E_m\right) \tag{226}$$

In order to simplify Eq. (226), we could utilize the unperturbed equation i.e. Eq. (221) as well. Then, the new perturbed wave equation is

$$\sum_n a_{mn} \beta_n{}^2 E_n(x) + \omega^2 \mu \Delta\varepsilon(x) E_m = \sum_n a_{mn} \beta_m{}^2 E_n(x) + \delta\beta_m{}^2 E_m \tag{227}$$

The further simplified version of Eq. (227) would follow

$$\sum_n a_{mn} \left(\beta_n{}^2 - \beta_m{}^2\right) E_n(x) = \left(\delta\beta_m{}^2 - \omega^2 \mu \Delta\varepsilon(x)\right) E_m(x) \tag{228}$$

By using the orthogonalization property in Eq. (224), we could multiply Eq. (228) by $E_m{}^*$ and integrate over the $x - y$ plane, which converts Eq. (228) to Eq. (229)

$$0 = \iint E_m{}^*(x) \left(\delta\beta_m{}^2 - \omega^2 \mu \Delta\varepsilon(x)\right) E_m(x) \tag{229}$$

Eq. (229) can be transformed to Eq. (230) since $\delta\beta_m{}^2$ is a constant:

$$\delta\beta_m{}^2 = \frac{\iint E_m{}^*(x) \omega^2 \mu \Delta\varepsilon(x) E_m(x) dx dy}{\iint E_m{}^*(x). E_m(x) dx dy} \tag{230}$$

By utilizing orthonormalization property and considering ${\delta\beta_m}^2 = 2\beta_m\delta\beta_m$[113], we obtain $\delta\beta_m$ as follows

$$\delta\beta_m = \frac{\omega}{4}\iint {E_m}^*.(\Delta\varepsilon)\, E_m dxdy \tag{231}$$

$2\delta\beta_m$ is the *nonreciprocal phase shift* (NRPS) coming from the existence of both static magnetic field and gyrotropic inclusions. Therefore, the phases of each mode, are differing from each other on the order of $2\delta\beta_m$ for the forward and backward direction and the new propagation constants for TM_0 is

$$\begin{aligned} \beta_{e+} &= \beta_e + \delta\beta_e \\ \beta_{e-} &= \beta_e - \delta\beta_e \end{aligned} \tag{232}$$

In Eq. (232), β_e refers to the propagation constant when there is no off-diagonal element. After including the off-diagonal element ε_0 (i.e. $\Delta\varepsilon(x)$), the difference between forward and backward propagation constant for the TM_0 mode would be $2\delta\beta_e$. For the TM_1 forward-backward propagation constant, the difference equals to $2\delta\beta_o$ as seen in Eq. (233):

$$\begin{aligned} \beta_{o+} &= \beta_o + \delta\beta_o \\ \beta_{o-} &= \beta_o - \delta\beta_o \end{aligned} \tag{233}$$

If there is no perturbation in the dielectric tensor, the difference in the forward-backward direction of even mode ($\delta\beta_e$) as well as the odd mode ($\delta\beta_o$) would both be zero. Therefore, without ε_0, no difference is observed in the propagation constants for forward and backward direction which translates into the fact that the system does not present nonreciprocal behavior based on Eq. (231).

5.3.5 Device Length – Nonreciprocal Phase Shift (NRPS) Relationship

To minimize the reflected power through backward direction, the destructive interference between even and odd modes should be obtained. For "m" number of interference fringes, the relationship can be illustrated as

$$(\beta_{e-} - \beta_{o-})L = (2m \pm 1)\pi \tag{234}$$

while L is the device length, β_{e-} is the propagation constant for the even mode of the backward direction and β_{o-} is for the odd mode. Likewise, to get maximum amounts of power in the output region, these two modes need to show constructive interference pattern:

$$(\beta_{e+} - \beta_{o+})L = 2m\pi \tag{235}$$

After solving Eq. (234) and Eq. (235), the relation between the device length and nonreciprocal phase shifts is:

$$L = \frac{\pi}{2(\Delta\beta_e - \Delta\beta_o)} \tag{236}$$

In order to obtain the lowest insertion loss, the amount of power through forward direction is to be maximized while the power along backward direction is to be minimized, both of which can be achieved by Eq. (236). Unfortunately, Ce:YIG has quite low $Im[\varepsilon_{xy}]$ which is 6.28×10^{-3} in contrast to the ferromagnetic elemental metals that are being investigated in this letter, which makes $(\Delta\beta_e - \Delta\beta_o)$ difference small. Therefore, we need larger device lengths so as to achieve a non-reciprocal phase shift difference of "π", which can be observed in Figure 5.4 (b).

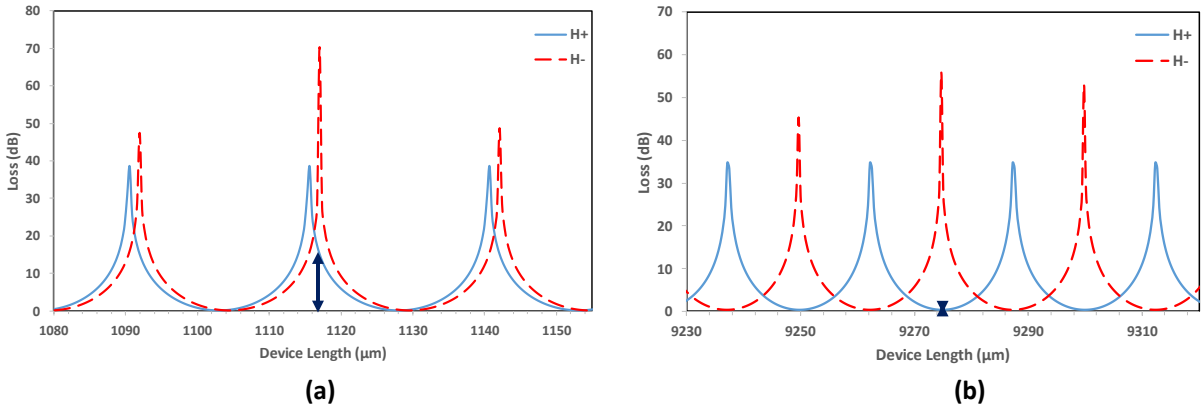

Figure 5.4 The isolation-insertion loss plot versus device length for the semiconductor optical waveguide isolator with thin Ce:YIG layers (a) Loss plot with device length of around 1 mm. (b) Loss plot with device length of around 9 mm

As Figure 5.4 (a) shows, the value of the insertion loss at the $1.117\ mm$ device length is $15.1\ dB$. This translates into the fact that smaller device lengths for the thin Ce:YIG layer integrated semiconductor waveguide isolators would be infeasible to use practically. However, in Figure 5.4 (b), the insertion loss at the $9.275\ mm$ device length is less than $0.5\ dB$, while both devices have the same isolation value of $55\ dB$. The relationship between the device length and the insertion loss can be seen in Table 5.3:

Table 5.3 The relationship between the insertion loss and device length of the proposed isolator

Device Length (mm)	Insertion Loss (dB)	Isolation (dB)
9.275	0.35	82.18
7.568	0.73	68.10
5.121	2.40	55.00
3.878	4.80	71.66
1.117	15.08	55.23

As seen in Table 5.3, insertion loss gets fairly large values when the device length is small due to the low values of $Im[\varepsilon_{xy}]$ for the Ce:YIG material. Even though large device lengths for optical isolators are not desired, an optimum selection should be done to decrease the theoretical insertion loss value.

5.4 Results and Discussion

Before starting to discuss the results for the optical isolator with thin Ce:YIG layers, we want to demonstrate the results for ferromagnetic elemental metal included isolators. Those metals are iron, cobalt and nickel. The reason to show them first is to exhibit their low efficiency to be used as part of the optical isolator. In contrast to those elemental metals, Ce:YIG and other magnetic garnets are better candidates for optical isolation purposes since they have large Faraday rotation angle and low absorption at the telecommunication wavelength, $1.55\ \mu m$.

5.4.1 Iron, Cobalt, and Nickel

The field and the loss profiles for the structures with iron, cobalt, and nickel will be shown and discussed in this section. In this structure with ferromagnetic metals, five InGaAsP quantum well structure is used as a waveguide, while one metal layer is used as a magneto-optic layer in between two thick silicon layers.

5.4.1.1 Field Profiles

In this section, the field profiles will be illustrated for various metals. The H_y field profiles for the TM_0 and TM_1 modes along the forward and backward directions can be seen in the next three figures. The relative refractive index profile is also added to show

the confinement of the modes along the x-axis. The field profile for iron can be seen in Figure 5.5. The refractive index for iron is ~3.63 which is the largest compared to other layers in the designed structure with iron. The discontinuities along the boundaries of the metal layer can be observed for all three metal designs mainly due to the thin metal layers.

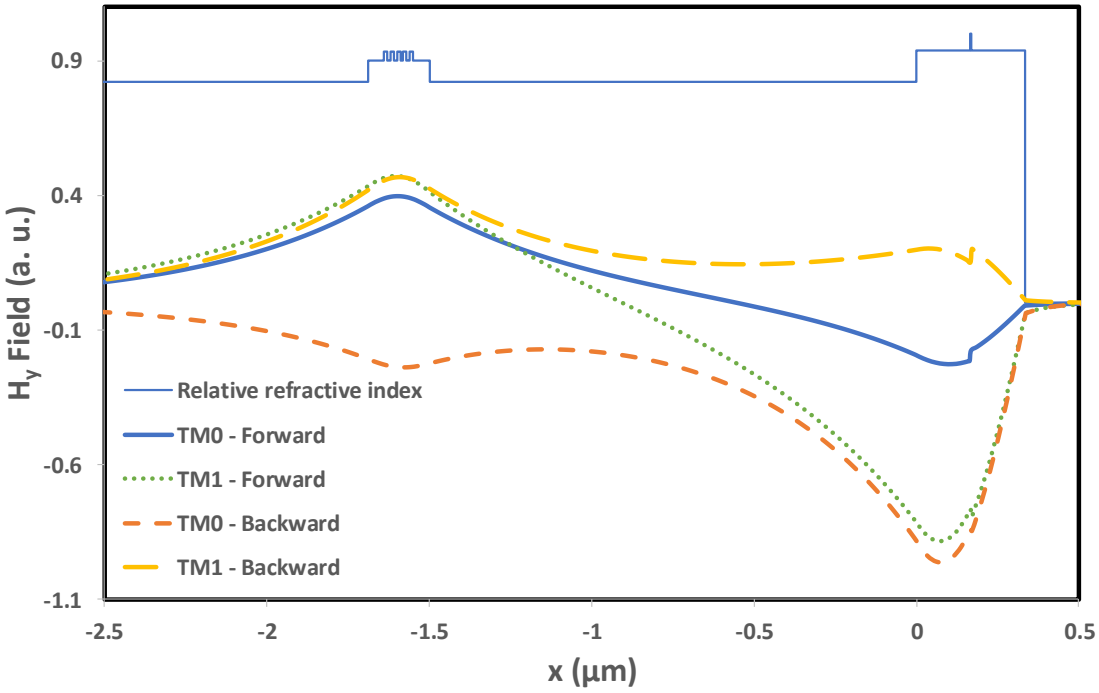

Figure 5.5: Hy field profile for the isolator with iron metal layer

The field profile for cobalt metal layer can be seen in Figure 5.6. The thickness value is 4 nm for all three metal layers and the thickness for the inner InP clad layer is 1500 nm. The refractive index for cobalt is the largest among all three metals which is ~5.62.

The differences between the TM_0 field profiles as well as TM_1 profiles along forward and backward directions can be observed. The reason for the difference is the large off-diagonal element for cobalt and iron.

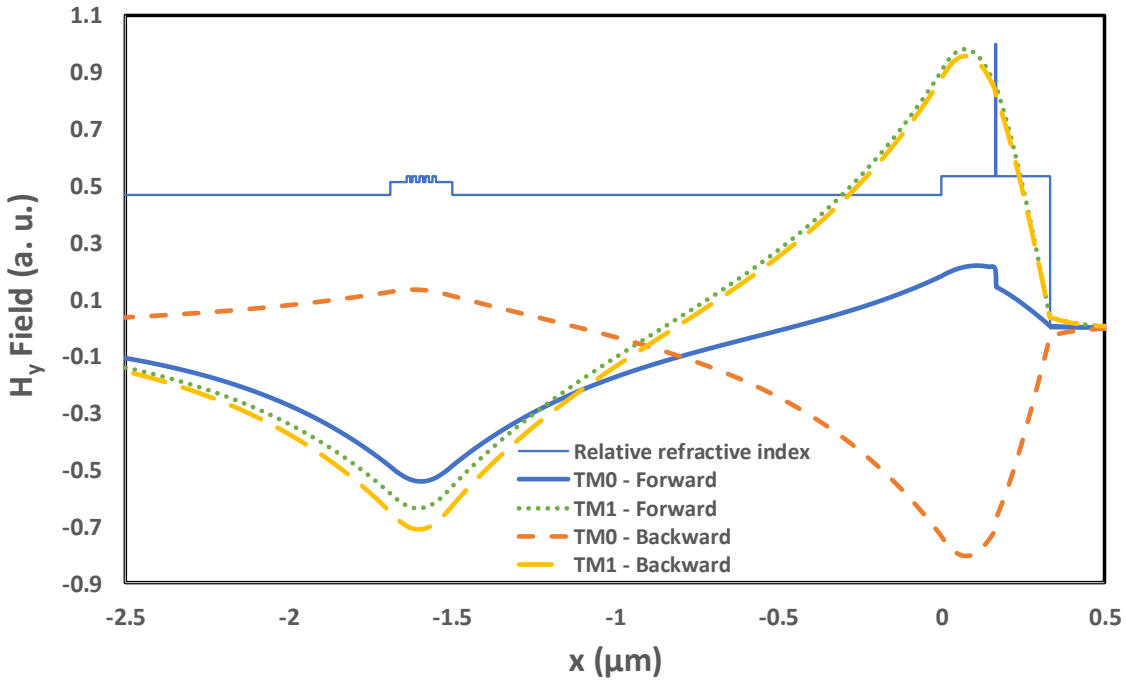

Figure 5.6 Hy field profile for the isolator with cobalt metal layer

The largest discontinuity among all metal structures is in Figure 5.6. The reason is the large magnitude of cobalt's refractive index. The field profile for nickel is shown in Figure 5.7. Nickel's comparably low refractive index can be seen which is ~3.38.

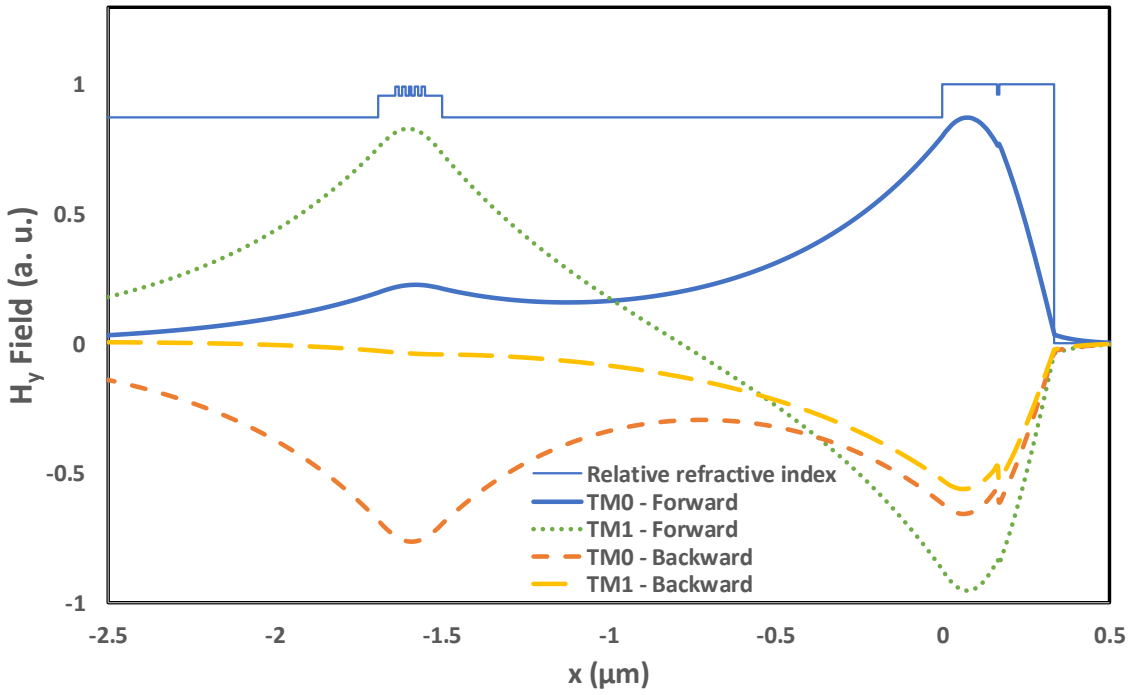

Figure 5.7 Hy field profile for the isolator with nickel metal layer

5.4.1.2 Loss Profiles

The comparative loss profiles for the isolator structures with three ferromagnetic metals along forward and backward directions will be shown and discussed in this section. In the loss profiles, H+ refers to the magnetic field along +y-direction, and H− refers to the magnetic field along −y-direction. In spite of the low imaginary parts of the off-diagonals for Ce:YIG, Iron has a quite large off-diagonal (i.e. $Im[\varepsilon_{xy}] = 1.82$ [86]), which helps have significant amount of isolation for lower device lengths, as seen in Figure 5.8. The

device length for the peak point in Figure 5.8 is 149.6 μm, and the isolation at that point is 27.08 dB. However, the amount of insertion loss is 23.05 dB at the same point. Even though Iron has a higher $Im[\varepsilon_{xy}]$ than Ce:YIG, which leads to satisfactory isolations in pretty small device lengths, it has a very large extinction coefficient, which keeps the insertion loss in the very high ranges as well.

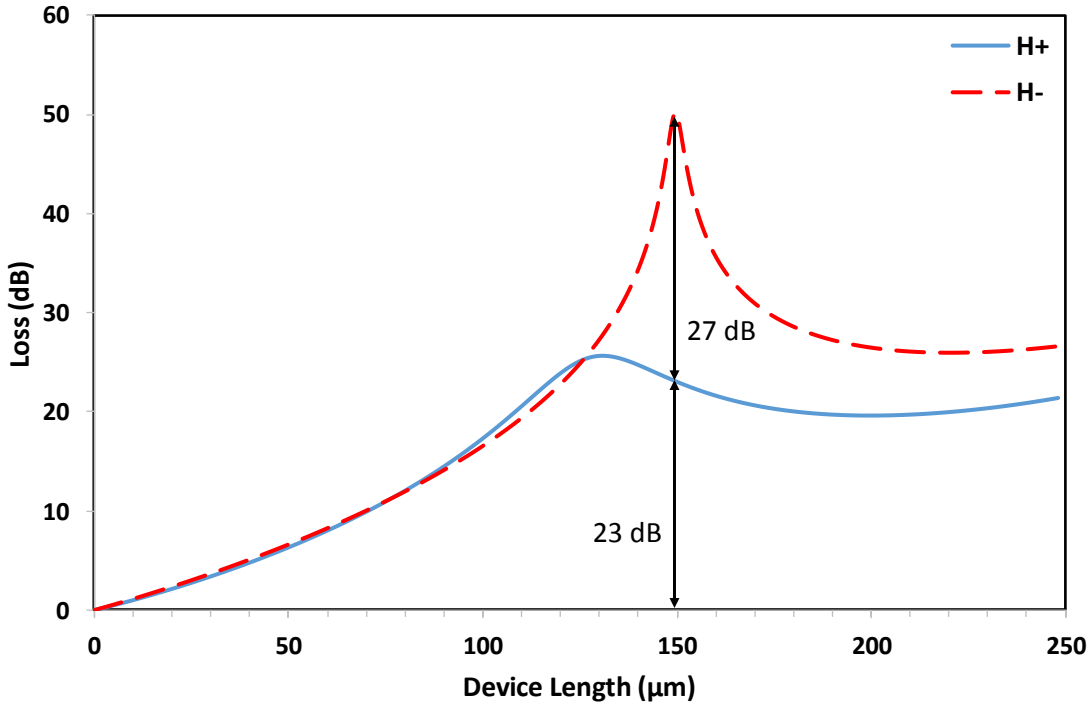

Figure 5.8 The loss profile of the isolator with Iron layer in terms of device length

Cobalt's imaginary part of the off-diagonal element is ~2.0 which is comparable to that of Iron [86]. The device length for the Cobalt-implemented isolator is $175.94\ \mu m$. The insertion loss is $31.56\ dB$. It is even larger for Cobalt since its extinction coefficient is 5.75, which is higher than that of Iron. The amount of isolation is $23.46\ dB$, which does not make Cobalt a better candidate for the purpose of optical isolators. The isolation-insertion loss graph in terms of device length can be seen in Figure 5.9.

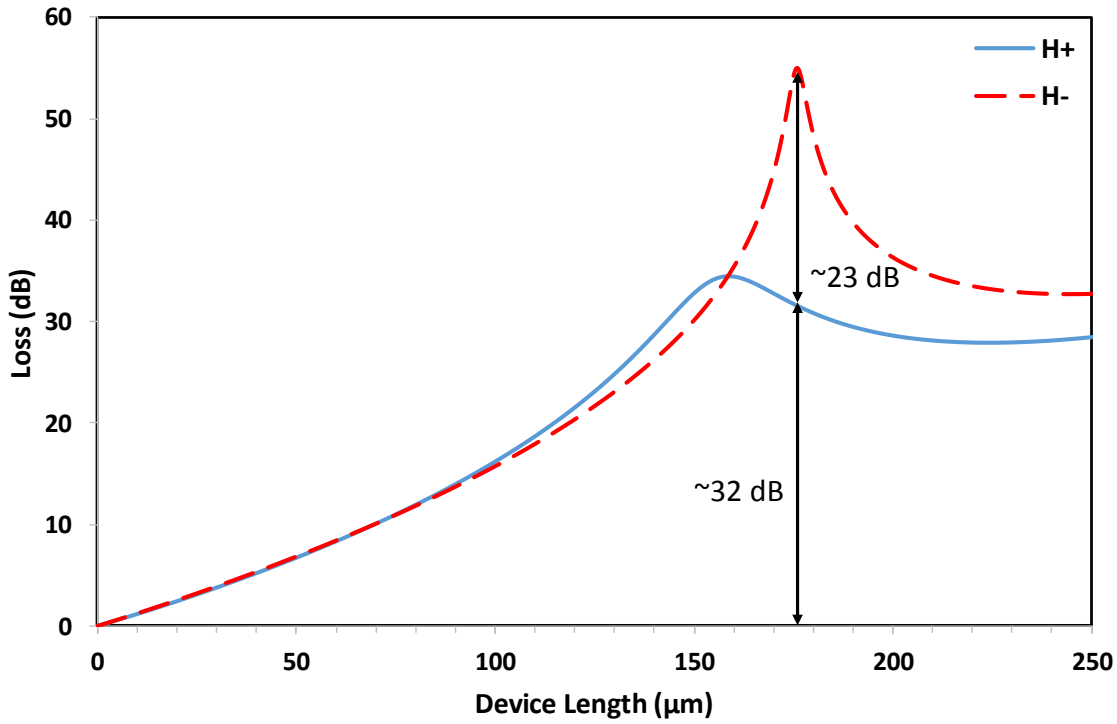

Figure 5.9: The loss profile for the Cobalt layer embedded isolator in terms of varying device length

To make a novel contribution to the optical isolator literature, we also investigated a Nickel-implemented device, which has a smaller $Im[\varepsilon_{xy}]$ with a value of 0.86 [86]. Due to this off-diagonal element, the peaks for forward and backward directions are quite close to each other, which makes the isolation smaller. The device length for the peak is 131.75 μm, while the isolation is 14.59 dB. Since Nickel's extinction coefficient is 6.82 which is the largest extinction coefficient of all the metals investigated in this chapter, its insertion loss in the peak for Figure 5.10 is also the largest, with a value of 37.02 dB.

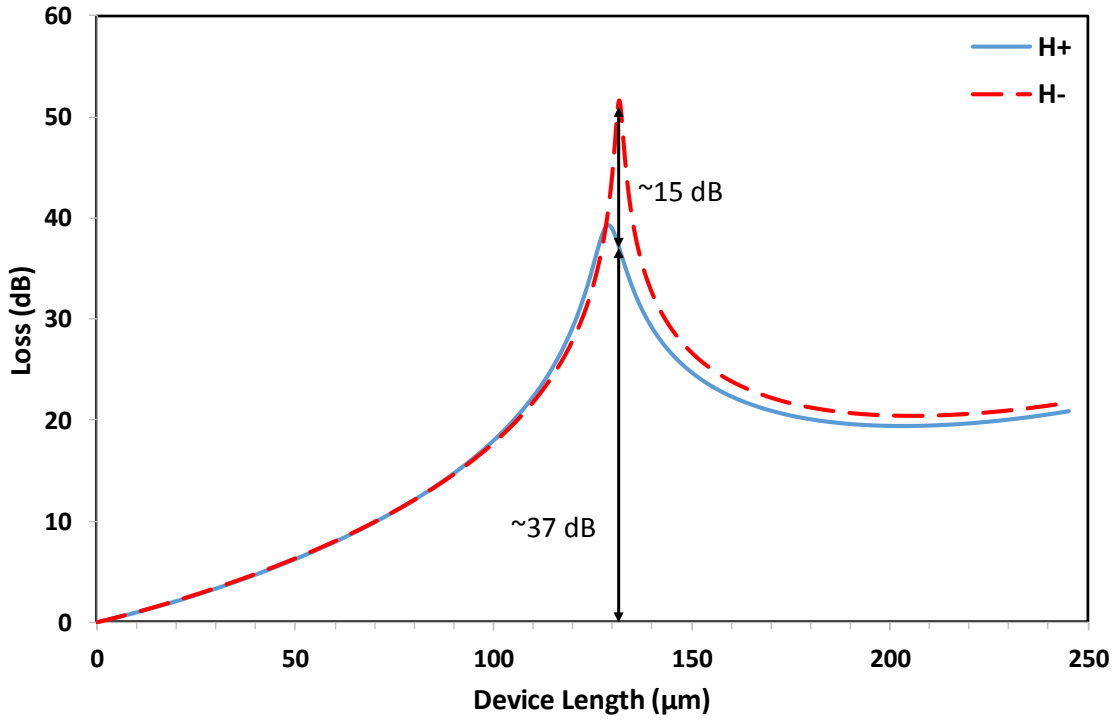

Figure 5.10 The loss profile for Nickel implemented isolator

Therefore, implementing the ferromagnetic common metals Fe, Co, and Ni even for tens of angstroms in optical waveguide isolators is not feasible because of the high loss that they bring to the system.

5.4.2 Ce-substituted YIG (Ce:YIG)

The field profile as well as the loss profile along the forward and backward directions for the isolator structure with Ce:YIG layers can be seen in this section. In contrast to the ferromagnetic metals in this work, yttrium iron garnets are better candidates for optical waveguide isolators because of their low loss and large Faraday rotation properties. For our proposed device, we utilize the extinction coefficient of 1.66×10^{-5} for Ce:YIG, while Faraday rotation angle is $-3300\ Deg/cm$ [95], [106]. Having a larger Faraday rotation angle is crucial in order to get a larger off-diagonal element.

$$\varepsilon_0 = \frac{2n\theta_F}{k_0} \tag{237}$$

where n is the refractive index of the material, θ_F is the Faraday rotation angle and k_0 is the wavenumber for the vacuum.

5.4.2.1 Field Profile

The field profile for the isolator structure with Ce:YIG material can be seen in Figure 5.11. The relative refractive index profile is also added to show the confinement of the modes among the layers. In this design, three quantum well InGaAsP laser structure is used as a waveguide layer. In the isolator region, there are two Ce:YIG layers which are stacked in between three thick silicon layers (~350 nm).

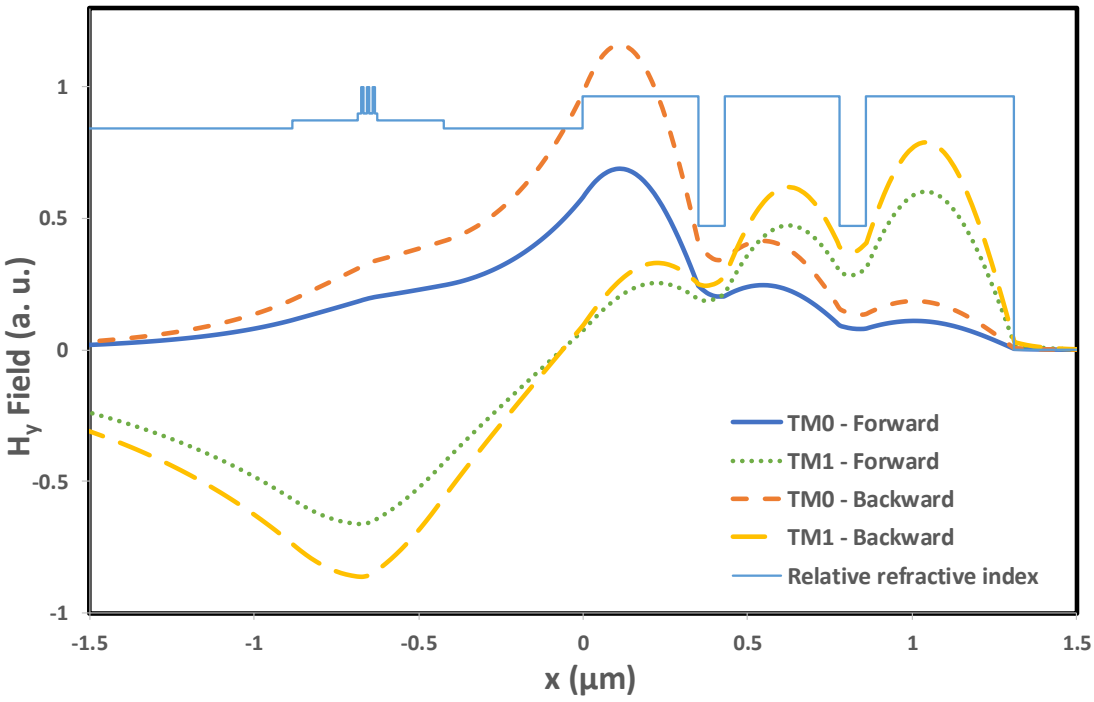

Figure 5.11 The field profile for the isolator design with Ce:YIG material.

As discussed in the previous sections, the overall refractive indices of each sub-waveguide should be comparable to each other in order to provide coupling between the two sub-waveguides. Therefore thick silicon layers are needed since the refractive index for Ce:YIG is low (~2.21). Although the off-diagonal element is small for Ce:YIG ($Im[\kappa_o] = 6.28 \times 10^{-3}$), the differences between the TM_0 field profiles as well as TM_1 profiles along forward and backward directions can still be observed. In contrast to the field profiles of structures with metal layers, there are no field discontinuities for structures with Ce:YIG material mainly because of the thick Ce:YIG layers compared to the very thin ferromagnetic metal layers.

5.4.2.2 Loss Profile

The loss profile for the Ce:YIG-implemented isolator appears in Figure 5.12. Optical isolation is realized at resonance wavelength value of around $1.54\ \mu m$ as Figure 5.12 shows. The device length is $5.12\ mm$. The reason for the large footprint is the small imaginary part of the off-diagonal for Ce:YIG with a value of 6.28×10^{-3}. As Table 5.1 shows, the isolation ratio at that device length is $55\ dB$, while the overall insertion loss is $2.4\ dB$, which translates into $0.47\ dB/mm$.

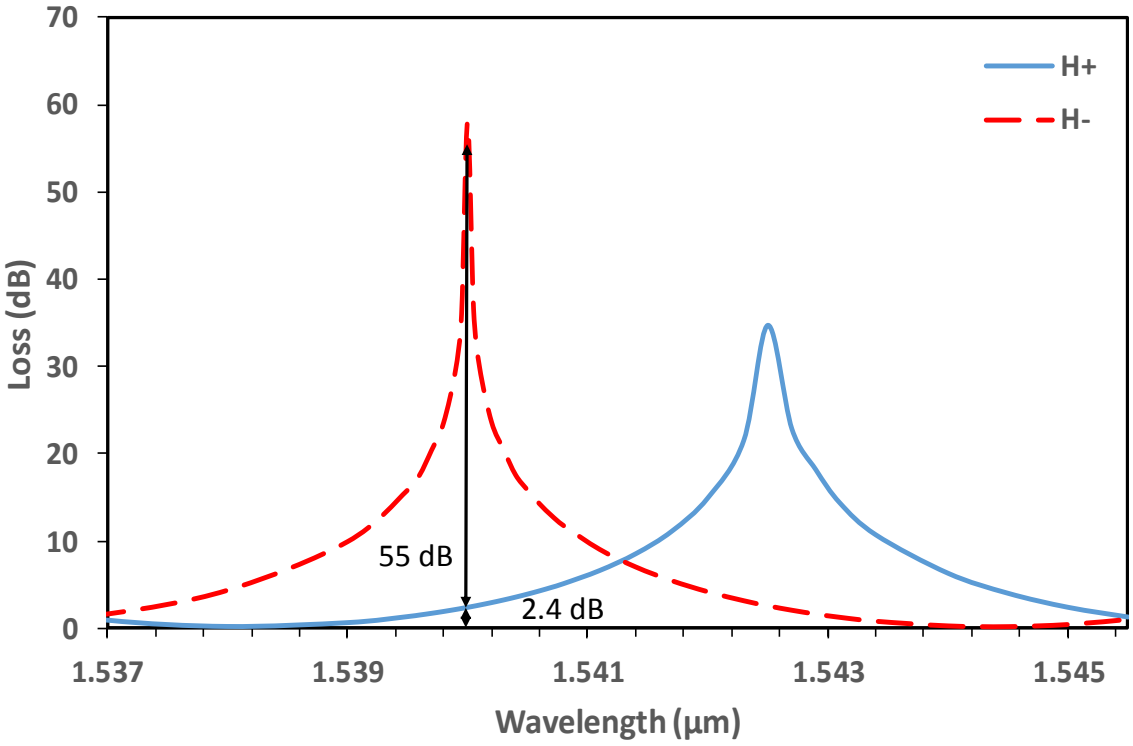

Figure 5.12 Isolation profile for the device length 5.12 mm, while the peak wavelength is 1.54 µm.

In order to provide a sensitivity check for our design, the refractive indices of each QW layers are changed on the order of ± 0.001. In Figure 5.13, backward propagation -as depicted by the solid line- represents the isolation, while forward propagation is illustrated with the dashed line. In Figure 5.12, and Figure 5.13, the device length is fixed at $5.12\ mm$ and the wavelength is changed in order to show the isolation behavior along the frequency space. The condition $\Delta n = 0$ refers to the original device as shown in Figure 5.12. When

the QW index is increased on the order of 0.001, the resonance wavelength shifts to 1.5396 μm, while the insertion loss is 2.23 dB, which is smaller than the initial $\Delta n = 0$ case. At that point, an isolation value of 33 dB can be obtained.

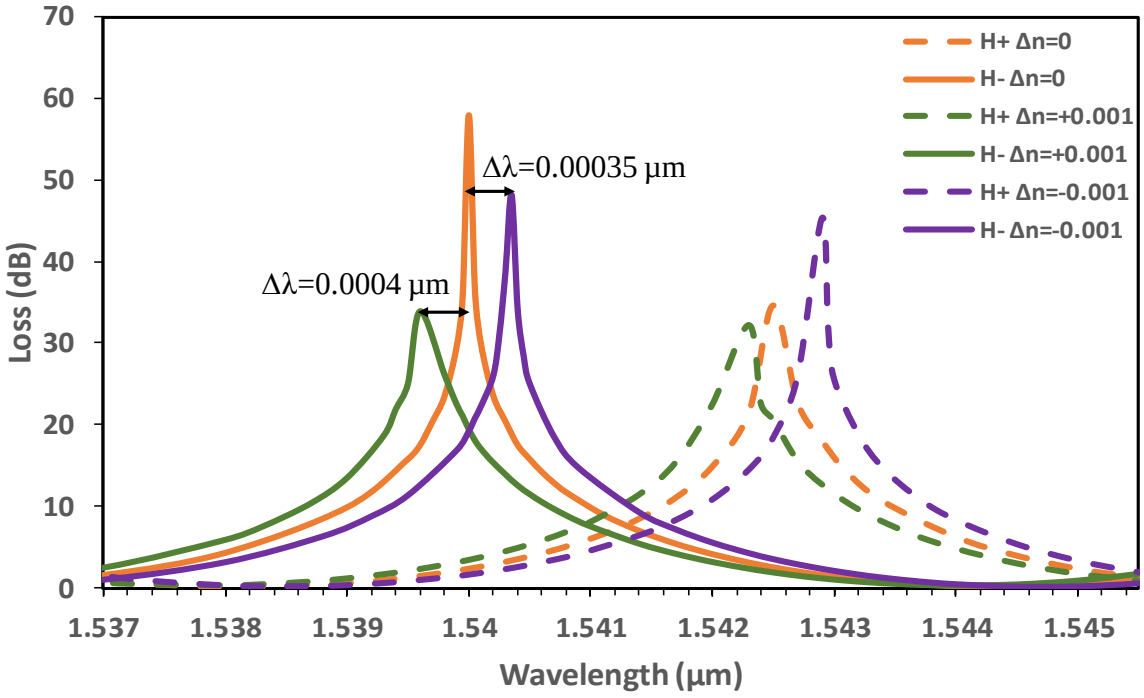

Figure 5.13 Sensitivity check of the design by changing the refractive indices of the QW laser's layers. Solid lines represent backward propagation while dashed lines are for forward propagation.

If the index is decreased at the same amount, the resonance is shifted to 1.54035 μm where the isolation is 48 dB. At that point, insertion loss is also in the same range as in the original case; that is, 2.44 dB. The sensitivity analysis demonstrates that our device provides high

isolation ratios even though there might be some potential errors in manufacturing the device or due to the external environmental factors. Even if such issues are considered, Figure 5.13 shows that the proposed device is very robust.

Up until now, Ce-substituted YIG material has been utilized in interferometric isolators which are designed to be passive devices. In those passive interferometric devices, laser light is sent through the input region of the isolator externally. However, monolithic integration of the optical isolators with laser diodes are crucial for the sake of future integrated optoelectronics. The current study is aimed at bridging this gap and hence proposes and analyzes the first monolithically integrated semiconductor active waveguide optical isolator with thin Ce:YIG layer. An InGaAsP/InP multiple quantum well laser is used as a SOA layer. Unlike the conventional SOA-type isolators, our device does not utilize its SOA gain as a compensation tool for forward loss, since it already has only a small amount of forward loss around $0.47\ dB/mm$. The attained isolation ratio is $55\ dB$. After conducting a sensitivity check for our system by changing the QW refractive index on the order of ± 0.001, we observed that our device does not strictly depend on waveguide parameters, which makes it easy to fabricate. With the goal of presenting a comparative study of Ce:YIG-based and ferromagnetic metal-based (i.e. Fe, Co, and Ni) SOA-type isolators, we also show the corresponding loss plots of each isolator type. Since they have large magneto-optic effects, they provide a high amount of isolation ratios. However, the

insertion loss that they bring to the system is not smaller than $23\ dB$, which renders them unsuitable candidates for use in optical isolators.

CHAPTER 6

6 CONCLUSION AND FUTURE WORK

In this dissertation, the semiconductor active waveguide optical isolators are proposed as a combination of various ferromagnetic metals (i.e. Fe, Co, Ni) one at a time and a ferrimagnetic garnet (i.e. Cerium-substituted Yttrium Iron Garnet (Ce:YIG)). In our monolithically integrated isolator the optical gain is not used as a compensation mechanism for the forward loss. In the design of the structures, two sub-waveguides are monolithically integrated to each other: One is a tunable multi-quantum well (MQW) InGaAsP/InP laser operating at $1.55\ \mu m$ telecommunication wavelength, and the other one is the isolator region which is a combination of alternating layers of the magneto-optic material and silicon.

6.1 Conclusion

A magnetic field (B_y) is applied along the $\hat{y}$ −direction, which is then reversed to simulate the forward and backward lights. The coupling of the two main sub-waveguides is the fundamental feature of this optical waveguide isolator. When the laser light enters the isolator section, the two isolator modes are excited. The power can be distributed in between the MQW and isolator regions by the help of coupling of the two layers. Another

critical component of this design is the alternating layer structure. It paves the way to assign high-indexed ferromagnetic metals in between thick Si layers in an alternating fashion (one layer silicon, one layer metal, and one layer silicon again and so on). This is conducted as such so as to achieve the coupling mechanism between the isolator and the MQW laser structure. As for the case of ferrimagnetic Ce:YIG, the refractive index is as low as 2.21, whereas the refractive index for laser is ~3.26. Considering that, it would be wiser to stack thin Ce:YIG layers in between the thick Si layers. This helps adjust the overall average refractive index of the isolator region. Alternating layers of magneto-optic material and silicon can be deposited above the QW laser.

In the proposed device, the backward light is primarily confined to the isolator region with the optimization of waveguide parameters. ISOLATOR software is devised to analyze the loss configurations along the forward and backward directions by iteratively changing the silicon layer thickness. Through this iterative process, we select the iteration point at which the backward loss is at its maximum. At this highest backward loss point, the intensity is primarily confined in the lossy magneto-optic layer instead of the MQW layer, which is the key principle of the proposed isolator in this work. The forward loss is different than the backward loss due to the non-reciprocity in magnetically biased magneto-optical devices along the + and – directions of the propagation. Therefore, our devices do not need to use the optical gain as a compensation tool for the forward loss in contrast to some of the active waveguide isolators in the literature [13], [84], [100].

Optical characterization of iron has been studied for the purpose of waveguide optical isolators. First of all, the Drude Free Electron Theory is used to model the susceptibility of iron. The large discrepancies in between the experimental data and the Drude model show that Drude model cannot characterize the behavior of all electrons in an atom. An extension of this model, referred to as the Lorentz-Drude (LD) model, is more reasonable to use for the near-IR and visible ranges of the spectrum since it includes bound electron effects. However, the Lorentzian line-shape has wider wings compared to the Gaussian line shape. This directs us to use the convolution of Lorentzian and Gaussian profiles, which is called Voigt line-shape. Brendel and Bormann (BB) described this model solely for the amorphous solids in the IR region [35], but seven years later, Rakic *et al.* showed that the same model is applicable to various kinds of materials containing metals in any regions up to 6 eV [42].

In this current study, the Rakic's BB model is improved by reducing the number of unknowns and relaxing a constraint from the system [42]. Since Rakic *et al.* did not apply their model to iron, we select an element that they analyzed (i.e. gold) to compare our model against theirs. The gold data is obtained from Lynch *et al.* [62]. For the first two interband transitions, which are at $\sim 1.9\, eV$ and $\sim 2.45\, eV$, the improved model fits accurately. Therefore, it can be claimed that our model for gold is compatible to Rakic et al.'s up to the energies of $4\ eV$. It provides better accuracy than Rakic et al.'s at the energies larger than $4\ eV$. This study presents uniqueness in that the improved BB model is applied

to the iron metal by using the data from Weaver *et al* [44]-[45]. Figure 2.3 shows that our model is a perfect fit for iron up to $30\ eV$.

In order to present and lay out the physical theory behind the optical waveguide isolators, the magneto-optic effects −primarily the Faraday Effect and the Magneto-optic Kerr Effect (MOKE)− have been introduced. For the case of Faraday Effect, the polarization plane of light is rotated upon emission through a magnetic material, when there is an applied magnetic field. For the MOKE, the polarization plane of light is rotated after reflection from a magnetic material. These polarization plane rotations are attributed to the change of refractive indices for the "right circularly-" and "left circularly-polarized" light components under an applied magnetic field, of which phenomenon is called Zeeman Effect. Therefore, it is inferred that all magneto-optic effects are based on the Zeeman Effect, which is basically the splitting of the spectral lines into a number of components under the influence of an applied magnetic field.

The theory of the optical waveguide isolators is presented in Chapter 4. The solutions of Maxwell Equations for the TE and TM mode are shown when the applied magnetic field is along the $\hat{y}$ −direction. It is demonstrated that the TE mode does not have any anisotropic property, which is important for the waveguide isolators. However, the TM mode has an anisotropic behavior; therefore, it is selected as an operating mode for our devices. The optical isolators with iron layers are also presented. Iron metal layers are included into the isolator region alternatingly with silicon. The enhancement in the

insertion loss after decreasing the number of iron layers can be observed. The insertion loss value is $33\ dB$ when the numbers of iron layers is four (with a total thickness of $4\ nm$ in total). However, it is $23\ dB$ if the layer number is decreased from four to one, keeping the same iron thickness at $4\ nm$. These results justify the practicality and the flexibility of the alternating layer structure for the waveguide optical isolators.

Out of all the ferromagnetic layer based isolators in this work, iron is the one that has the lowest insertion loss compared to the others. The rationale behind is that the amount of extinction coefficient for iron is 5.6, which is fairly large [90]. However, compared to cobalt and nickel, this value is still small. Cobalt's extinction coefficient is 5.75, while nickel's is 6.82 [90]. In the ferromagnetic layer embedded isolators, there is one ferromagnetic layer and two silicon layers. The thicknesses of each of the silicon layers are iteratively changed from $\sim 155\ nm$ to $\sim 180\ nm$, and the thickness of each of the ferromagnetic layers is $4\ nm$. For iron, the device length is $149.6\ \mu m$. The isolation ratio for that is $27.08\ dB$, while the insertion loss is $23.05\ dB$. For the case of cobalt, the isolation is $23.46\ dB$, and the insertion loss is $31.56\ dB$, at the device length of $175.94\ \mu m$. Since nickel has the biggest extinction coefficient out of all the abovementioned ferromagnetic metals, its insertion loss is the highest at the value of $37.02\ dB$. The isolation for nickel is $14.59\ dB$, while the device length is $131.75\ \mu m$. Imaginary part of the off-diagonal dielectric constant is one of the most important features

to have large amount of isolations. This can be seen in the Table 6.1 for the abovementioned ferromagnetic metals.

Table 6.1 The magneto-optical properties of ferromagnetic metals [86], [90] and the insertion loss/isolation results.

	$Im[\varepsilon_{xy}]$	**Extinction Coefficient, k**	**Insertion Loss**	**Isolation**
Iron	1.82	5.6	23.05 dB	27.08 dB
Cobalt	2.00	5.75	31.56 dB	23.46 dB
Nickel	0.86	6.82	37.02 dB	14.59 dB

For iron, the isolation value is the highest among all listed metals since it has the largest $Im[\varepsilon_{xy}]$ of 1.82 [86]. As for the nickel, the isolation is the smallest because of its $Im[\varepsilon_{xy}]$ being equal to 0.86 [86]. From all the results above, we can infer that the ferromagnetic metals are not the best candidates for designing optical waveguide isolators as they have substantial amounts of insertion losses.

In contrast to the ferromagnetic elemental metals in this work, yttrium iron garnets are better candidates for optical waveguide isolators due to their low loss and large Faraday rotation properties. For our proposed device, we utilize the extinction coefficient of 1.66×10^{-5} for the Ce:YIG, and the Faraday rotation angle of $-3300\ Deg/cm$ [95],

[106]. The device shows promising results with an isolation ratio of $55\ dB$ at a wavelength of $1.54\ \mu m$. The reason for that is the high Faraday rotation values of magnetic garnets. Unfortunately, Ce:YIG has quite low $Im[\varepsilon_{xy}]$, which is 6.28×10^{-3}, in contrast to the aforementioned ferromagnetic metals. Therefore, larger device lengths are needed to achieve satisfying amounts of isolation. For our case, the device length is reported as $5.12\ mm$. The Ce:YIG layer implemented isolator provides favorably small insertion loss of $2.4\ dB$, which in other words is equal to $0.47\ dB/mm$ per length of unit.

As for the Ce:YIG case, we report a sensitivity check in order to validate the reliability of the isolator. The amounts of refractive indices of the QW layers are changed at the range of ± 0.001. Corresponding results of this alteration can be seen in Table 6.2.

Table 6.2 The results of the sensitivity check for the Ce:YIG implemented waveguide isolator.

	Resonance Wavelength (μm)	**Isolation Ratio**	**Insertion Loss**
$\Delta n = 0$	$1.54\ \mu m$	$55\ dB$	$2.4\ dB$
$\Delta n = +0.001$	$1.5396\ \mu m$	$33\ dB$	$2.23\ dB$
$\Delta n = -0.001$	$1.54035\ \mu m$	$48\ dB$	$2.44\ dB$

In Table 6.2, it can be understood that the proposed device is robust within the possible range of errors stemming from the other devices such as semiconductor lasers. Therefore,

it can confidently be claimed that this model is practical to apply in the field of opto-electronics. The only drawback that is observed would be the device length of the isolator. This can be further analyzed to decrease the device lengths of Ce:YIG-implemented isolators.

6.2 Future Work

The structure with Ce:YIG layers yield promising results in terms of low insertion loss and high isolation ratios. Yet, that structure has a high device footprint mainly due to the low off-diagonal element of the Ce:YIG material. Therefore, it is crucial to further optimize the isolator design in order to minimize the device length.

On the other hand, magnetic garnet materials have recently emerged to be important in the nonreciprocal devices due to their large magneto-optic effect. To the best of our knowledge, Ce:YIG material is one of the best garnets in the state-of-art. However, it still has low off-diagonal element values, which is the reason for having relatively large device lengths. It would be a viable option to search for other feasible materials for the same purpose. Determining the material parameters is also an important step for theoretical research.

As the third component of potential future work, it would be critical add-on to literature to validate the theory with the experimental work. We are aimed at fabricating

these theoretically designed structures and test their isolator properties for having a low-loss on-chip semiconductor optical isolator.

7 APPENDIX

7.1 Appendix 1

As shown in Eq. (54), the expectation value of the diagonal susceptibility depends on $\langle 1/\widetilde{\Omega}_j \rangle$ and considering the complex normalized frequency in Eq. (24), the diagonal susceptibility can be defined as follows:

$$\langle \frac{1}{\widetilde{\Omega}_j} \rangle = \langle \frac{1}{1 - \overline{\Omega}_j^2 - j\Gamma_j} \rangle \tag{238}$$

while the random variable is $\overline{\Omega}_j = \overline{\omega}_j/\omega$ and the normalized collision frequency is $\Gamma_j = \gamma_j/\omega$. The integral form is shown in Eq. (239):

$$I(a_j) = \langle \frac{1}{a_j^2 - \overline{\Omega}_j^2} \rangle = \frac{1}{\sqrt{2\pi}\sigma_j} \int_{-\infty}^{+\infty} \frac{1}{a_j^2 - \overline{\Omega}_j^2} e^{-\frac{(\overline{\omega}_j - \omega_j)^2}{2\sigma_j^2}} d\overline{\omega}_j \tag{239}$$

where $a_j^2 = 1 - j\Gamma_j$. If the nominator and the denominator in the exponent are multiplied with $1/\omega^2$, as well as the nominator and the denominator of the integrand itself with $1/\omega$, the integral equation would be as follows:

$$I(a_j) = \frac{1}{\sqrt{2\pi}S_j} \int_{-\infty}^{+\infty} \frac{1}{a_j^2 - \bar{\Omega}_j^2} e^{-\frac{(\bar{\Omega}_j - \Omega_j)^2}{2S_j^2}} d\bar{\Omega}_j \tag{240}$$

$S_j = \sigma_j/\omega$ in Eq. (240) is the variance of the random variable $\bar{\Omega}_j$. As shown in Rakic *et al.* [42] $I(a_j)$ can be defined as a summation of two integrals:

$$\frac{1}{a_j^2 - \bar{\Omega}_j^2} = \frac{1}{2a_j}\left(\frac{1}{a_j - \bar{\Omega}_j} + \frac{1}{a_j + \bar{\Omega}_j}\right) \tag{241}$$

with the condition of $Im[a_j] > 0$. Therefore, the first term can be written as:

$$I_1 = \frac{1}{2\sqrt{2\pi}a_j S_j} \int_{-\infty}^{+\infty} \frac{1}{(a_j - \omega_j) - (\bar{\Omega}_j - \omega_j)} e^{-\frac{(\bar{\Omega}_j - \Omega_j)^2}{2S_j^2}} d\bar{\Omega}_j \tag{242}$$

Considering relations (7.1.3) and (7.1.4) in Handbook of Mathematical Functions [67], we could define $t = (\bar{\Omega}_j - \Omega_j)/(\sqrt{2}S_j)$ and $z_1 = (a_j - \omega_j)/(\sqrt{2}S_j)$ that helps to rewrite Eq. (242) as in Eq. (243):

$$\begin{aligned} I_1 &= \frac{1}{2\sqrt{2\pi}a_j S_j} \int_{-\infty}^{+\infty} \frac{e^{-t^2}}{z_1 - t} dt = -j\frac{\sqrt{\pi}}{2\sqrt{2}a_j S_j} e^{-{z_1}^2} erfc(-jz_1) \\ &= -j\sqrt{\frac{\pi}{2}}\frac{1}{2a_j S_j} w(z_1) \end{aligned} \tag{243}$$

The second integration can be defined as:

$$I_2 = \frac{1}{2\sqrt{2\pi}a_j S_j} \int_{-\infty}^{+\infty} \frac{1}{(a_j + \omega_j) + (\bar{\Omega}_j - \omega_j)} e^{-\frac{(\bar{\Omega}_j - \Omega_j)^2}{2S_j^2}} d\bar{\Omega}_j \tag{244}$$

If we define $z_2 = (a_j + \omega_j)/(\sqrt{2}S_j)$ the result of the second integration would be as follows:

$$I_2 = -j\sqrt{\frac{\pi}{2}} \frac{1}{2a_j S_j} w(z_2) \tag{245}$$

The equations of $w(z_1)$ and $w(z_2)$ is calculated by the NAG library, S15DDF function.

7.2 Appendix 2

The secular equations Eq. (144) and Eq. (165) with γ −dependency can be represented as follows:

$$A(\gamma)q(\gamma) = 0 \tag{246}$$

This equation is to be solved iteratively by the help of ARPACK routine. Eq. (246) is a form of an eigenvalue equation, which satisfies $(\boldsymbol{A}'(\boldsymbol{\gamma}) - \lambda \boldsymbol{I})q(\gamma) = 0$ while $\boldsymbol{A}'(\boldsymbol{\gamma}) = A(\gamma) + \lambda \boldsymbol{I}$. One can infer that $A(\gamma)$ should be singular (i.e. $det(\boldsymbol{A}'(\boldsymbol{\gamma}) - \lambda \boldsymbol{I}) = 0$) in order to get nontrivial solutions for $q(\gamma)$ eigenvectors. The system is aimed at finding the values of γ which makes $A(\gamma)$ singular. If $\gamma = \gamma_a$ makes $A(\gamma)$ singular, then $q(\gamma_a)$ would be the nontrivial solution vector, which has at least one of its eigenvalues equal to zero. Let us assume a random value of γ which does not make $A(\gamma)$ singular, hence $A(\gamma)$ cannot depict $q(\gamma)$. However, $A(\gamma)$ can depict $q(\gamma)$, if the eigenvector with the smallest eigenvalue can be determined. We can tabulate the structure that we use in the program as follows:

$\gamma = \gamma_a$	$A(\gamma)$ singular	$One\ of\ its\ eigenvalues = 0$
$\gamma \neq \gamma_a$	$A(\gamma)$ nonsingular	$One\ of\ its\ eigenvalues \ll 1$

Our way of using Newton's iterative method tracks the condition nature of matrix, which is to quantify the sensitivity of the system with respect to changes in the coefficients. The formula for condition number is defined as in Eq. (247):

$$cond(\boldsymbol{A}) = \|\boldsymbol{A}\|\left\|\boldsymbol{A}^{-1}\right\| \tag{247}$$

In Eq. (247), $\|\boldsymbol{A}\|$ is the norm of the matrix $\boldsymbol{A}$, which is defined as the maximum of the summation of each matrix column as

$$\|\boldsymbol{A}\| = \max_{1\le j\le n}\sum_{i=1}^{n}\left|a_{ij}\right| \tag{248}$$

If the condition number is large, the system is named as ill-conditioned. Therefore, the condition number to enhance the accuracy of the solution should be minimized. If the condition number reaches the value of $\sim 10^{-14}$, the iteration would stop and calculate the effective index of the model [91]. Let us pick a random value as $\gamma = \gamma_0$, which is close to γ_a (but not equal). Matrix $\boldsymbol{A}$ is nonsingular and the Newton-type iteration follows the path according to the first order expansion of Eq. (249):

$$A(\gamma)q(\gamma) = A(\gamma_0)q(\gamma_0) + q(\gamma_0)\delta\gamma\left(\frac{\partial A}{\partial\gamma}\right)\Big|_{\gamma=\gamma_0} + A(\gamma_0)\delta\gamma\left(\frac{\partial q}{\partial\gamma}\right)\Big|_{\gamma=\gamma_0} = 0 \tag{249}$$

By assigning $\delta\gamma = \gamma - \gamma_0$ a small value, singularity would be closely realized. To further simplify Eq. (249), we could use Eq. (250) and Eq. (251):

$$A_0 = A(\gamma_0), \qquad A_\gamma = \left(\frac{\partial A}{\partial \gamma}\right)\Big|_{\gamma=\gamma_0} \tag{250}$$

$$q_0 = q(\gamma_0), \qquad q_\gamma = \left(\frac{\partial q}{\partial \gamma}\right)\Big|_{\gamma=\gamma_0} \tag{251}$$

Hence, the simplified version of Eq. (249) would be as follows:

$$A(\gamma)q(\gamma) = 0 = A_0 q_0 + q_0 \delta\gamma A_\gamma + A_0 \delta\gamma q_\gamma \tag{252}$$

Since an explicit dependency of eigenvector q with respect to γ does not exist, the values of q_γ cannot be obtained. Therefore, the third term in the right-hand side of Eq. (252) can be omitted as shown in Eq. (253):

$$A_0 q_0 + q_0 \delta\gamma A_\gamma = 0 \tag{253}$$

Since we assumed that A_0 is nonsingular and in turn it has an inverse, Eq. (253) should be multiplied by ${A_0}^{-1}$ as follows:

$$q_0 + {A_0}^{-1} q_0 \delta\gamma A_\gamma = 0 \tag{254}$$

$${A_0}^{-1} A_\gamma q_0 = -\left(\frac{1}{\delta\gamma}\right) q_0 \tag{255}$$

The eigenvalue of matrix ${A_0}^{-1} A_\gamma$ could be determined as shown in Eq. (256):

$$\lambda = -(1/\delta\gamma) \tag{256}$$

$\delta\gamma$ needs to be minimized to get the matrix close to singularity. Therefore, λ will be maximized i.e. $\lambda = \lambda_{max} = -(1/\delta\gamma)$.

In summation, we want to determine the smallest eigenvalue to have close proximity to singularity (since at least one of the eigenvalues of singular matrices is zero), but ARPACK always finds the largest eigenvalue. Therefore, we decided to find the largest eigenvalue of another term, i.e. ${A_0}^{-1}A_\gamma$. By the help of this, the eigen-functions of matrix $\boldsymbol{A}$ and the propagation constants for each mode could be identified.

7.3 Appendix 3

The effect of the off-diagonal term on the propagation constant can be found by the first order perturbation of the matrix $\boldsymbol{A}$ from the equations Eq. (144) and Eq. (165). The first order expansion of these equations can be represented as

$$(A_0 + A_1\varrho)(q_0 + q_1\varrho) = 0 \tag{257}$$

while ϱ is an off-diagonal element and it is defined as κ_0/κ_v. The other terms in Eq. (257) can be illustrated as follows:

$$A_0 = A(\gamma_a)_{\varrho=0} \qquad q_0 = q(\gamma_a)_{\varrho=0} \tag{258}$$

$$A_1 = \left(\frac{dA(\gamma_a)}{d\varrho}\right)_{\varrho=0} \qquad q_1 = \left(\frac{dq(\gamma_a)}{d\varrho}\right)_{\varrho=0} \tag{259}$$

We could state that the solution can be shown as in Eq. (260) when $\varrho = 0$, namely there is no magnetic bias:

$$A_0(\gamma_a)q_0(\gamma_a) = 0 \tag{260}$$

The open form of the first order expansion in Eq. (257) can be seen in Eq. (261):

$$A_0 q_0 + \frac{dA}{d\varrho} q_0 \varrho + A_0 \frac{dq}{d\varrho} \varrho = 0 \tag{261}$$

Eq. (260) shows that multiplying A_0 by the right eigenvector q_0 would result in zero. If we multiply the same matrix from the left hand-side by the transpose-conjugate of the left eigenvector, it would again give zero as shown in Eq. (262):

$$({q_0}^L)^\dagger A_0 = 0 \tag{262}$$

The transpose of the complex conjugate of a vector can be demonstrated by a symbol of " † " as a superscript. Considering Eq. (262), if Eq. (261) is multiplied by $({q_0}^L)^\dagger$ from the left hand-side of the equation, the relation in Eq. (263) is

$$({q_0}^L)^\dagger \frac{dA}{d\varrho} q_0 = 0 \tag{263}$$

The total derivative of matrix A with respect to ϱ is illustrated as

$$A_1 = \left(\frac{dA}{d\varrho}\right)_{\varrho=0} = \left(\frac{\partial A}{\partial \varrho}\right)_{\varrho=0} + \left(\frac{\partial A}{\partial \gamma}\frac{\partial \gamma}{\partial \varrho}\right)_{\varrho=0} \tag{264}$$

When the total derivative equation is plugged into the Eq. (263), the equation for the first order perturbation (stemming from the off-diagonal element i.e. ϱ) on the propagation constant, γ, would be received as

$$\frac{\partial \gamma}{\partial \varrho} = -\frac{({q_0}^L)^\dagger \left(\frac{dA}{d\varrho}\right)_{\varrho=0} q_0}{({q_0}^L)^\dagger \left(\frac{dA}{d\gamma}\right)_{\varrho=0} q_0} \qquad (265).$$

7.4 Appendix 4

The details of proposed methodology are explained earlier in Section 5.3.1. The following figure outlines the steps of how the optical isolator is designed in this study. If the material used for magneto-optic region is desired to be changed, the entire process can be rerun starting with the initial step of the generic methodology. On the other hand, if the number of magneto-optic layers is needed to be altered for a given material, only the ISOLATOR software is to be rerun and the corresponding parameters are to be optimized.

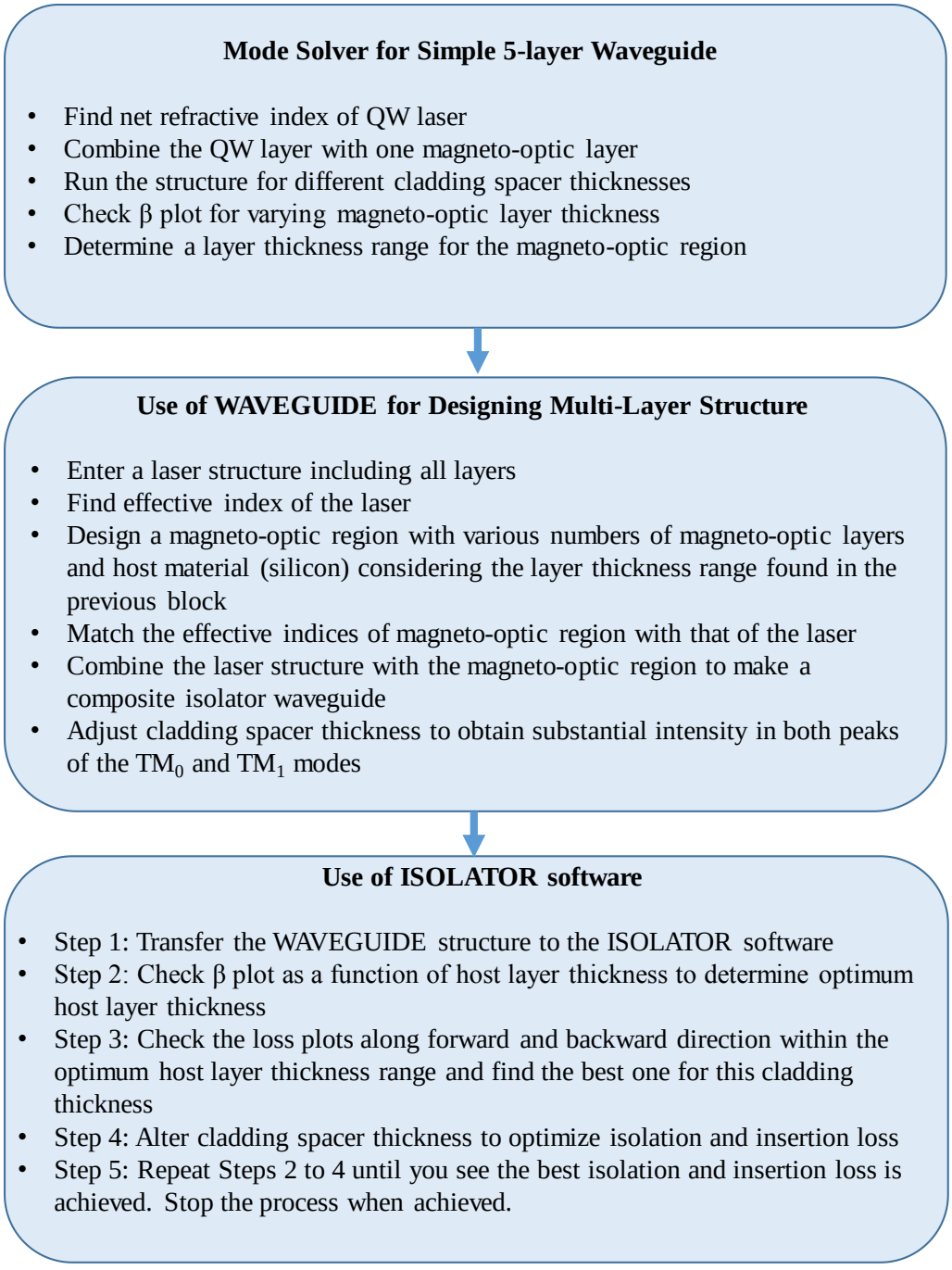

Figure 7.1 Proposed methodology for the isolator design

8 BIBLIOGRAPHY

[1]Arns, Robert G. "The other transistor: early history of the metal-oxide semiconductor field-effect transistor." *Engineering Science & Education Journal* 7.5 (1998): 233-240.

[2]Kaminow, Ivan P. "Optical integrated circuits: A personal perspective." *Journal of Lightwave Technology* 26.9 (2008): 994-1004.

[3]Nagarajan, Radhakrishnan, et al. "Large-scale photonic integrated circuits." *IEEE Journal of Selected Topics in Quantum Electronics*11.1 (2005): 50-65.

[4]Miller, Stewart E. "Integrated optics: An introduction." *Bell Labs Technical Journal* 48.7 (1969): 2059-2069.

[5]Koch, Thomas L., and Uziel Koren. "Semiconductor photonic integrated circuits." *IEEE Journal of Quantum Electronics* 27.3 (1991): 641-653.

[6]Ozgur, Gokhan. "Application of the resonant-layer effect to integrated isolators and other photonic components." (2006).

[7]Mizumoto, T., Shoji, Y., & Takei, R. (2012). Direct wafer bonding and its application to waveguide optical isolators. *Materials*, *5*(5), 985-1004.

[8]Petermann, K. External optical feedback phenomena in semiconductor lasers. *IEEE J. Sel. Top. Quantum Electron.* 1995, *1*, 480–489.

[9]Wolfe, R., Hegarty, J., Dillon, J. F., Luther, L. C., Celler, G. K., Trimble, L. E., Dorsey, C. S. (1985). Thin-film waveguide magneto-optic isolator. *Applied Physics Letters*, *46*, 817-819.

[10]Mizumoto, T., Kawaoka, Y., Naito, Y. (1986). Waveguide-type optical isolator using the Faraday and Cotton-Mouton effects. *Trans. IECE Japan*, E69, 968-972.

[11]Takenaka, M., & Nakano, Y. (1999). Proposal of a novel semiconductor optical waveguide isolator, *1999. IPRM. 1999 Eleventh International Conference on Indium Phosphide and Related Materials* (pp. 289-292). IEEE.

[12]Zaets, W., & Ando, K. (1999). Optical waveguide isolator based on nonreciprocal loss/gain of amplifier covered by ferromagnetic layer. *IEEE Photonics Technology Letters*, *11*(8), 1012-1014.

[13]Vanwolleghem, M., Van Parys, W., Van Thourhout, D., Baets, R., Gauthier-Lafaye, O., Lelarge F., Thedrez B., Wirix-Speetjens, R., De Boeck, J. (2004). First experimental demonstration of a monolithically integrated InP-based waveguide isolator, in OFC 2004, TuE6.

[14]Vanwolleghem, Mathias, et al. "Experimental demonstration of nonreciprocal amplified spontaneous emission in a CoFe clad semiconductor optical amplifier for use as an integrated optical isolator." *Applied physics letters* 85.18 (2004): 3980-3982.

[15]Shimizu, H., & Nakano, Y. (2004). First demonstration of TE mode nonreciprocal propagation in an InGaAsP/InP active waveguide for an integratable optical isolator. *Japanese Journal of Applied Physics*, *43*(12A), L1561.

[16]Amemiya, T., Shimizu, H., Nakano, Y., Hai, P. N., Yokoyama, M., & Tanaka, M. (2006). Semiconductor waveguide optical isolator based on nonreciprocal loss induced by ferromagnetic MnAs. *Applied Physics Letters*, *89*(2), 1104.

[17]Stadler, B.J. and Mizumoto, T., 2014. Integrated magneto-optical materials and isolators: a review. *IEEE Photonics Journal*, *6*(1), pp.1-15.

[18]Hammer, J. M., Ozgur, G., Evans, G. A., & Butler, J. K. (2006). Integratable 40 dB optical waveguide isolators using a resonant-layer effect with mode coupling. *Journal of applied physics*, *100*(10), 103103.

[19]Mizumoto, T., Mashimo, S., Ida, T., & Naito, H. (1993). In-plane magnetized rare earth iron garnet for a waveguide optical isolator employing nonreciprocal phase shift. *IEEE Transactions on Magnetics*, *29*(6), 3417-3419.

[20]Yokoi, H., Mizumoto, T., Takano, T., & Shinjo, N. (1999). Demonstration of an optical isolator by use of a nonreciprocal phase shift. *Applied Optics*, *38*(36), 7409-7413.

[21]Yokoi, H., Mizumoto, T., Shinjo, N., Futakuchi, N., & Nakano, Y. (2000). Demonstration of an optical isolator with a semiconductor guiding layer that was obtained by use of a nonreciprocal phase shift. *Applied Optics*, *39*(33), 6158-6164.

[22]Shoji, Y., & Mizumoto, T. (2006). Wideband design of nonreciprocal phase shift magneto-optical isolators using phase adjustment in Mach-Zehnder interferometers. *Applied Optics*, *45*(27), 7144-7150.

[23]Shoji, Y., Mizumoto, T., Yokoi, H., Hsieh, I. W., & Osgood Jr., R. M. (2008). Magneto-optical isolator with silicon waveguides fabricated by direct bonding. *Applied Physics Letters*, *92*(7), 071117.

[24]Ghosh, S., Keyvavinia, S., Van Roy, W., Mizumoto, T., Roelkens, G., & Baets, R. (2012). Ce: YIG/Silicon-on-Insulator waveguide optical isolator realized by adhesive bonding. *Optics Express*, *20*(2), 1839-1848.

[25]Bi, L., Hu, J., Jiang, P., Kim, D.H., Dionne, G.F., Kimerling, L.C. and Ross, C.A., 2011. On-chip optical isolation in monolithically integrated non-reciprocal optical resonators. *Nature Photonics*, *5*(12), p.758.

[26]Hammer, Jacob M., et al. "Isolators, polarizers, and other optical waveguide devices using a resonant-layer effect." *Journal of lightwave technology* 22.7 (2004): 1754.

[27]Hammer, Jacob M., et al. "Integratable 40dB optical waveguide isolators using a resonant-layer effect with mode coupling." *Journal of applied physics*100.10 (2006): 103103.

[28]Takenaka, Mitsuru, and Yoshiaki Nakano. "Proposal of a novel semiconductor optical waveguide isolator." *Indium Phosphide and Related Materials, 1999. IPRM. 1999 Eleventh International Conference on*. IEEE, 1999. (Born & Wolf, 1980)

[29]Yokoi, Hideki, et al. "Demonstration of an optical isolator with a semiconductor guiding layer that was obtained by use of a nonreciprocal phase shift." *Applied optics* 39.33 (2000): 6158-6164.

[30]Zaets, Wadim, and Koji Ando. "Optical waveguide isolator based on nonreciprocal loss/gain of amplifier covered by ferromagnetic layer." *IEEE Photonics Technology Letters* 11.8 (1999): 1012-1014.

[31]Ehrenreich, H., and H. R. Philipp. "Optical properties of Ag and Cu."*Physical Review* 128.4 (1962): 1622.

[32]Adachi, Sadao. "Model dielectric constants of GaP, GaAs, GaSb, InP, InAs, and InSb." *Physical review B* 35.14 (1987): 7454.

[33]J. W. Garland, H. Abad, M.Viccaro, and P.M. Raccah, Appl. Phys. Lett. 52, 1176-1178 (1988).

[34]Oppeneer, P. M., et al. "Ab initio calculated magneto-optical Kerr effect of ferromagnetic metals: Fe and Ni." *Physical Review B* 45.19 (1992): 10924.

[35]Brendel, R., and D. Bormann. "An infrared dielectric function model for amorphous solids." *Journal of applied physics* 71.1 (1992): 1-6.

[36]C. C. Kim, J. W. Garland, H. Abad, and P. M. Raccah, "Modeling the optical dielectric function of semiconductors: extension of the critical-point parabolic-band approximation," Phys. Rev. B 45, 11,749–11,767 (1992).

[37]Bennett, H. E., and J. M. Bennett. "*Validity of the Drude theory for silver, gold and aluminum in the infrared"* in "Optical Properties and Electronic Structure of Metals and Alloys", F. Abelès, ed. (North-Holland, Amsterdam, 1966), pp. 175–188.

[38]Ordal, M. A., et al. "Optical properties of the metals Al, Co, Cu, Au, Fe, Pb, Ni, Pd, Pt, Ag, Ti, and W in the infrared and far infrared." *Applied Optics* 22.7 (1983): 1099-1119.

[39]M. A. Ordal, R. J. Bell, J. R. W. Alexander, L. L. Long, and M. R. Querry, "Optical properties of fourteen metals in the infrared and far infrared: Al, Co, Cu, Au, Fe, Pb, Mo, Ni, Pd, Pt, Ag, Ti, V, and W," *Appl. Opt.*, vol. 24, pp. 4493–4499, Dec. 1985.

[40]Powell, C. J. "Analysis of Optical-and Inelastic-Electron-Scattering Data. II. Application to Al*†." *JOSA* 60.1 (1970): 78-93.

[41]Rakić, Aleksandar D. "Algorithm for the determination of intrinsic optical constants of metal films: application to aluminum." *Applied optics* 34.22 (1995): 4755-4767.

[42]Rakić, Aleksandar D., et al. "Optical properties of metallic films for vertical-cavity optoelectronic devices." *Applied optics* 37.22 (1998): 5271-5283.

[43]Djurišić, Aleksandra B., and E. Herbert Li. "Modeling the index of refraction of insulating solids with a modified Lorentz oscillator model." *Applied optics*37.22 (1998): 5291-5297.

[44]J. H. Weaver, C. Drafka, D. W. Lynch, and E. E. Koch, "Optical properties of metals," *Appl. Optics*, vol. 20, pp. 1124–1124, 1981.

[45]J. H. Weaver, C. Drafka, D. W. Lynch, and E. E. Koch, *Optical Properties of Metals I: Transition Metals,* $0.1 \leq h\nu \leq 500\ eV$ (ZAED, 1981).

[46]Ashcroft, N. W., and Mermin, N. D. *Solid state physics*, Philadelphia: Saunders College Publishing, 1976, Chapter 1.

[47]J. Babiskin and J. R. Anderson, Eds., American Institute of Physics Handbook (McGraw-Hill, New York, 1972), pp. 9-39, 9-40.

[48]Fox, Mark. *Optical properties of solids*. Vol. 3. Oxford university press, 2010.

[49]Almog, I. F., Bradley, M. S., & Bulovic, V. (2011). *The Lorentz Oscillator and its Applications*. Massachusetts Institute of Technology.

[50]www.engineeringtoolbox.com/metal-alloys-densities-d_50.html

[51]Bittencourt, J. A., Fundamentals of Plasma Physics, New York: Springer Science-Business Media, 2004.

[52]Pantell, Richard H., and Puthoff, Harold E. *Fundamentals of quantum electronics*, New York: Wiley, 1969.

[53]Odom, B., D. Hanneke, B. D'Urso, and G. Gabrielse. "New measurement of the electron magnetic moment using a one-electron quantum cyclotron" *Physical review letters* 97, no. 3 (2006): 30801.

[54]http://physics.nist.gov/cgi-bin/cuu/Value?gammae

[55]Butler, J. K., Martinez, M. A., Kilci R., and Evans G. A., "Optical properties of Iron to 30 eV", *To be submitted*.

[56]U. Platt and J. Stutz, *Differential Optical Absorption Spectroscopy: Principles & Applications*, (Springer-Verlag, Berlin Heidelberg, 2008).

[57]Kim, C. C., Garland, J. W., & Raccah, P. M. (1993). Modeling the optical dielectric function of the alloy system Al x Ga 1− x As. *Physical Review B*, *47*(4), 1876.

[58]J. W. Garland, H. Abad, M.Viccaro, and P.M. Raccah, Appl. Phys. Lett. 52, 1176-1178 (1988).

[59]S. F. Edwards and Y. B. Gulyaev, Proc. Phys. Soc. London 83, 496 (1964) in C. C. Kim, J. W. Garland, H. Abad, and P. M. Raccah, "Modeling the optical dielectric function of semiconductors: extension of the critical-point parabolic-band approximation," Phys. Rev. B **45,** 11,749–11,767 (1992).

[60]T. Lukes and K. T. S. Somaratna, J. Phys. C 3, 2044 (1970) in C. C. Kim, J. W. Garland, H. Abad, and P. M. Raccah, "Modeling the optical dielectric function of semiconductors: extension of the critical-point parabolic-band approximation," Phys. Rev. B 45, 11,749–11,767 (1992).

[61]NAG Mark 23 Library, "Optimization Section", http://www.nag.com/numeric/cl/nagdoc_cl23/html/E04/e04conts.html

[62]Lynch, D. W., Hunter, W. R., & Palik, E. D. (1985). *Handbook of optical constants of solids.* Vol.1 (Academic Press, Orlando, FL, 1985).

[63]Bardosova, Maria, and Tomas Wagner, eds. *Nanomaterials and Nanoarchitectures: A Complex Review of Current Hot Topics and Their Applications*. Pg. 282, Springer, 2015.

[64]Shalaev, Vladimir M., ed. *Optical properties of nanostructured random media*. Vol. 82, Pg. 194, Springer Science & Business Media, 2003.

[65]Mukundan, R., Bhansali, S., Carter, M. T., & Hunter, G. (2008). Sensor, Actuators, and Microsystems (General). ECS Transactions, 11, (14), 41-55.

[66]Weaver, J. H., Colavita, E., Lynch, D. W., & Rosei, R. (1979). Low-energy interband absorption in bcc Fe and hcp Co. *Physical Review B*, *19*(8), 3850.

[67]Abramowitz, M., & Stegun, I. A. eds. (1972). *Handbook of Mathematical Functions with Formulas, Graphs, and Mathematical Tables*, Dover, New York.

[68]Faraday, Michael. "Experimental researches in electricity. Nineteenth series." *Philosophical Transactions of the Royal Society of London* 136 (1846): 1-20.

[69]Oppeneer, P. M. "Handbook of Magnetic Materials." *Vol. 13, Elsevier, Amsterdam* (2001).

[70]Freiser, Ml. "A survey of magnetooptic effects." *IEEE Transactions on magnetics* 4.2 (1968): 152-161.

[71]Zvezdin, Anatoliĭ Konstantinovich, and Viacheslav Alekseevich Kotov. *Modern magnetooptics and magnetooptical materials*. CRC Press, 1997.

[72]Landau, Lev Davidovich, and E. M. Lifshitz. *Course of Theoretical Physics. Vol. 8: Electrodynamics of Continuous Media*. Oxford, 1960.

[73]Ishimaru, Akira. *Electromagnetic Wave Propagation, Radiation, and Scattering: From Fundamentals to Applications*. Prentice Hall, 1991.

[74]Hunt, Robert P. "Magneto-Optic Scattering from Thin Solid Films." *Journal of Applied Physics* 38.4 (1967): 1652-1671.

[75]Yang, Z. J., and M. R. Scheinfein. "Combined three-axis surface magneto-optical Kerr effects in the study of surface and ultrathin-film magnetism." *Journal of applied physics* 74.11 (1993): 6810-6823.

[76]You, Chun-Yeol, and Sung-Chul Shin. "Derivation of simplified analytic formulae for magneto-optical Kerr effects." *Applied physics letters* 69.9 (1996): 1315-1317.

[77]Robinson, C. C. (1960). *The longitudinal Kerr magneto-optic effect in ferromagnetic thin films* (Doctoral dissertation, Massachusetts Institute of Technology).

[78]Purcell, S. T., et al. "Spatially resolved magneto-optical investigation of the perpendicular anisotropy in a wedge-shaped ultrathin epitaxial Co layer on Pd (111)." *Journal of magnetism and magnetic materials* 113.1-3 (1992): 257-263.

[79]Weller, D., et al. "Orbital magnetic moments of Co in multilayers with perpendicular magnetic anisotropy." *Physical Review B* 49.18 (1994): 12888.

[80]You, Chun-Yeol, and Sung-Chul Shin. "Generalized analytic formulae for magneto-optical Kerr effects." *Journal of applied physics* 84.1 (1998): 541-546.

[81]Nederpel, P. Q. J., and J. W. D. Martens. "Magneto-optical ellipsometer." *Review of scientific instruments* 56.5 (1985): 687-690.

[82]Tanaka, Shun-ichi. "Longitudinal Kerr magneto-optic effect in Permalloy film." *Japanese Journal of Applied Physics* 2.9 (1963): 548.

[83]Ferguson, P. E., and R. J. Romagnoli. "Transverse Kerr Magneto-Optic Effect and Optical Properties of Transition-Rare-Earth Alloys." *Journal of Applied Physics* 40.3 (1969): 1236-1238.

[84]Shimizu, H., Goto, S., & Mori, T. (2010). Optical Isolation Using Nonreciprocal Polarization Rotation in Fe–InGaAlAs/InP Semiconductor Active Waveguide Optical Isolators. *Applied Physics Express*, *3*(7), 072201.

[85]De Lacheisserie, Etienne du Tremolet, Damien Gignoux, and Michel Schlenker, eds. *Magnetism: II-Materials and Applications*. Springer Science & Business Media, 2012.

[86]Krinchik, G. S., & Artem'ev, V. A. (1968). Magneto-optical properties of Ni, Co, and Fe in the ultraviolet, visible, and infrared parts of the spectrum. *Sov. Phys. JETP*, *26*(6), 1080-1085.

[87]Krinchik, G. S., & Artemjev, V. A. (1968). Magneto-optic Properties of Nickel, Iron, and Cobalt. *Journal of Applied Physics*, *39*(2), 1276-1278.

[88]Landau, Lev Davidovich, and E. M. Lifshitz. *Course of Theoretical Physics. Vol. 8: Electrodynamics of Continuous Media*. Oxford, 1960.

[89]Kartalopoulos, Stamatios V. *Free space optical networks for ultra-broad band services*., Pg. 23, John Wiley & Sons, 2011.

[90]Haynes, W. M. (Ed.). (2014). *CRC handbook of chemistry and physics*. 95th edition. CRC press.

[91]V. A. Barker, L. S. Blackford, J. Dongarra, J. D. Croz, S. Hammarling, M. Marinova, J. Waoeniewski, and P. Yalamov, *LAPACK95 Users' Guide*. SIAM, 2001.

[92]Shimizu, H., Yoshida, S., & Goto, S. (2008). Semiconductor waveguide optical isolators towards larger optical isolation utilizing nonreciprocal phase shift by ferromagnetic Co. *IEEE Photonics Technology Letters*, *20*(18), 1554-1556.

[93]Shimizu, H., Goto, S., & Mori, T. (2010). Optical Isolation Using Nonreciprocal Polarization Rotation in Fe–InGaAlAs/InP Semiconductor Active Waveguide Optical Isolators. *Applied Physics Express*, *3*(7), 072201.

[94]Zaman, T. R., Guo, X., & Ram, R. J. (2008). Semiconductor waveguide isolators. *Journal of Lightwave Technology*, *26*(2), 291-301.

[95]Bi, L., Hu, J., Jiang, P., Kim, D. H., Dionne, G. F., Kimerling, L. C., & Ross, C. A. (2011). On-chip optical isolation in monolithically integrated non-reciprocal optical resonators. *Nature Photonics*, *5*(12), 758-762.

[96]Sun, X.Y., Du, Q., Goto, T., Onbasli, M.C., Kim, D.H., Aimon, N.M., Hu, J. and Ross, C.A., 2015. Single-step deposition of cerium-substituted yttrium iron garnet for monolithic on-chip optical isolation. *Acs Photonics*, *2*(7), pp. 856-863.

[97]Lira, H., Yu, Z., Fan, S. and Lipson, M., 2012. Electrically driven nonreciprocity induced by interband photonic transition on a silicon chip. *Physical review letters*, *109*(3), p.033901.

[98]Yang, Y., Galland, C., Liu, Y., Tan, K., Ding, R., Li, Q., Bergman, K., Baehr-Jones, T. and Hochberg, M., 2014. Experimental demonstration of broadband Lorentz non-reciprocity in an integrable photonic architecture based on Mach-Zehnder modulators. *Optics express*, *22*(14), pp.17409-17422.

[99]Mizumoto, T., Kawaoka, Y., Naito, Y. (1986). Waveguide-type optical isolator using the Faraday and Cotton-Mouton effects. *Trans. IECE Japan*, E69, 968-972.

[100]Mizumoto, T., Ryohei, T, and Shoji, Y. (2012). "Waveguide optical isolators for integrated optics." *IEEE Journal of Quantum Electronics* 48.2: 252-260.

[101]P. B. Johnson and R. W. Christy, "Optical constants of transition metals: Ti, V, Cr, Mn, Fe, Co, Ni, and Pd," *Phys. Rev. B*, vol. 9, pp. 5056–5070, 1974.

[102]Hammer, J. M., Ozgur, G., Evans, G. A., & Butler, J. K. (2006). Integratable 40dB optical waveguide isolators using a resonant-layer effect with mode coupling. *Journal of applied physics*, *100*(10), 103103.

[103]Okamura, Y., Inuzuka, H., Kikuchi, T., Yamamoto, S. (1986). "Nonreciprocal propagation in magnetooptic YIG rib waveguides." *Journal of lightwave technology*, 4(7):711-4.

[104]Hansen, P.; Krume, J.P. Magnetic and magneto-optical properties of garnet films. *Thin Solid Films* 1984, *114*, 69–107.

[105]Gomi, M., Satoh, K., & Abe, M. (1988). Giant Faraday rotation of Ce-substituted YIG films epitaxially grown by RF sputtering. *Japanese journal of applied physics*, *27*(8A), L1536.

[106]Shintaku, T., Tate, A., & Mino, S. (1997). Ce-substituted yttrium iron garnet films prepared on Gd3Sc2Ga3O12 garnet substrates by sputter epitaxy. *Applied physics letters*, *71*, 1640-1642.

[107]Mizumoto, T.; Saito, H. Semi-leaky waveguide optical isolator. In *Proceedings of Optical Fiber Communication Conference*, Anaheim, CA, USA, 25 March 2007.

[108]Mizumoto, T. Wafer bonding of magneto-optic garnet and its application to integrated optical devices. In *Proceedings of the 210th Meeting of Electrochemical Society*, Cancun, Mexico, 29 October–3 November 2006; p.1258.

[109]Takei, R.; Abe, K.; Mizumoto, T. Room-temperature direct bonding for integrated optical devices. In *Proceedings of IEEE Nano-Optoelectronics Workshop*, Shonan Village, Japan, 2–15 August 2008; pp. 203–204.

[110]Goto, T., Onbasli, M. C., Kim, D. H., Singh, V., Inoue, M., Kimerling, L. C., & Ross, C. A. (2014). Nonreciprocal racetrack resonator based on vacuum-annealed magnetooptical cerium-substituted yttrium iron garnet. *Optics express*, *22*(16), 19047-19054

[111]Goto, T., Eto, Y., Kobayashi, K., Haga, Y., Inoue, M., & Ross, C. A. (2013). Vacuum annealed cerium-substituted yttrium iron garnet films on non-garnet substrates for integrated optical circuits. *Journal of Applied Physics*, *113*(17), 17A939.

[112]Callen, Herbert B. "The application of Onsager's reciprocal relations to thermoelectric, thermomagnetic, and galvanomagnetic effects." *Physical Review* 73.11 (1948): 1349.

[113]Yariv, A., & Yeh, P. (2006). *Photonics: optical electronics in modern communications (the oxford series in electrical and computer engineering)*. Oxford University Press, Inc.

[114]Sung, Sang-Yeob. PhD dissertation: *Integrating magneto-optical garnet isolators on semiconductor substrates*. ProQuest, 2008.